

RICE UNIVERSITY

**Experimental Studies of the Fractional Quantum
Hall Effect and the Wigner Solids**

by

Chi Zhang

A THESIS SUBMITTED
IN PARTIAL FULFILLMENT OF THE
REQUIREMENTS FOR THE DEGREE

Doctor of Philosophy

APPROVED, THESIS COMMITTEE:

Rui-Rui Du, Chair
Professor, Physics

Adilet Imambekov
Assistant Professor, Physics

Junichiro Kono
Professor, Electrical and Computer
Engineering

Houston, Texas

April, 2010

ABSTRACT

Experimental Studies of the Fractional Quantum Hall Effect and the Wigner Solids

by

Chi Zhang

This Ph.D. thesis is composed of two parts: the first part is concerned with electron transport in the higher Landau levels (LL) in a two-dimensional electron system (2DES); the second part is focused on the Wigner Crystal in two-dimensional hole system (2DHS).

We report on the high Landau-level (LL) magnetotransport (including tilt-fields) in a high purity modulation-doped GaAs/AlGaAs quantum Well (QW) with twice the electron density of standard samples. A quantized $\nu = 5/2$ Hall plateau is observed at $B \sim 10$ T, with an activation gap $\Delta_{5/2} \sim 125$ mK; the plateau can persist up to a $\sim 25^\circ$ tilt-field. This finding is discussed in the context of proposed Moore-Read Pfaffian (Pf) wave function (or Anti-Pfaffian (APf)) being possible ground states at $5/2$. The tilted-fields induce background resistance at $5/2$ that could be either isotropic or anisotropic, depending simply on in-plane magnetic field orientation with respect to the GaAs crystalline axis. Such data indicate a substantial coupling between the $5/2$ collective phases and the GaAs crystal.

In a high hole density ($p = 2.0 \times 10^{11} \text{ cm}^{-2}$), high mobility ($\mu = 1 \times 10^6 \text{ cm}^2/\text{Vs}$) 20 nm wide GaAs/AlGaAs quantum well, we observed reentrant insulating phases around Landau-level filling factor $\nu = 1/5$ and $\nu = 2/9$ at very high magnetic fields. Previous experiments reported the reentrant insulating phases around the $\nu = 1/3$

FQHE state in dilute 2DHS and around the $\nu = 1/5$ FQH liquid in 2DES, respectively. It is rather interesting that our experimental results in the hole system look like the former electron results at low fields. Our T -dependent conductance measurements exhibit rather intriguing behaviors: the Arrhenius plot of the conductance (vs. $1/T$) suggests a certain energy scale in the melting procedure of the solid phase. We also observed a large threshold for electric field in the differential conductance measurements, which is an indication of the sliding motion of Wigner solid driven by an external field. These phenomena are related to the depinning of Wigner solids under various magnetic fields. A possible explanation is that the effective pinning potential increases with the magnetic fields.

Acknowledgments

First, I would like to thank my thesis advisor Professor Rui-Rui Du for bringing me into the field of quantum Hall physics, and for his insight and invaluable guidance throughout these projects.

I would also like to thank the committee members Professor Junichiro Kono and Professor Adilet Imambekov for their reading of the thesis and comments.

Highest-purity two-dimensional electron GaAs/AlGaAs quantum wells (QW) were grown by molecular beam epitaxy by the group of Dr. Loren Pfeiffer and Ken West at Alcatel-Lucent, Bell Laboratories (now at Princeton University). The high mobility C-doped GaAs/AlGaAs QW wafers were provided by Dr. Michael Manfra of Bell laboratories (now at Purdue University), Dr. Loren Pfeiffer and Ken West.

I would like to thank the members in my lab who contributed to this work: Dr Tauno Knuuttila for providing the ultralow temperature magnetotransport data for the sample; Yanhua Dai for the GaAs substrate etching experiment which is crucial for identifying the crystalline axis. I am indebted to Dr. Changli Yang, who taught me the ropes of low temperature transport experiments and who provided constant advice and encouragement. Thanks are due to Dr. Guangtong Liu not only for being my roommate and good colleague, but also for offering me lots of help and useful advice on work and daily life. I appreciate Dr. Z. Q. Yuan for sharing his techniques and experiences on clean-room processing, and K. Stone for advice in laboratory research and presentations. I also had some good discussions on research topics with Ivan Knez and Xiaowei He. Special thanks are due to Patrick Johnson, who helped train me as a user for the Rice cleanroom. Special thanks for my friend Yu Pu, who taught me various plotting skills; for Liang Zhao, who is not only good at computer

techniques, but also discuss his physics ideas with me; for Changhao Wang, who is very helpful with computer programming.

I acknowledge the financial support from Department of Energy (DOE) and W. M. Keck Foundation, which made this thesis work possible. A portion of this work was performed at the National High Magnetic Field Laboratory, which is supported by NSF Cooperative Agreement No. DMR-0084173, by the State of Florida, and by the DOE. Expert technical assistance of T. Murphy, J. H. Park, and J. Glover is greatly appreciated.

Contents

Abstract	ii
Acknowledgments	iv
List of Illustrations	ix
List of Tables	xvi
1 Introduction	1
1.1 Introduction to the Section of 5/2 State	1
1.2 Introduction to the Section of Wigner Solid	6
2 Background of 5/2 State in GaAs	9
2.1 2DEG in GaAs/AlGaAs Quantum Well	9
2.2 Integer Quantum Hall Effect	11
2.3 Fractional Quantum Hall Effect	12
2.4 Activation Energy in Higher LLs under a Perpendicular Magnetic Field	14
2.5 Activation Energy in Higher LLs under a Tilted Magnetic Field . . .	15
2.6 Anisotropic Electronic Transport in Higher Landau Levels	17
2.7 Transport in Higher Landau Levels under a Tilted Magnetic Field . .	18
3 Experiment of 5/2 State	20
3.1 Experimental Setup	20
3.2 Sample Characterization	22
3.3 Experimental Results in a Perpendicular Magnetic Field	25
3.4 Experimental Results in a Tilted Magnetic Field	31

3.5	Anisotropic and Isotropic Magnetoresistances under Perpendicular and Tilted Magnetic Fields	41
3.6	Discussion	51
4	Conclusions of 5/2 State Experiments	53
5	Background of Wigner Crystal	55
5.1	Wigner Crystal	55
5.2	Magnetotransport Measurements on Wigner Solids	56
5.3	Fractional Quantum Hall Liquid and Wigner Solid	60
5.4	Two-Dimensional Hole System in GaAs	61
6	Experiments on Wigner Crystal in a Two-Dimensional Hole System	64
6.1	Experimental Setup	64
6.2	Sample Characterization	66
6.3	Conductance and Resistance Measurements	74
6.4	Non-linear Conductivity Measurements	89
7	Conclusions of Wigner Crystal in 2DHS	95
A	Sample Information	97
A.1	2D Electron Samples	97
A.2	2D Hole Samples	97
A.3	Effect of Light on Samples	98
B	Determination of crystalgraphic axis by defect-pit etching technique	99
B.1	Etching Profile of Cross-Section	99

B.2 Pit-Etching by Using KOH for GaAs Sample	100
--	-----

B.3 Pit-Etching by Using $\text{H}_3\text{PO}_4:\text{H}_2\text{O}_2:\text{H}_2\text{O}$ (1:1:38) for GaAs Sample . .	103
---	-----

Bibliography	104
---------------------	------------

Illustrations

1.1	An overview of magnetotransport data showing the IQHE and the FQHE (Willett et al [10], 1987).	4
2.1	Band diagram of the sample with a 20 nm wide GaAs/AlGaAs quantum well, with the wavefunction below the Fermi level.	10
3.1	In-plane magnetic field experimental setup, in which the sample surface can be tilted. Zeeman energy is proportional to total B , and Landau level spacing is proportional to $B \cos \theta$	21
3.2	Schematic of the Van der Pauw configuration	22
3.3	Schematic of the structure of the sample with modulation Si-doped 20 nm wide GaAs/Al _{0.24} Ga _{0.76} As quantum well (QW-A).	23
3.4	The magnetoresistance in the same 20 nm QW (sample e-QW-A-1) measured at 10 mK is presented, showing the quantized Hall plateaus at 5/2 and 7/2, as well as at 7/3 and 8/3 (Courtesy of Dr. Tauno Knuuttila [56]).	25
3.5	Resistance R_{xx} and R_{yy} of 20 nm wide QW(sample e-QW-A-3)under perpendicular magnetic field	28
3.6	R_{yy} of 20 nm wide QW (sample e-QW-A-2) as a function of temperature (between 20mK and 300 mK) for perpendicular magnetic fields.	29

3.7 Under perpendicular magnetic fields, the temperature-dependent resistance of 8/3, 5/2, and 7/3 states, exhibit the logarithm behaviors: $\ln(R_{xx}) \propto \exp(-2\Delta/k_B T)$, we obtained the activation energies Δ for 5/2, 7/3, and 8/3 states are 125 mK, 200 mK, and 65 mK, respectively. 30

3.8 Longitudinal resistance R_{yy} as a function of temperature (between 20 mK and 300 mK) for a tilted angle ($\theta \sim 4.4^\circ$). 32

3.9 Longitudinal resistance R_{yy} as a function of temperature (between 20 mK and 300 mK) for a tilted angle ($\theta \sim 7.3^\circ$). 33

3.10 Longitudinal resistance R_{yy} as a function of temperature (between 20 mK and 300 mK) for a tilted angle ($\theta \sim 10.2^\circ$). 34

3.11 Longitudinal resistance R_{yy} as a function of temperature (between 20 mK and 300 mK) for a tilted angle ($\theta \sim 13.2^\circ$). 35

3.12 Longitudinal resistance R_{yy} as a function of temperature (between 20 mK and 300 mK) for a tilted angle ($\theta \sim 16.2^\circ$). 36

3.13 Longitudinal resistance R_{yy} as a function of temperature (between 20 mK and 120 mK) for a tilted angle ($\theta \sim 20.1^\circ$). 37

3.14 Longitudinal resistance R_{yy} as a function of temperature (between 20 mK and 120 mK) for a tilted angle ($\theta \sim 25^\circ$). 38

3.15 Longitudinal resistance R_{yy} as a function of temperature (between 20 mK and 120 mK) for a tilted angle ($\theta \sim 30^\circ$). 39

3.16 The 3-dimensional figure of longitudinal resistances (R_{yy}) under various in-plane magnetic fields. 39

3.17 energy gaps Δ (and quasi gaps Δ^{quasi}) of 8/3, 5/2, 7/3 under various tilted-magnetic fields. 40

3.18 The Hall resistivity (of e-QW-A-3) under various tilted angles: $0^\circ, 8^\circ, 18^\circ, 25^\circ, 30^\circ$; and two red traces are derivatives $B \times dR_{xy}/dB$ for 8° and 30° , respectively. 40

- 3.19 The magnetic resistance R_{xx} (solid, red) and R_{yy} (dotted, blue) in sample 20nm QW (sample e-QW-A-2) measured in a perpendicular magnetic field, respectively along orthogonal crystalline axis $[\bar{1}\bar{1}0]$ and $[110]$, are shown. The inset depicts schematically the measurement axis. For comparison, the data for sample e-QW-B is shown for the magnetic field range cover $9/2$ and $11/2$ 43
- 3.20 R_{xx} (solid line) and R_{yy} (dashed line) (of Sample e-QW-A-3) under various tilted angles (configuration A). The top trace is Hall resistance under tilted B , and the plateaus at filling factors of $7/3$ and $8/3$ are very clear. 45
- 3.21 R_{xx} (solid line) and R_{yy} (dashed line) (of sample e-QW-A-3) under various tilted angles (configuration B). The top inset is Hall resistance under tilted B , and the plateaus at filling factors of $7/3$ and $8/3$ are very distinct. 46
- 3.22 The resistances of states with a fractional filling factor of $5/2$ (of sample e-QW-A-3) under various in-plane magnetic field. R of configuration A (circled trace) exhibits large anisotropy, the anisotropy ratio is around 10; on the other hand, R of configuration B (rectangled trace) exhibits isotropic behavior. In the plot, the symbols are presented as: R_{xx} in configuration A (red-circled curve), R_{yy} in configuration A (blue-circled curve); R_{xx} in configuration B (red-squared curve), R_{yy} in configuration B (blue-squared curve). . . 47

- 3.23 Longitudinal resistances of $7/2$ (of sample e-QW-A-3) under various in-plane magnetic field. R of configuration A (circled trace) exhibits large anisotropy, the anisotropy ratio is larger than 10; on the other hand, R of configuration B (rectangled trace) exhibits isotropic behavior. In the plot, the symbols are presented as: R_{xx} in configuration A (red-circled curve), R_{yy} in configuration A (blue-circled curve); R_{xx} in configuration B (red-squared curve), R_{yy} in configuration B (blue-squared curve). 48
- 3.24 The magnetoresistance R_{xx} (solid symbols) and R_{yy} (open symbols) (of sample e-QW-A-2) are shown for sample c at filling factor $9/2$, as a function of the in-plane magnetic field $B_{//}$; the circle represent the data for $B_{//}$ applied along the $[1\bar{1}0]$ axis; the square represent the data for $B_{//}$ applied along the $[110]$ axis. 49
- 3.25 The magnetoresistance R_{xx} (solid symbols) and R_{yy} (open symbols) (of sample e-QW-A-2) are shown for sample c at filling factor $11/2$, as a function of the in-plane magnetic field $B_{//}$; the circle represent the data for $B_{//}$ applied along the $[1\bar{1}0]$ axis; the square represent the data for $B_{//}$ applied along the $[110]$ axis. 50
- 5.1 The magnetotransport data of a low electron density sample, there exists a reentrant insulating phase around $\nu = 1/5$ FQHE state (Sajoto et al [43]). 58
- 5.2 The magnetotransport data of a dilute 2DHS, with a reentrant insulating phase along $\nu = 1/3$ FHQE state (Santos et al [42]). 59
- 5.3 The band structure diagram in bulk GaAs, (panel a)), and in GaAs quantum well (panel b)). 62

6.1	Schematic for setup of conductance (panel a)) and nonlinear (ac + dc) conductance (panel b)) measurements on Corbino samples.	67
6.2	The schematic of the main structure of the 20 nm wide GaAs/AlGaAs wafers: A and B, other details of layers are not present in this figure.	69
6.3	Optical picture of typical Corbino samples, the sample B3 (h-QW-B-3) (left) has In/Zn contacts and the sample A2 (h-QW-A-2) (right) has Au/Be contacts.	69
6.4	Conductance data of 20nm QW B3 (Corbino sample h-QW-B-3) in the magnetic field from 0 to 40 T.	71
6.5	Magnetoresistance R_{xx} (red and green) and R_{xy} of 20 nm wide QW B2 (Van der Pauw sample h-QW-B-2) at a base $T \sim 20$ mK.	72
6.6	Conductance data of 20nm QW A2 (Corbino sample h-QW-A-2) in the magnetic field from 19 to 45 T.	73
6.7	Conductance of sample A2 under ac electric fields, which ranges from 4.6 mV/cm to 92 mV/cm.	76
6.8	Conductance of sample A2 under ac electric fields, which ranges from 92 mV/cm to 276 mV/cm.	77
6.9	Conductance of sample A2 under ac electric fields, which ranges from 276 mV/cm to 437 mV/cm.	78
6.10	Conductance of sample A2 under ac electric fields, which ranges from 437 mV/cm to 690 mV/cm.	79
6.11	Conductance sample B3 (h-QW-B-3) under ac electric fields, which ranges from 1.8 mV/cm to 226 mV/cm.	80
6.12	T -dependent conductance of Corbino sample A2 (h-QW-A-2) . The applied field $E_{ac} = 46$ mV/cm.	81
6.13	T -dependent conductance of sample A2 (h-QW-A-2) (for $T = 41 - 107$ mK) is measured in a magnetic range: $B \sim 34 - 42$ T.	82

6.14	T -dependent conductance of sample A2 (h-QW-A-2) (for $T = 115 - 191$ mK) is measured in a magnetic range: $B \sim 34 - 42$ T.	83
6.15	T -dependent conductance of sample A2 (h-QW-A-2) (for $T = 204 - 316$ mK) is measured in a magnetic range: $B \sim 34 - 42$ T.	83
6.16	T -dependent conductance data (sample h-QW-A-2) under various magnetic fields (at various magnetic fields: $B \sim 36$ T (red, solid circle), 38 T (black, solid circle), 40 T (blue, solid square)). The Arrhenius plot exhibits two energy scales: Energy gap (E_g) $G_{xx} \sim \exp(E_g/k_B T)$ and activation energy (Δ): $G_{xx} \sim \exp(-\Delta/k_B T)$	84
6.17	T -dependent conductance data (sample h-QW-A-2) under various magnetic fields (at various magnetic fields: $B \sim 35$ T (blue open triangular), 39 T (black, open square), 41 T (red, open square)). The Arrhenius plot exhibits two energy scales: Energy gap (E_g) $G_{xx} \sim \exp(E_g/k_B T)$ and activation energy (Δ): $G_{xx} \sim \exp(-\Delta/k_B T)$	85
6.18	Energy gaps E_g and Δ (of sample h-QW-A-2) under various magnetic fields: 35 T, 36 T, 38 T, 39 T, 40 T, 41 T.	86
6.19	T -dependent conductance of Corbino sample B3 (h-QW-B-3) with T : 60 mK to 270 mK.	88
6.20	The nonlinear conductivity measurements (h-QW-A-2) exhibit large threshold electric field in solid phase, the linear behavior at $B \sim 37.8, 38.1$ T indicate the liquid phase at these magnetic fields. From Lockin-amplifier, we applied ac voltage $V_{ac}=30$ mV, which corresponds to the ac-field $E_{ac} = 6.9$ mV/cm at the inner radius of the Corbino sample.	91
6.21	The threshold field under various magnetic fields simply indicate the parameters of the phases of various filling factors.	92
6.22	The slope of the j vs. E ($E > E_{th}$) in the nonlinear conductance measurements.	92

6.23	The schematic of phase diagram of the 20 nm wide GaAs/AlGaAs QW sample A2 (h-QW-A-2) with a high hole density ($p \sim 2 \times 10^{11} \text{ cm}^{-2}$). The phase diagram exhibit the phases under various temperature (T) and magnetic field (B).	93
6.24	The differential conductance of Corbino sample B (h-QW-B-3) is performed by applying ac+dc electric fields, with dc field $\sim 22.6 \text{ mV/cm} - 226 \text{ mV/cm}$	93
B.1	Cr crucible and basket are used for pit-etching with KOH.	101
B.2	SEM picture, with the scale of rectangle structure $\sim 100 - 200 \text{ nm}$	101
B.3	SEM picture with a larger scale, and the typical scale of rectangle structure $\sim 100 - 200 \text{ nm}$	102
B.4	Bowtie strcutures in the GaAs sample are obtained by pit-etching with $\text{H}_3\text{PO}_4:\text{H}_2\text{O}_2:\text{H}_2\text{O}$ (1:1:38).	103

Tables

3.1	Electron density, mobility, and activation gaps measured in the fractional quantum Hall states $5/2$ and $7/3$	26
-----	--	----

Chapter 1

Introduction

1.1 Introduction to the Section of 5/2 State

Under the extreme conditions of a strong perpendicular magnetic field and low temperatures, a two-dimensional electron system (2DES) exhibits physical properties which have been the subject of research for almost 30 years. The field has seen many discoveries that were unforeseen by theories [1]. Among the most important discoveries are the integer quantum Hall effect (IQHE) by Klaus Von Klitzing [2] in a Silicon MOSFET in 1980 and the fractional quantum Hall effect (FQHE) by D. C. Tsui, H. L. Stormer, and A. C. Gossard [3] in GaAs/AlGaAs heterostructures in 1982. In Laughlin's work [4], a splendid explanation was proposed for fractional quantized states with $1/3$ filling factors. Many new FQH states, all characterized by odd-denominator filling factors, were soon observed following improvements in sample purity. The formation of these states can be understood in the framework of composite fermions (CFs): new quasiparticles each carries one electron and an even number (*i.e.* 2, 4, 6) of magnetic flux quanta [5,6]. An overview of magnetotransport in a high mobility GaAs/AlGaAs sample can be seen in Figure 1.1.

Landau levels (quantum number N) with half-filling have a special place in quantum Hall physics. To begin with, the single particle density of states peaks at half-integer fillings, like $1/2$, $3/2$, $5/2$, $7/2$, and so on. Electron correlations at these fillings, however, dominate the physics and novel, many-particle phases emerge. For

example, magnetotransport at half-fillings at different N in this system are found to exhibit completely different characteristics in terms of low temperature magnetotransport resistances, namely, the diagonal resistivity, ρ_{xx} and the Hall resistivity, ρ_{xy} . Down to a typical temperature $T \sim 20$ mK, such characteristics in the $N = 0, 1, 2$ have by and large conformed to the following pattern: 1) In the lowest LL, $N = 0$, the ρ_{xx} at $\nu = 1/2, 3/2$ show a weak temperature dependence, and the concomitant ρ_{xy} is classical, *i.e.*, linear with magnetic field B [7]. The transport features of $1/2$ and $3/2$ are well described by the formation of a CF Fermi surface, which is compressible [6, 8, 9]. 2) In the first excited LL, $N = 1$, the ρ_{xy} at $\nu = 5/2$ (and $\nu = 7/2$) shows quantized plateaus, and ρ_{xx} minimum shows activated transport associated with an energy gap [10–12]. The $\nu = 5/2$, which is an even-denominator fractional quantum Hall effect (FQHE), and other states in $N = 1$ LL, are probably the most interesting, due to their relevance to the non-Abelian quasiparticles [13, 14]. As proposed by theories, the $5/2$ FQHE is described by the Moore-Read Pfaffian (Pf) wave function [13, 15–18], or its particle-hole symmetry conjugate, the Anti-Pfaffian (APf) [19, 20]. Either Pf or APf supports quarter-charged quasiparticles that obey non-Abelian statistics, and non-trivial braiding of these entities form the bases for fault-topological quantum computation [14, 21]. 3) In $N = 2$, magnetotransport at $\nu = 9/2, 11/2$ is strongly anisotropic [22–24], a feature that can be attributed to a striped electronic phase [26, 27] or liquid crystal-like phase [28].

As part of the introduction, it is helpful to highlight some of the major findings in high LLs. In 1987, Willet et al [10] discovered the first even-denominator FQHE state at filling factor $5/2$. While the $5/2$ shows typical signatures of a FQHE, namely, the quantization of a Hall plateau at $\rho_{xy} = (h/e^2)/(5/2)$ and a vanishing magnetoresistivity ρ_{xx} at low temperatures, the formation of FQHE at an even-denominator filling

factor presented profound challenges for theoretical understanding. It could not be understood based on a generalization of Laughlin's wavefunction, which requires the odd-denominator filling factors. The 5/2 quantum Hall liquid is protected by an energy gap, $\Delta_{5/2}$, which measures the creation energy for a pair of quasi-particles and quasi-hole from the ground state [10–13, 17, 20, 21, 23, 24, 27–32]. The activation energy of FQHE state can be determined from the thermal activated T -dependence of the resistance. Arrhenius plot ($\ln(R_{xx})$ vs. $1/T$) exhibit a linear behavior for certain FQH liquid: $R_{xx} = \text{const} \times \exp(-\Delta/2T)$, with Δ being the energy gap of the fractional quantum Hall state. Exact diagonalization in small systems and numerical calculations in various system size [15, 17, 18, 31, 33–35] have confirmed that the wave function of the experimentally observed 5/2 state has a strong overlap with the Pf. More recently, the issue of the particle-hole symmetry in the 5/2 state has been considered, and the APf are degenerate in energy for the Coulomb interaction if LL mixing could be ignored [19, 20]. The role of three body interaction [16, 34, 35] in 5/2 has been emphasized, which can be influenced by LL mixing or other material factors [18, 34–36]. Recent numerical calculations show that the ground state of the FQH Hamiltonian at 5/2 is fully spin-polarized even in the limit of zero Zeeman energy [37]. However, the predicted properties of Pf and APf have yet to be experimentally confirmed for the 5/2 FQHE observed in real systems.

Based on a finite-size calculation, Morf in 1998 reexamined [15] the problem of the ground state at 5/2, and reached the remarkable conclusion that the 5/2 ground state has a stronger overlap with a spin-polarized wavefunction, proposed by Moore and Read [13], termed a Pfaffian (Pf) wavefunction. The transition of the ground state at 5/2 under a tilted field can be viewed as resulting from an incompressible (gapped) to a compressible (gapless) state wavefunction. The 5/2 state is equivalent

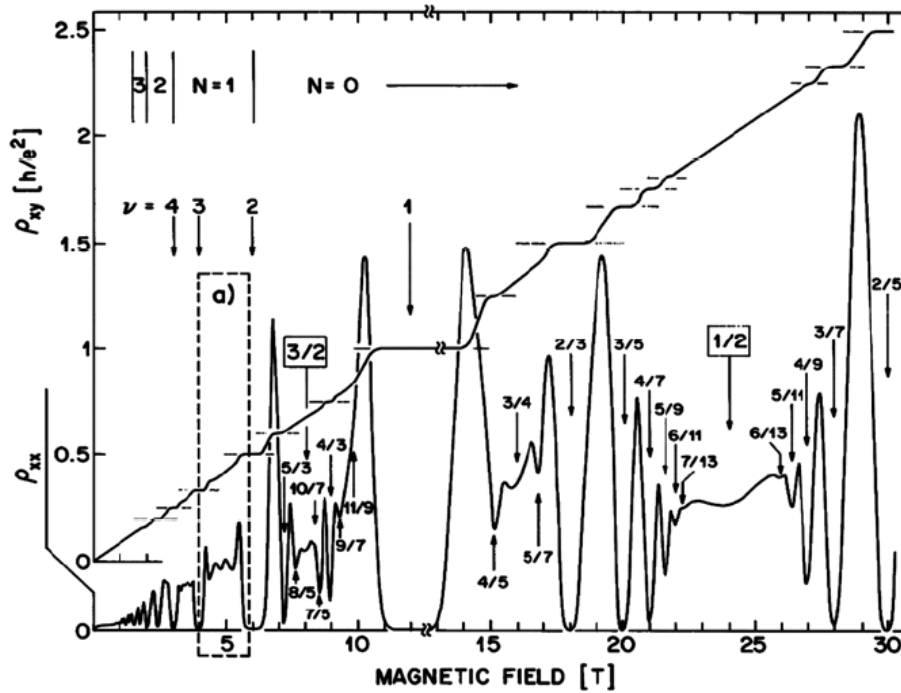


Figure 1.1 : An overview of magnetotransport data showing the IQHE and the FQHE (Willett et al [10], 1987).

to a p-wave superconductor proposed by Greiter, Wen, Wilczek [16].

The nature of the electron states in half-filling, but higher Landau levels ($N > 1$) remained unclear until 1999, when two groups, Lilly et al [23], and Du et al [24], independently reported the observation of strongly anisotropic transport at filling factors $9/2$ and $11/2$ ($N = 2$). The magnetoresistances were found to be dependent on the underlying GaAs crystalline axis. In the samples studied in [23, 24], a high resistance was always found along $[1\bar{1}0]$, and a low resistance along $[110]$; the resistance ratio can be as high as $1500 : 1$ [38]. In subsequent work, Pan et al [12] and Lilly et al [25] found that the high resistance axis can be turned by an in-plane magnetic field in the tilted field experiments. In the samples they studied, the high resistance axis is always aligned with the in-plane magnetic field direction. More remarkably,

in these very high mobility samples, the $5/2$ FQHE states not only diminish under a tilted magnetic field, they also develop into anisotropic states, much like half-filling in the $N = 2$ LL. These experiments underscored that quantum phase transitions can be tuned by experimental parameters, such as an in-plane magnetic field.

Current theories based on Hartree-Fock (HF) calculations propose that the ground states at $9/2$ and $11/2$ are striped phases [26,27], which are broken-symmetry phases having alternating filling factors 4 and 5 (for $9/2$), or 5 and 6 (for $11/2$) along the high-resistance axis. Theories taking into account the quantum fluctuations at very low temperatures propose that the ground states at these half-fillings are liquid-crystal like phases [28], which have no long range order. A notable fact is that, to date, the underlying mechanism for symmetry breaking remains unclear [38].

The physics underlying these rich phases and the phase transitions between them have been extensively studied in terms of pseudopotentials [17, 39]. Rezayi and Haldane have shown by numerical calculations (exact diagonalization) that there exists a rather narrow window for stabilizing the quantized Hall states at half-fillings [39]. In particular, the pseudopotential ratio V_1/V_3 is found in the window for the formation of a paired FQHE state at $5/2$ in GaAs/AlGaAs samples with realistic parameters. Increasing or decreasing this ratio leads to a crossover to compressible CF phases or a phase transition towards an anisotropic phase. This later scenario has been observed experimentally [12,23].

This part of the Ph.D. Thesis is concerned with an experimental study of the magnetotransport properties at $5/2$, $7/2$, $9/2$, and $11/2$ in a quantum well having a very high electron density, allowing for observation of these states at a field value twice as high as in standard samples.

This project is motivated by several factors: 1) to study the influence of LL mixing

on the $5/2$ and $9/2$ states. Increasing the magnetic field reduces mixing, thereby affecting the wavefunctions of the high LL states. In particular, recent theories proposed that an Anti-Pfaffian (APf) wavefunction could exist at $5/2$, which is degenerate in energy with the Pfaffian (Pf). The relevance of Pf or APf depends on LL mixing, a parameter that can be tuned by density; 2) to study the influence of Zeeman energy on the $5/2$ state. It is shown theoretically [13] that the Pf and APf must be at least partially spin-polarized. Observation of $5/2$ FQHE state in a high magnetic field supplies indirect evidence for ruling out a spin-unpolarized ground state; 3) to study the influence of orbital size on the anisotropic states at $9/2$ and $11/2$. Current Hartree-Fock calculations are dependent on the pseudopotentials describing electron-electron interactions, and for higher magnetic fields, the HF model may break down.

This part of the thesis is organized as follows: a brief summary for background is given in Chapter 2, followed by a relatively detailed description of experimental procedures and results in Chapter 3. Based on these results, possible interpretations of the physics are given in Chapter 4 along with a brief discussion on proposed experiments.

1.2 Introduction to the Section of Wigner Solid

The concept of Wigner crystal was originally proposed by Eugene Wigner in 1934 [40]. In a disorder-free system, as the Coulomb interaction becomes dominant to the kinetic energy, the electron liquid changes into the Wigner crystal. In the limit of dilute 2-dimensional systems, carriers can be localized by the magnetic field, thus terminating the FQH liquid. For convenience, a dimensionless density r_s ($r_s = E_C/E_k$) is widely used for describing the quantum phase in dilute systems, here E_C and E_k are Coulomb energy and kinetic energy, respectively. In GaAs/AlGaAs specimen, some magnetotransport measurements accumulated the evidences for the Wigner solid

[41–44], which exhibits an insulating behavior. In 2DES, Wigner solid phase is observed with a density r_s range $1 < r_s < 3$, which is much smaller than that of 2DHS ($7 < r_s < 15$).

At a high magnetic field, a ground state of FQH liquid was discovered by D. C. Tsui et al [3] in 1982. It is interesting that the original experiments were searching for magnetic-field-induced Wigner crystal. Actually, the competition between the Wigner crystal and the FQH liquid determines the ground state. It is possible that Wigner crystal is reentrant around the FQH liquid phase. In 2DES, the reentrant insulating phase is observed around $\nu = 1/5$ FQH state [43], with $r_s \sim 2$; the reentrant insulating phase is around $1/3$ FQH liquid in 2DHS [42], with $r_s \sim 10$. In our large hole density sample, the reentrant insulating phase is around the $1/5$ FQH state ($r_s \sim 7.6$, between 2 and 10). It is rather amazing that we observed the reentrant insulating phase around $1/5$ FQH liquid. This phenomenon indicates that somehow our hole sample exhibits electron-like behaviors.

Now, we would like to introduce the sliding motion of Wigner crystal. The Wigner solid is pinned by disorder potential. If the external force overcomes the pinning force, the Wigner crystal starts sliding. This phenomenon can be observed by means of electric field, microwave, etc. Under microwave, Chen et al [45] reported the Wigner crystal with the radio-frequency resonances. Here, the harmonic oscillation of Wigner crystal is relatively “soft”. In our hole system measurements, we observed sliding motion with a larger threshold electric field and sharp slopes dj/dE in the non-linear conductance (j : current density). In the “melting” procedure of Wigner crystal, the thermally activated behavior indicates a larger energy gap. These results show us that the sliding Wigner crystal is “harder” under a high magnetic field.

The motivation of this topic is as follows: 1) the large effective mass in a hole

system helps the formation of a Wigner crystal. On the other hand, a high density hole system increases the ratio r_s to ~ 7.6 and reduces the LL mixing. We would like to observe the behaviors of Wigner crystal under high magnetic fields. 2) We hope to measure the conductance and non-linear conductance in the Corbino samples, which eliminates the Hall field in the sample. This will help us to obtain an effective threshold field for the sliding Wigner solid phase. 3) We are interested in the properties of the new type of high quality samples: C-doped (001) quantum well.

The topic of Wigner solid in 2DHS is organized as follows: a brief introduction for background on theory and experiments of Wigner crystal is discussed in Chapter 4. In Chapter 5, principles and details of experimental setup and results on Wigner solid are described. Based on the data, possible interpretations are provided in Chapter 7.

Chapter 2

Background of 5/2 State in GaAs

In this chapter, we will introduce the fundamental background of integer quantum Hall effect (IQHE), fractional quantum Hall effect (FQHE), the discovery of even-denominator fractional quantum Hall state $\nu = 5/2$, and the activation energy (energy gap) measurements.

We would like to describe high magnetic field, low temperature transport in a 2D electron system, which shows the integer quantum Hall effect (IQHE) and the fractional quantum Hall effect (FQHE). The odd-denominator FQHE states and the even-denominator states are both incompressible quantum liquids, but they have completely different ground states and quasiparticle excitations. In excited LLs ($N=1$ and above), anisotropic transport in the vicinity of half-filling factors was observed. Under tilted magnetic field, the half-filling QH states in higher LL give way to the stripe phase. The observed effect is that the in-plane magnetic field ($B_{//}$) governs the orientations of anisotropy at $\nu = 11/2, 9/2, 7/2$ and $5/2$. In particular, the $5/2$ and $7/2$ states are isotropic in the absence of in-plane magnetic field, but can become anisotropic by applying an in-plane field.

2.1 2DEG in GaAs/AlGaAs Quantum Well

GaAs crystals are composed of two elements, Gallium (Ga) and Arsenic (As), which form the Zinc Blende structure. Ga and As each form a face-centered cubic lat-

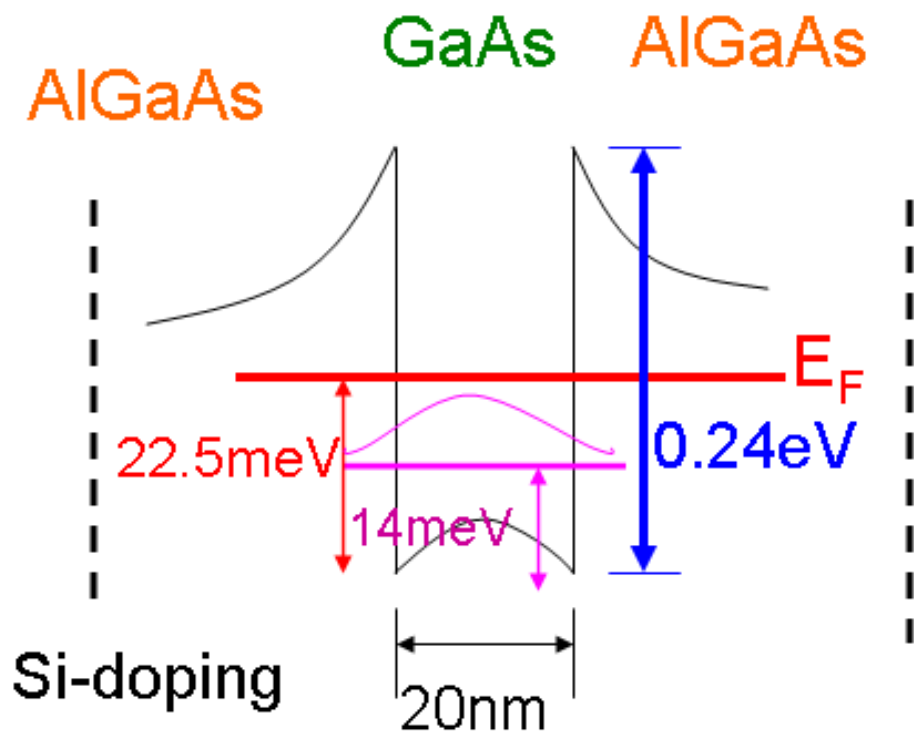


Figure 2.1 : Band diagram of the sample with a 20 nm wide GaAs/AlGaAs quantum well, with the wavefunction below the Fermi level.

tice, which is shifted along the diagonal direction. The crystal structure of the alloy $\text{Al}_x\text{Ga}_{1-x}\text{As}$ (x is the molar fraction of Al) is also Zinc Blende, but with some Ga sites being substituted by Al atoms. By a modern materials growth technique, termed molecular beam epitaxy, a quantum well can be grown by lattice-lattice matched $\text{GaAs}/\text{Al}_x\text{Ga}_{1-x}\text{As}$. Due to the band structure differences between GaAs and $\text{Al}_x\text{Ga}_{1-x}\text{As}$, the electrons are confined in a quantum well. An obvious advantage of a two-dimensional electron gas (2DEG) is that the density of states (DOS) is a constant: $m^*/\pi\hbar^2$ (\hbar is Planck's constant), and the Fermi energy is $n\pi\hbar^2/m^*$. m^* is the effective mass of carriers in the specimen, $0.067 m_e$ in GaAs , where m_e is the mass of a free electron. The DOS of a $\text{GaAs}/\text{AlGaAs}$ quantum well is: 2.8×10^{13} ($1/\text{eV cm}^2$).

2.2 Integer Quantum Hall Effect

In 1980, Von Klitzing observed the IQHE in a 2DEG specimen [2]. At certain filling factors $\nu = i$, (i is an integer), the Hall resistance exhibit a series of plateaus, the values of Hall resistances are proportional to $1/i$, such that $R = R_H/i$. The standard resistance, R_H , is $h/e^2 = 25812.8 \Omega$. On the other hand, an important dimensionless constant, the fine structure constant, is proportional to the standard resistance R_H . At integer filling factors $\nu = i$, the longitudinal resistances drop to zero.

A high perpendicular magnetic field causes quantization in the states of a 2DEG and is denoted as the Landau levels ($N = 0, 1, 2, 3\dots$). According to Schrödinger's equation and the Landau gauge, the Landau level for a 2DES can be expressed as: $E_N = (N + 1/2)\hbar\omega_c$, where $\omega_c = eB/m$ is the cyclotron frequency. The closed cyclotron orbits which come from different Landau levels are located inside the sample. At the sample boundaries, orbits are interrupted by elastic reflection, and edge states

with higher energy than those in the middle move along the boundaries of the sample.

2.3 Fractional Quantum Hall Effect

Compared with the IQHE, the FQHE expresses more collective properties of electrons in 2DES. Under a high magnetic field, at a filling factor of $\nu = 1/3$, the FQHE was discovered by Tsui, Stormer and Gossard in 1982 [3]. For the $1/3$ state, the longitudinal resistance exhibits a very deep minimum very close to zero, and the associated Hall resistance value is $3h/e^2$. Laughlin gives an excellent expression of the model for the FQHE, in which an odd-denominator FQH state (with a filling factor of $\nu = 1/q$) can be understood as an incompressible quantum liquid. Generally, for an odd-denominator FQH state, Laughlin obtains the ground state wave function with a filling factor $1/q$ ($q = 3, 5, 7, \dots$): $\Psi = \prod_{j < k} (Z_j - Z_k)^q \exp(-1/4 \sum |Z_l|^2)$. Here, Z is the electron coordinate in the complex plane. The restriction to odd integer q comes from the requirement of exchange symmetry for the wavefunctions of Fermi quantum liquids. On the other hand, Landau level filling factor can be expressed as: $\nu = \frac{E_F}{\hbar\omega_c}$ (E_F is the Fermi level). For clarity, we need to emphasize the relation between the LL index and LL filling factor: the $\nu = 1/2, 3/2$ states locate in the lowest Landau level ($N=0$), and the states at $\nu = 5/2$ and $7/2$ are in the second Landau level ($N=1$), etc.

In 1987, Willett et al [10], observed a first even-denominator quantum numbers in the FQHE. Strong T -dependence of $\nu = 5/2$ in R_{xx} below 100 mK was thoroughly researched. Simultaneously, the Hall plateau for the $5/2$ state indicated the same T -dependence as R_{xx} . This behavior is the same as that of the odd-denominator quantum number state. From Laughlin's work, the odd-denominator is used to meet the requirement of Pauli's exclusion principle, while the even-denominator may lead

to Fermion pairing. Various theories have indicated that the $5/2$ state has a strong overlap with the Pfaffian wavefunction which supports quasiparticles obeying non-Abelian quantum statistics. Such non-Abelian behavior is pursued theoretically for the purpose of topological quantum computing [14].

One of the specific properties of the Pfaffian is that it must be spin-polarized or partially spin-polarized, as opposed to the spin-singlet, which is spin-unpolarized. Either the Pfaffian (Pf) wavefunction, proposed by Moore and Read [13] to describe the $5/2$ state, or the Anti-Pfaffian (APf) wavefunction [19,20], which is a degenerate state recently proposed by Dimov et al [46] and Feiguin et al [37] (with respect to the Pf), are fully spin-polarized states. On the other hand, there are also paired states which are not fully-polarized: for example, Halperin's $(3, 3, 1)$ state [47].

To date, there is no direct proof for fully electron polarization at $5/2$, but some experiments give evidence for a spin-polarized ground state (*i.e.* Pan et al [30]). Some important discussions resulted from theoretical simulations and calculations. Morf et al [15] showed that the fully-polarized state has lower energy than the spin-singlet state of a finite number of electrons. Park et al [48] found that a polarized Pf is more favorable than a polarized and unpolarized CF sea. Dimov et al [46] concluded by a variational Monte Carlo method, that the Pf has lower energy than the $(3, 3, 1)$ state; Feiguin et al [37] calculated the ground state of the $\nu = 5/2$ FQH state, even for zero Zeeman energy, and found that it is fully-polarized.

2.4 Activation Energy in Higher LLs under a Perpendicular Magnetic Field

The energetics relevant to the quantum Hall system are cyclotron energy $E_\omega = \hbar e B / m^* \propto B$, where $m^* \sim 0.067 m_e$, is the electron effective mass; Zeeman energy $E_Z = g \mu_B \propto B$, where g is the effective g -factor in GaAs, μ_B is the Bohr magneton; and electron interaction energy $E_C = e^2 / \epsilon l_B \propto B^{1/2}$, where $\epsilon = 12.9$ is the dielectric constant in GaAs and $l_B = (\hbar / e B)^{1/2}$ is the magnetic length. Although the bare g -factor $g \sim -0.44$ is small in magnitude, increasing magnetic field favors the E_Z / E_C . On the other hand, the LL mixing $\kappa = E_C / E_\omega$ decreases as $B^{-1/2}$. The Landau-level mixing is characterized by $\kappa = (e^2 / \epsilon l_B) / (\hbar e B / m^*) = l_B / a_B^*$, where $a_B^* \sim 10$ nm is the Bohr radius in GaAs. Xia et al reported [11] an ultralow temperature study of the 5/2 FQHE and other many-particle states (including 12/5) in an ultra-high mobility 30 nm GaAs/AlGaAs QW ($\mu = 3.1 \times 10^7$ cm²/Vs, $n_e \sim 3 \times 10^{11}$ cm⁻²). Choi et al studied systematically the activation gaps of FQHE in the $N = 1$ LL in similar density samples, with a particular emphasis on the role of the disorder plays in the measured gaps [49]. In these “standard” samples the LL mixing parameter $\kappa \geq 1$. Dean et al studied the 5/2 FQHE at $B \sim 2.6$ T in a $n_e = 1.6 \times 10^{11}$ /cm², 40 nm QW [50], corresponding to a stronger LL mixing regime. They found contrasting behavior of the 5/2 and 7/3 FQHE in a tilted field, and discussed the relevance of Zeeman energy and the magneto-orbital effect in interpretation of spin-polarization of the 5/2 state. In the other limit, Pan et al reported [30] a 5/2 FQHE minimum at a B as high as 12.6 T, which is observed in a heterojunction insulated gate field-effect transistor. From the T -dependent amplitude of the 5/2 peak-valley structure, a “quasi-gap” can be defined. The $\Delta_{5/2}^{quasi}$ vs. n_e exhibited a systematic fashion in

which a maximum value of $\Delta_{5/2}^{quasi} \sim 150$ mK is observed around 9 T. This result, when the disorder is taken into account, is consistent with what is to be expected for a spin-polarized FQHE at 5/2 [30].

2.5 Activation Energy in Higher LLs under a Tilted Magnetic Field

The thermal activated resistivity directly determines the fundamental energy gap for a FQHE state. The energy gap can be obtained from the slope of the linear behavior in Arrhenius plot ($\ln(R_{xx})$ vs. $1/T$): $R_{xx} \propto \exp(-\Delta/2T)$. In FQHE state, the energy (Δ) is required to excite the quasi-particle and quasihole pair.

Zeeman energy is proportional to the total magnetic field B_{tot} . In the tilted-field experiments, $B_{perp} = B_{tot}\cos\theta$, where θ is the tilted angle. For a certain FQHE state (ν is fixed), the perpendicular magnetic field is fixed. The total field-dependent energy gap is relevant to the spin differences between before and after the excitation of the quasiparticle and quasihole pair. For a very simple case, the energy gap can be written as: $\Delta = \Delta_0 - g\mu_B B_{tot}\Delta S$, in which Δ_0 is for the case without Zeeman energy, Bohr magneton $\mu_B = 0.67$ (K/T), and the bulk g -factor $g \sim -0.44$ in GaAs. For a spin-polarized ground state of FQH state, if the quasiparticle and quasihole are both spin-polarized, the difference $\Delta S = 0$, and the activation gap should be constant. For a spin-unpolarized ground state, the spin difference $\Delta S = 1$, and $\Delta = \Delta_0 - g\mu_B B_{tot}$. Actually, the above discussion is merely focused on the simplest case, and other factors in the sample are neglected. Pan et al [30] explained for the spin-unpolarized ground state $\Delta = \Delta_0 - g\mu_B B_{tot} - \Gamma$, here Γ is the broadening from disorder; $\Delta = \Delta_0 - \Gamma$ is for the spin-polarized ground state. In the real systems, the measured energy gap

is much smaller than those from calculations, where the disorder in the specimen is neglected. In some experiments [30], the $5/2$ state is investigated at a high magnetic field, and the obtained activation energy ($\Delta_{5/2}$) is even smaller than Zeeman energy.

More recently, Wójs et al [51] reported the Skyrmions in the Moore-Read State at $\nu = 5/2$ state. The Skyrmion of $\nu = 5/2$ state has twice the charge of the quasiparticles (QPs) ($q = 2(e/4) = e/2$), therefore the Skyrmion can be considered as the bound pair of the quasiparticles. The quasiparticles can be trapped by disorder, thereby the binding QP pairs form Skyrmions in a potential well. On the other hand, Wójs et al [51] illustrated that as the disorder strength increase with B , the Skyrmion is stable until a large Zeeman energy (E_Z). The calculation demonstrated for a magnetic field $B \leq 6$ T in GaAs specimen at $\nu = 5/2$ state, with the existence of disorder, quasiholes can bind into Skyrmions. For the sufficient low Zeeman energy, even at the center of the $5/2$ plateau, the ground state is not fully spin-polarized, with the formation of Skyrmions leading to the depolarization. From the discussions above, previous results for lower- B version at $\nu = 5/2$ implicates non-fully polarized or fully-polarized ground states. On the other hand, the higher- B destroyed the Skyrmions, with the fully spin-polarized ground state at $5/2$.

In 2009, Rezayi and Simion [36] calculated and compared the Pfaffian and Anti-Pfaffian ground states in the real sample systems, which include the Landau level mixing. They conclude that the ground state of $\nu = 5/2$ is fully polarized and the Moore-Read state is favored. In our higher electron density samples, we have a smaller value of LL mixing parameter $\kappa \sim 0.8$, and ground state is at least partially spin-polarized (or even fully-polarized), which provide the implications for Moore-Read Pfaffian state.

2.6 Anisotropic Electronic Transport in Higher Landau Levels

Previous work from Fogler et al [26], and Mossener et al [27] suggests that for the half LL filling factors of $N \geq 2$, the ground state is a charge density wave (CDW), or, more specifically, forms a unidirectional “stripe phase”. The Hartree-Fock calculations for $N \geq 2$ showed that the CDW state has lower energies than the Laughlin liquid. It is argued that near a half filling factor the wavelength is of the same order of magnitude as the cyclotron radius.

At the lowest LL half filling factor ($\nu < 2$), including spin-down branch $\nu = 1/2$ and spin-up branch $\nu = 3/2$, the magnetoresistance can be explained as the result of the formation of composite fermions. Jiang et al [7] discovered that the deep minima in the longitudinal resistance at filling factors of $1/2$ and $3/2$ can be observed up to around 10 Kelvin. At the second LL half filling factor ($2 < \nu < 4$), Hall resistance of the spin-down state $\nu = 5/2$ and the spin-up state $7/2$ exhibit a respective FQHE plateau [10]. However, the properties of these FQH states and the underlying physics are not completely understood. At even higher LL half filling factors ($\nu > 4$), states at filling factors $\nu = 9/2, 11/2, 13/2, 15/2$ show a strong anisotropic behavior: the resistance exhibits a peak when current flows along one direction (R_{xx}) and a valley along the 90° direction within the plane of the sample surface, which is defined as R_{yy} . Conventionally, the direction along higher resistance is called the hard direction, and the direction along lower resistance is called the easy direction; for the $9/2$ state, the anisotropic ratio can be up to 100.

The DC transport observations for striped phases at $9/2$ and $11/2$ [12, 23–25] are now further supported by AC (microwave frequency) experiments [52]. For the

third and higher LLs in clean 2DEG GaAs/AlGaAs heterostructures, the transport anomalies are solid and intriguing. These phenomena appear with large anisotropy and are restricted to very low in T .

The samples of GaAs/AlGaAs quantum wells or single-interfaced heterostructures are grown on the [001]-oriented GaAs substrates. Based on the results of transport measurements, it is believed that “easy” direction is parallel to [110] orientation, and that the “hard” direction is along the $[1\bar{1}0]$ crystallographic direction. At half filling factors in higher LLs ($N > 1, \nu = 9/2, 11/2, 13/2, 15/2$), the anisotropic phenomenon is explained as the result from the CDW ground state. This “stripe” phase should have a wavelength of the same order of magnitude as the cyclotron radius. For our 20 nm wide QW, the cyclotron radius is $R_c = \hbar k_F / eB = 130(nm) / B$ (T). From the transport measurements, we estimate the electron density to be $n = 6.3 \times 10^{11} (\text{cm}^{-2})$, and the corresponding Fermi wave vector as $k_F = \sqrt{2\pi n} = 2.0 \times 10^{16} (\text{cm}^{-1})$.

2.7 Transport in Higher Landau Levels under a Tilted Magnetic Field

A tilted magnetic field is a powerful method for research of magnetoresistance. Around forty years ago, the effect of tilted magnetic fields on 2DEG were discussed systematically by Fang and Stiles [53]. In tilted- B experiments, Landau spacing is proportional to the perpendicular magnetic field and Zeeman splitting is proportional to the total magnetic field. The Zeeman energy goes up with increasing total magnetic field for some certain QH fractions (*i.e.* $\nu = 5/2$). In-plane B squeezes the single particle wavefunction which can effectively decrease the QW width and reduce the strength of the 5/2 FQHE [29]. On the other hand, Eisenstein et al [29], discovered the

collapse of the $5/2$ state wave function in the presence of a parallel magnetic field. The $5/2$ FQH state gives way to CDW stripe phase for high in-plane B (Pan et al [12], Lilly et al [25]).

For a tilted magnetic field, the longitudinal resistance shows a different phenomenon, which is considered as the collapse of the FQHE states, typically in the half filling factors FQHE states. Pan et al [12], observed the anisotropic transport (at $T = 40$ mK) around the $11/2$, $9/2$, $7/2$, $5/2$ states, by comparing the differences from before and after the rotation by 90° within the 2DEG sample surface. Their results indicated that under zero tilted magnetic field, $5/2$ and $7/2$ are isotropic, while $9/2$ and $11/2$ are anisotropic. As the in-plane B increases, the anisotropic axes of $9/2$ and $11/2$ are re-oriented, with the peaks generated along the in-plane B orientation, and the anisotropic axes (induced by tilting B) of $5/2$ and $7/2$ also aligned with the in-plane B orientation.

Chapter 3

Experiment of 5/2 State

The experimental setup and data collection is the main focus of this chapter. The necessary sample characterization will also be discussed in this section. Extremely low temperature and very high magnetic field are important conditions for the measurement of FQHE. The tilted magnetic field provides a tunable experimental parameter, the in-plane magnetic field, and is crucial to the project described in this thesis. The majority of the experimental data were obtained at the National High Magnetic Field Lab (NHMFL) in Tallahassee, Florida.

3.1 Experimental Setup

The magnetotransport experiments were performed in a top-loading Oxford He3/He4 dilution refrigerator, which has a base temperature of 20 mK, and the magnetic field, up to 18 T, was provided by a superconducting magnet. The sample was mounted on the platform of the precision mechanical rotator, which can be turned *in situ* by a bellow feedthrough on the top of the top-load probe. The axis of rotation of the platform is perpendicular to the magnetic field axis, so for a rotation angle θ , the perpendicular field to the 2DEG is $B\cos\theta$, and the parallel (or, in-plane) field is $B_{//} = B\sin\theta$ (Figure 3.1). The rotator can be continuously adjusted between $0 < \theta < 360^\circ$. However, since in this research we mainly focus on the state at filling factor 5/2 which occurs at ~ 10 T, a tilted angle up to 50° can be reached for a

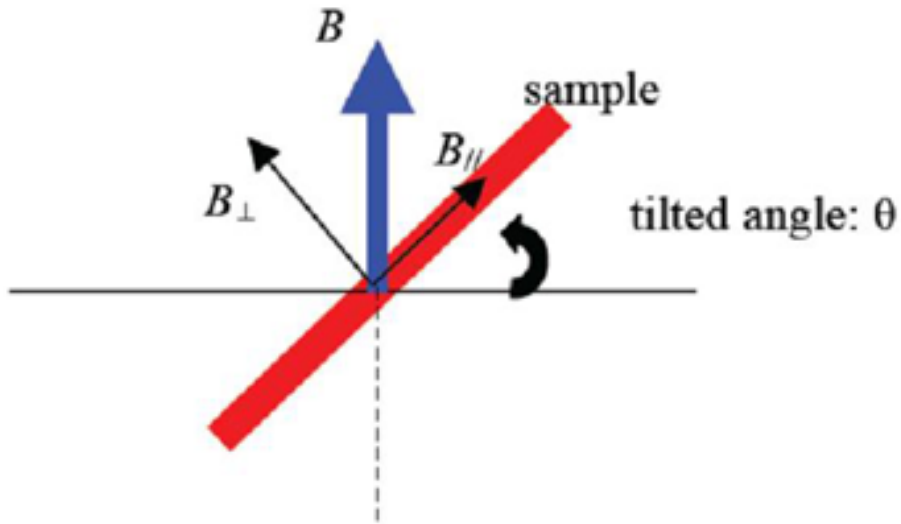


Figure 3.1 : In-plane magnetic field experimental setup, in which the sample surface can be tilted. Zeeman energy is proportional to total B , and Landau level spacing is proportional to $B \cos \theta$.

total magnetic field of 18 T. Our data in a tilted B will be limited to within this range. In T -dependent experiments, it is necessary to raise the temperature around the sample space while keeping the dilution refrigerator in normal operation. This can be achieved by a resistive heater in the tail of sample space; or alternatively, by a resistive heater attached to the He3/He4 mixing chamber. Note that a thermometer is placed in the proximity of the sample, but the thermometer only measures the temperature of the coolant and not the electronic temperature of the sample. To minimize electron heating a small AC excitation current (typically 7 Hz and 10 nA) was applied to the sample.

The Van der Pauw method is widely used for the Hall effect measurement in 2DEG samples. The measurement using the Van der Pauw method requires the thickness of the sample to be less than the length and width. In the Van der Pauw configuration, the resistance of the sample can be measured as follows: voltage can be measured in

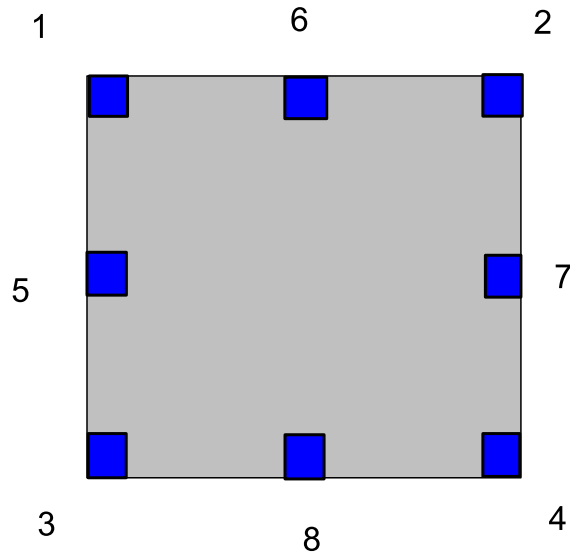


Figure 3.2 : Schematic of the Van der Pauw configuration

one pair of contacts, while current is applied to another pair of contacts. In Figure 3.2, $R_A = V_{12}/I_{34}$, $R_B = V_{13}/I_{24}$, $R_C = V_{34}/I_{12}$, $R_D = V_{24}/I_{13}$, $R_E = V_{56}/I_{78}$, $R_F = V_{67}/I_{85}$, $R_G = V_{78}/I_{56}$, $R_H = V_{85}/I_{67}$. From the van der Pauw's equation, the sheet resistivity can be expressed as: $\rho = \frac{\pi}{ln2} \times 1/8 \times (R_A + R_B + R_C + R_D + R_E + R_F + R_G + R_H)$. For the Van der Pauw configuration with eight contacts, the measurements of the longitudinal contacts include all pairs of the neighbor contacts.

3.2 Sample Characterization

The specimens for our experiments are modulation-doped GaAs/Al_{0.24}Ga_{0.76}As wafers, which are grown by molecular beam epitaxy (MBE) on a (001) GaAs substrate, While it is common for the best modulation-doped GaAs/AlGaAs heterostructures to reach a high electron mobility $\mu > 1.0 \times 10^7$ cm²/Vs, it is a rather challenging task to

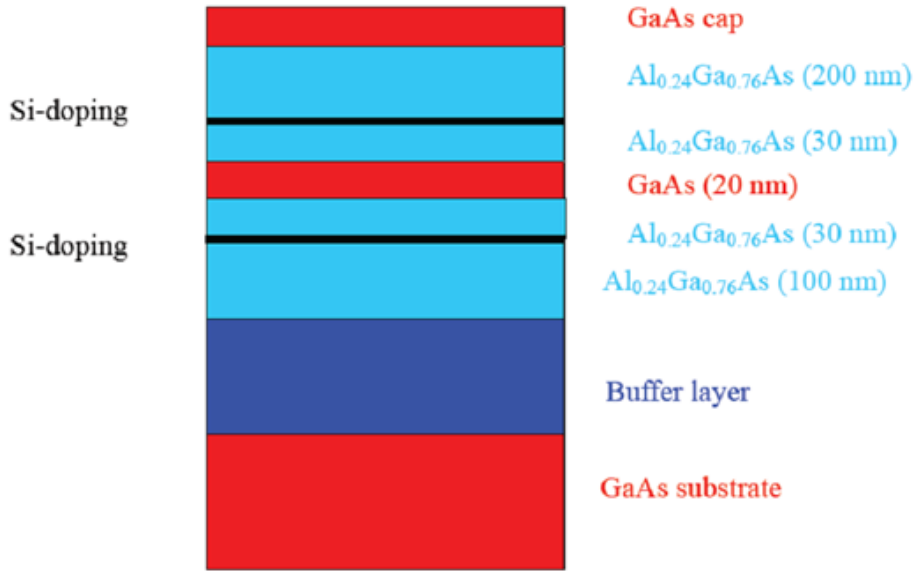


Figure 3.3 : Schematic of the structure of the sample with modulation Si-doped 20 nm wide GaAs/ $\text{Al}_{0.24}\text{Ga}_{0.76}\text{As}$ quantum well (QW-A).

achieve both very high electron density and very high mobility by the present MBE technique. The main trade off is between the need to increase the spacer distance for reducing the impurity scattering, and the need to reduce this distance in order to transfer electron in the QW. A schematic of the 20 nm wide QW structure used for our experiment is shown in Figure 3.3.

After being illuminated with a red LED (bias 10 mA) at $T = 2$ K for 5 minutes, the 20 nm QW sample has a high carrier density of $(6.2-6.3)\times 10^{11}\text{cm}^{-2}$, and the mobility can be up to $1.0\times 10^7\text{cm}^2/\text{Vs}$. The low- T LED illumination, which is associated with persistent photoconductivity in defect centers in GaAs [54], is an effective way to improve the mobility and density homogeneity across the sample.

The procedure to make the Ohmic contacts to 2DEG is as follows: (1) coating solution S1813 with the spinner (with a rotation velocity of 4000 rms, for 50 seconds), soft baking the sample at 90°C for 45 seconds;(2) then processing under ultraviolet

(UV) exposure (for 10 seconds) with SUSS mask aligner MJB4. (3) After hard baking at 100°C for 40 seconds, the samples need to be developed with developer-321 for around 60 seconds. (4) Ge (430Å)/ Pd (300Å)/ Au (870Å) metals were deposited on the sample surface with an E-beam evaporator in the ultrahigh vacuum environment. (5) After metal deposition, the patterns on sample surface are revealed by lift-off in acetone for a couple of minutes. After the lift-off, the samples should be rinsed in methanol and deionized (DI) water.

In this project, we have measured 6 samples, each with a $3mm \times 3mm$ squares cleaved from the wafer. Each square has eight contacts placed at the four corners and on the middle of the four edges.

In order to identify the crystal axis of the sample, we use the defect pit-etching procedure, as briefly described here [courtesy of Yanhua Dai who did the etching experiment, [55] and Appendix B].

We first present data for the quantized Hall plateau measured at $\nu = 5/2$. Figure 3.3 shows the longitudinal resistance R_{xx} minimum and the Hall resistance for a specimen cooled to $T \sim 10$ mK. At a $B \sim 10.4$ T, we observed a Hall plateau that is quantized to the value $(h/e^2)/(5/2)$ within the experimental uncertainty $\sim 0.5\%$. This is the first time that a quantized $5/2$ plateau is reported at $B > 10$ T. Together with a vanishing R_{xx} , these data establish unambiguously a true FQHE gap at $5/2$ in this QW. These results confirm the observation of the $5/2$ FQHE minimum in a magnetic field $B \geq 10$ T first reported in Ref. [30] and strengthen the case for a high- B version of the $5/2$ quantum liquid.

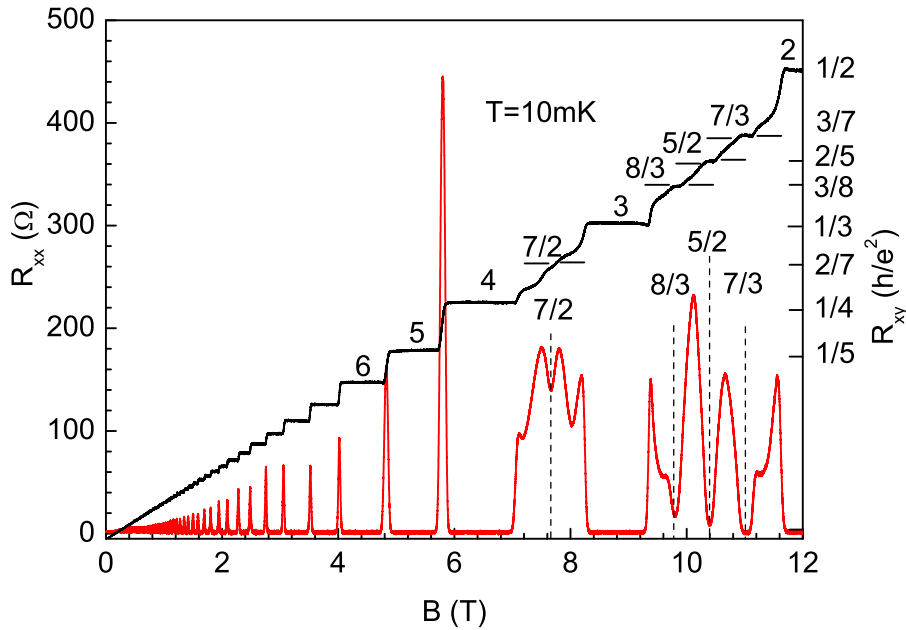


Figure 3.4 : The magnetoresistance in the same 20 nm QW (sample e-QW-A-1) measured at 10 mK is presented, showing the quantized Hall plateaus at $5/2$ and $7/2$, as well as at $7/3$ and $8/3$ (Courtesy of Dr. Tauno Knuuttila [56]).

3.3 Experimental Results in a Perpendicular Magnetic Field

We study experimentally the quantum phases at $\nu = 5/2$ and $7/2$ in the limit of increasing electron density n_e . This thesis will present systematic magnetotransport data in a modulation-doped, high- n_e QW, in which a $5/2$ quantized plateau is observed at a high magnetic field $B \sim 10$ T with a measured activation gap $\Delta_{5/2} \sim 125$ mK. Observation of the FQHE in $B \sim 10$ T and its evolution under a small-angle tilt-field lends support for a spin-polarized ground state at $\nu = 5/2$. The resistances at $\nu = 5/2$ show complex response to the tilted field, which we interpret as resulting from a competition between the quantum Hall liquid and the insulating phase [12] in the tilted field, but the background diagonal resistances can either be isotropic or become anisotropic, depending on the in-plane component $B_{//}$ direction (with respect

Table 3.1 : Electron density, mobility, and activation gaps measured in the fractional quantum Hall states $5/2$ and $7/3$.

Sample	n_e (cm^{-2})	μ (cm^2/Vs)	w/l_B	κ	$\Delta_{5/2}$ (mK)	$\Delta_{7/3}$ (mK)
40 nm QW [50]	1.6×10^{11}	14×10^6	2.5	1.6	262	200
30 nm QW [49]	2.8×10^{11}	10.5×10^6	2.5	1.2	272	206
20 nm QW	6.3×10^{11}	10×10^6	2.5	0.8	125	200
Heterojunction [12]	2.3×10^{11}	17×10^6		1.3	110	100

to the GaAs crystalline axis). Such data indicate a substantial coupling between the collective phases at $\nu = 5/2$ and the GaAs crystal.

Our experiment is in a regime where for $5/2$, $E_Z \sim 3$ K, which is comparable with the predicted gap energy $\Delta \sim 2.5$ K [31], and $\kappa < 1$, corresponding to reduced LL mixing (Table 3.1). The main results were obtained from a modulation-doped GaAs/ $\text{Al}_x\text{Ga}_{1-x}\text{As}$ square quantum well (QW) having a width $w = 20$ nm and $x = 0.24$ in the barrier. After a brief illumination from a red light-emitting diode, QW attained an electron density approximately $n_e = (6.1 - 6.3) \times 10^{11} / \text{cm}^2$, and a mobility $\mu \sim 1 \times 10^7 \text{cm}^2/\text{Vs}$ at $T \sim 0.3$ K. A total of three specimens (labeled as e-QW-A-1,2,3), each of a $(3 \sim 5)$ mm \times $(3 \sim 5)$ mm square, were cleaved from the wafer with edges roughly aligned with GaAs $[110]$ or $[1\bar{1}0]$ axis. Eight Ge/Pd/Au contacts were diffused on the perimeter for magnetotransport measurements. We have measured $R_{xx}(5/2)$ as a function of T (Figure 3.6) and found thermally activated transport behavior in the T -range between ~ 25 mK and ~ 100 mK. These data are illustrated in an Arrhenius plot (Figure 3.7) $R_{xx} \sim \exp(-\Delta_{5/2}/2k_B T)$ (with k_B the Boltzmann constant), yielding a gap value $\Delta_{5/2} \sim 125$ mK. Similar procedure yields a gap at

filling factor value $\Delta_{7/3} \sim 200$ mK. These values are generally inline with that measured from similar mobility, standard density samples of narrow w (see Table 1). For example, in a $n_e = 2.3 \times 10^{11}/\text{cm}^2$, $\mu = 1.7 \times 10^7$ cm²/Vs GaAs/AlGaAs heterojunction, $\Delta_{5/2} \sim 0.11$ K and $\Delta_{7/3} \sim 0.10$ K were reported [12]. On the other hand, no features for 12/5 or reentrant integer quantum Hall effect around the 5/2 [12] were seen in this QW at zero tilt. Overall, while it is clear that the major FQHE states such as 5/2, 7/3, and 8/3 are stabilized, scattering presented due to a narrow width (20nm) in this QW may have obscured the more fragile states, such as 2+1/5 and 2+4/5 states observed in similar mobility but wider QWs (Table 3.1, 30 nm [49] and 40 nm [50] QWs).

Before presenting the systematic experimental results of magnetotransport data measured in NHMFL, it is helpful to review the ultralow temperature magnetoresistance and Hall resistance data for the same QW. The data was measured by Dr. Tauno Knuuttila in an Oxford 1000 dilution refrigerator, at a sample substrate temperature ~ 10 mK. The data show quantized Hall plateaus at filling factor 5/2, 7/2, 7/3, and 8/3, and close to zero magnetoresistances at 5/2 and 8/3. Such data indicate exceptional sample quality at such a high electron density. More importantly, a quantized 5/2 Hall plateau at $B \sim 10.4$ T provides strong hints that the state at 5/2 is unlikely to be spin-unpolarized.

In the rest of this chapter we will present data measured in NHMFL. In Figure 3.5, the resistance in a purely perpendicular magnetic field at 20 mK is displayed, and no anisotropy at $\nu = 5/2, 7/2$ was observed. Around the states at filling factors 9/2, 11/2, 13/2, 15/2, the R_{xx} and R_{yy} show different behaviors. We can see Hall plateaus at 5/2, 7/2 fractions. At $T = 20$ mK, the R anisotropy exists at 9/2, 11/2, but the anisotropic ratio are pretty small ($1 \sim 1.5$), (roughly speaking, it is almost

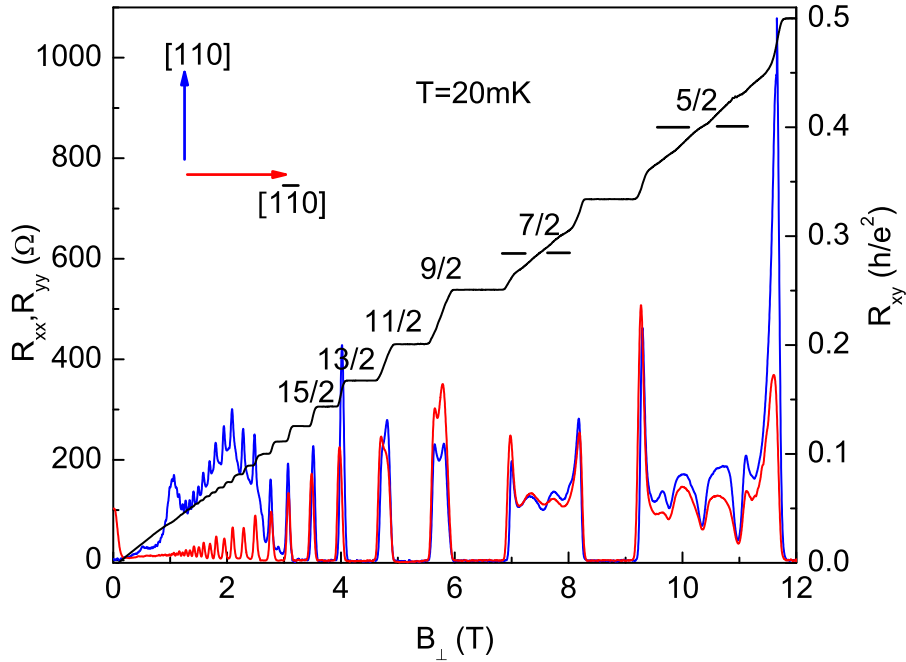


Figure 3.5 : Resistance R_{xx} and R_{yy} of 20 nm wide QW (sample e-QW-A-3) under perpendicular magnetic field

isotropic).

In the data of our 20 nm wide QW sample, there is almost no anisotropy in the absence of in-plane magnetic field around states of $9/2$ and $11/2$, which is consistent with the conclusion of W. Pan et al [12].

From the longitudinal resistance, the density $n = \frac{B\nu}{h/e}$ can be calculated, where h/e is the flux quantum. For example, at filling factor $5/2$, we obtained the density of $n = \frac{10.4 \times 5/2}{4.136 \times 10^{-15} (m^{-2})} = 6.28 \times 10^{11} (cm^{-2})$. On the other hand, we can also calculate the density from the slope of the Hall resistance vs. B : $n = \frac{B}{e\rho}$, it is around $6.30 \times 10^{11} (cm^{-2})$. It can be seen that these data agree very well.

Figure 3.6 shows the temperature dependent of the $5/2$ and $7/2$ states, with T ranging from 20 mK to 300 mK. At extremely low T , from 20 to 300 mK, near $5/2$, R_{xx} exhibits similar features for the states of filling factors $8/3$ and $7/3$. As T increases

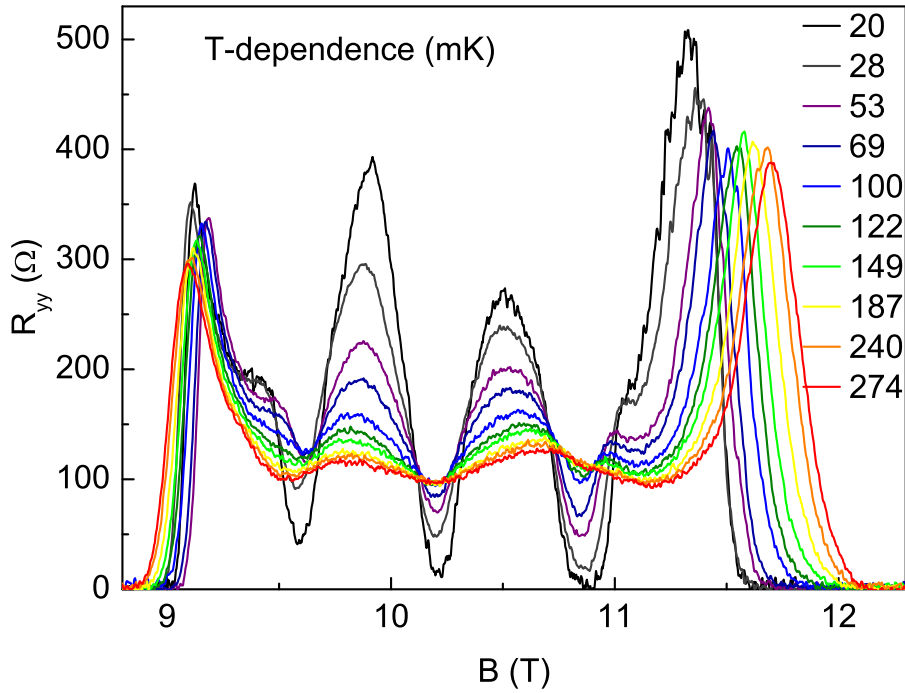


Figure 3.6 : R_{yy} of 20 nm wide QW (sample e-QW-A-2) as a function of temperature (between 20mK and 300 mK) for perpendicular magnetic fields.

the ΔR (the difference between the deep minimum at $\nu = 5/2$ and the median of vicinity peaks) goes down. Around the $7/2$ state, lowering the temperature causes an overall increase in resistances over range $3 < \nu < 4$. The difference in resistances between the minimum of $7/2$ and the two nearby maxima shrinks as temperature goes up. It is intriguing that with increased T , the gap around $\nu = 3$ becomes a little narrower. Generally speaking, in Figure 3.7 the fractions $5/2$ and $7/3$ have a similar T -dependence: the resistances of $8/3$, $7/3$ and $5/2$ decrease with increasing temperature. Based on our measurements, the $5/2$ state and the $7/2$ state have distinct T -dependent behaviors.

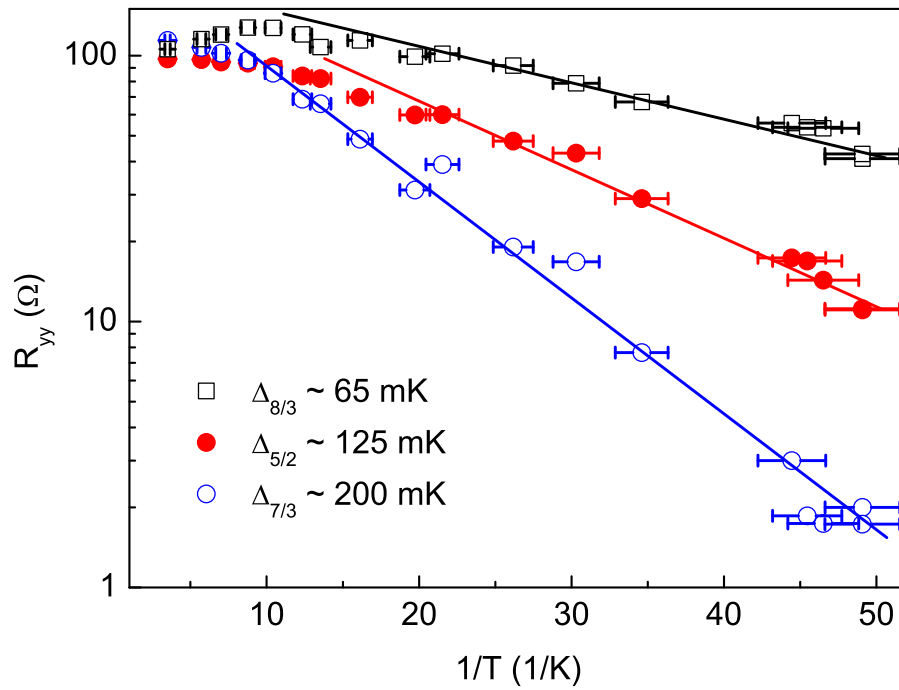


Figure 3.7 : Under perpendicular magnetic fields, the temperature-dependent resistance of 8/3, 5/2, and 7/3 states, exhibit the logarithm behaviors: $\ln(R_{xx}) \propto \exp(-2\Delta/k_B T)$, we obtained the activation energies Δ for 5/2, 7/3, and 8/3 states are 125 mK, 200 mK, and 65 mK, respectively.

3.4 Experimental Results in a Tilted Magnetic Field

In this section, we would like to study the changes of the activation energies with the increasing Zeeman energy. In real measurements, the isotropic transport configuration is more convenient for comparing resistance under various tilted angles. We measured the longitudinal resistances R_{yy} along the crystalline axis [110], which exhibit the isotropic resistances. It should be mentioned that the in-plane magnetic field $B_{//}$ is also along the [110] crystalline orientation. For small tilted angles, $0^\circ < \theta < 10^\circ$, the amplitudes of T -dependent resistances for $5/2$, $7/3$, $8/3$ states decrease with the in-plane magnetic fields; for a fixed angle, the magnetoresistances of $5/2$, $7/3$, $8/3$ FQHE states increase with temperature. For tilted angle $\sim 10^\circ$, the $\nu = 5/2$ and $8/3$ states saturate; and longitudinal resistance of $\nu = 7/3$ still increases with temperature. For higher tilted angles, $13^\circ < \theta < 30^\circ$, the resistances decrease with temperatures at $\nu = 5/2$ and $8/3$. For the measured largest angle $\sim 30^\circ$, the resistance of $7/3$ state remains stable under $20 < T < 300$ mK.

Tilt-field data reveal the perplexing response of the $5/2$ FQHE state under a small tilt-angle ($\theta < 30^\circ$). While the FQHE is found to weaken with respect to tilt, the background resistances around $5/2$ are dramatically different from previous studies [12,23]: the resistance tensor become anisotropic starting from $\theta \sim 10^\circ$ when the $B_{//}$ is aligned with [110] (Figure 3.20), but isotropic (up to at least $\sim 40^\circ$) for $B_{//}$ aligned with $[1\bar{1}0]$ (Figure 3.21). Such data indicate a strong bias from the GaAs crystal, an effect which was reported for $9/2$ but was absent for $5/2$ [12,23]. Figure 3.18 shows a plot of R_{xx} (R_{yy}) as a function of $B_{//}$. The ratio at $5/2$ ($7/2$) can reach ~ 25 (~ 75) for anisotropic case, whereas ~ 1 for the isotropic case. We have carefully studied the evolution of the $5/2$ Hall plateau in increasing tilt (Figure 3.18). Remarkably, starting with a zero-tilt at $B_\perp = 10.4$ T, the plateau can persist up to a tilt of $\sim 25^\circ$.

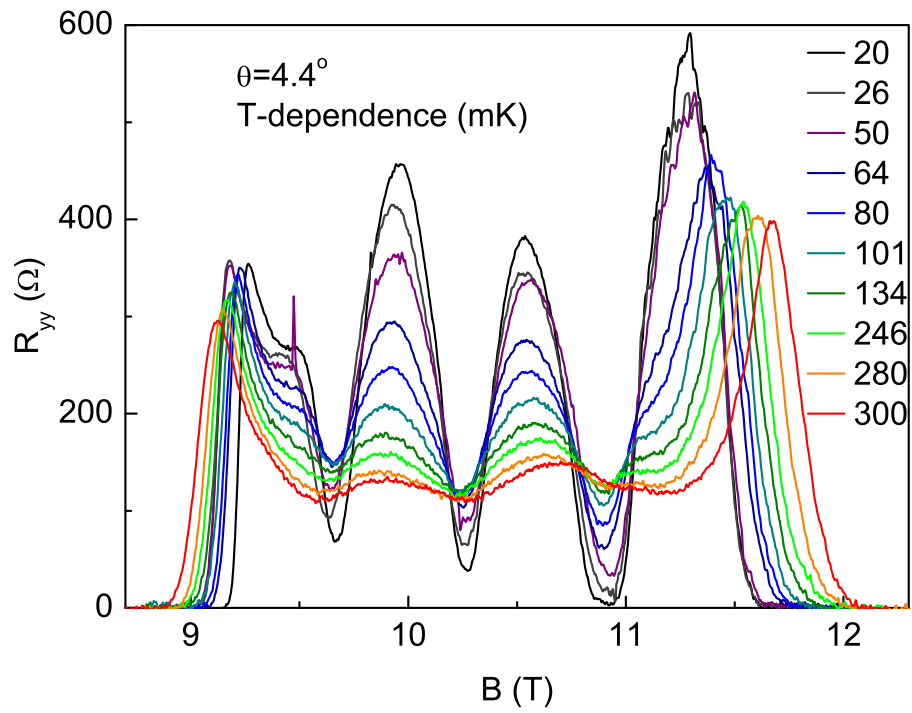


Figure 3.8 : Longitudinal resistance R_{yy} as a function of temperature (between 20 mK and 300 mK) for a tilted angle ($\theta \sim 4.4^\circ$).

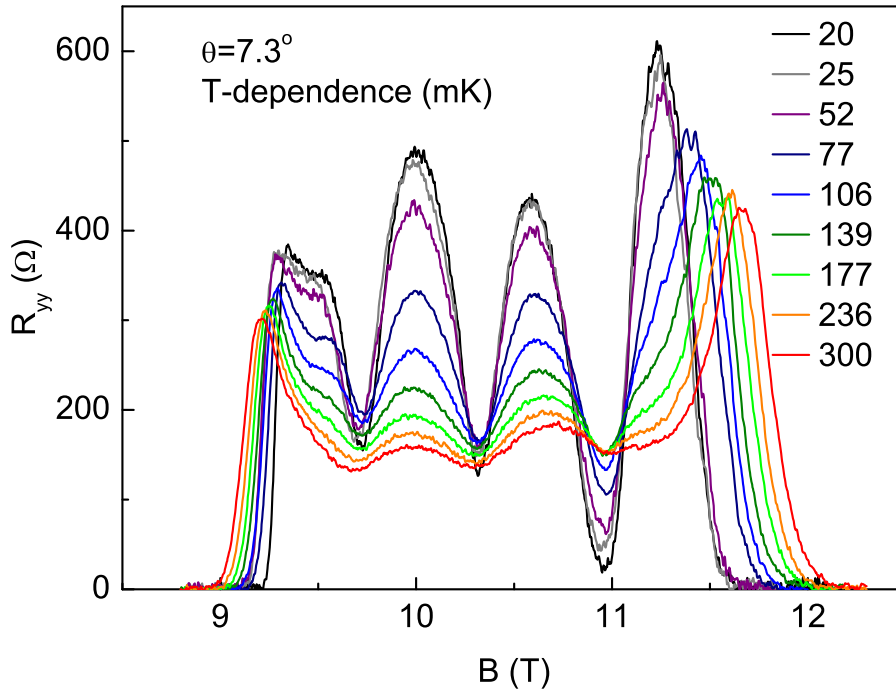


Figure 3.9 : Longitudinal resistance R_{yy} as a function of temperature (between 20 mK and 300 mK) for a tilted angle ($\theta \sim 7.3^\circ$).

At $\sim 30^\circ$, its derivative $B \times (dR_{xy}/dB_\perp)$ shows a sharp minimum at $5/2$, indicating characteristic residual features from the quantum liquid.

Observation of a stable paired FQHE at 10 T has explicit implications for proposed Moore-Read Pfaffian wave function (or Anti-Pfaffian) being the possible ground state at $\nu = 5/2$. We should first discuss the measured gap value $\Delta_{5/2} \sim 125$ mK. According to a recent numerical calculation [31], a spin-polarized MR energy gap in the limit of vanishing LL mixing equals to $\Delta_{theory} \sim 0.016 e^2/\epsilon l_B$, which is approximately 2.5 K in our case. Empirically, such value is subtracted by a level broadening as in [12, 30, 49, 50], which can be estimated from the onset of Shubnikov de Haas (SdH) Oscillation ($\Gamma_{SdH} = \hbar/\Gamma_{SdH}$). A $\Gamma_{SdH} \sim 1.5$ K determined in this QW could partially account for a large reduction of the measured gap from the theoretical prediction.

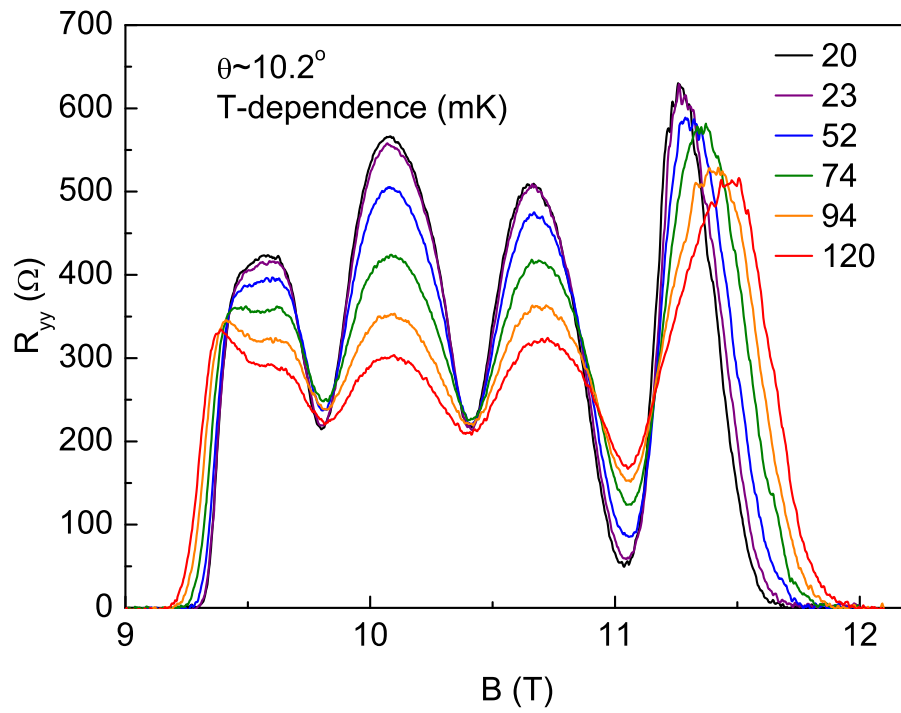


Figure 3.10 : Longitudinal resistance R_{yy} as a function of temperature (between 20 mK and 300 mK) for a tilted angle ($\theta \sim 10.2^\circ$).

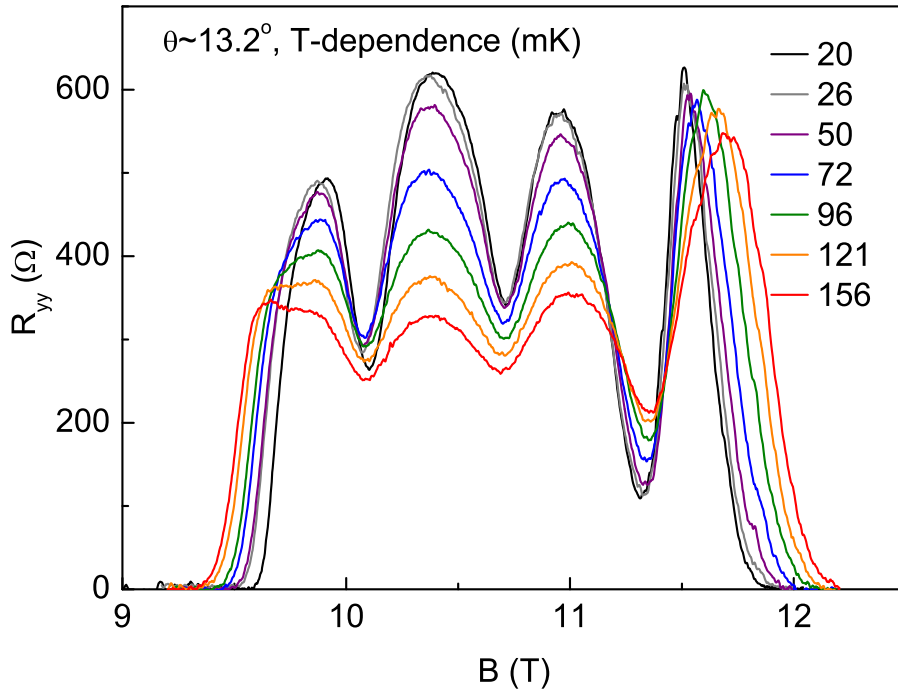


Figure 3.11 : Longitudinal resistance R_{yy} as a function of temperature (between 20 mK and 300 mK) for a tilted angle ($\theta \sim 13.2^\circ$).

We propose that in our 20 nm QW, short-range scattering from the GaAs/AlGaAs interface, which is amplified at high B , may play an important role in gap reduction. Experiments in similar density but wider w QWs should help to address this issue. More over, increasing w/l_B from 2.5 (present QW) to ~ 4 should optimize the overlap between the $5/2$ wave function and Pf, according to a recent theoretical study [18,33].

Since at 10 T the Zeeman energy $E_Z \sim 3$ K is already larger than the $\Delta_{theory} \sim 2.5$ K, it is unlikely that a spin-unpolarized state could be stabilized. Additional evidence can be seen by analyzing the energetics in small tilt. The tilt-field experiments at $B \sim 10$ T render a large increment δE_Z of Zeeman energy even in a small tilt-angle θ , therefore it is instructive to examine the plateau behavior in relation to δE_Z . Assuming that to begin with, the $5/2$ FQHE is spin-unpolarized, and using a bulk

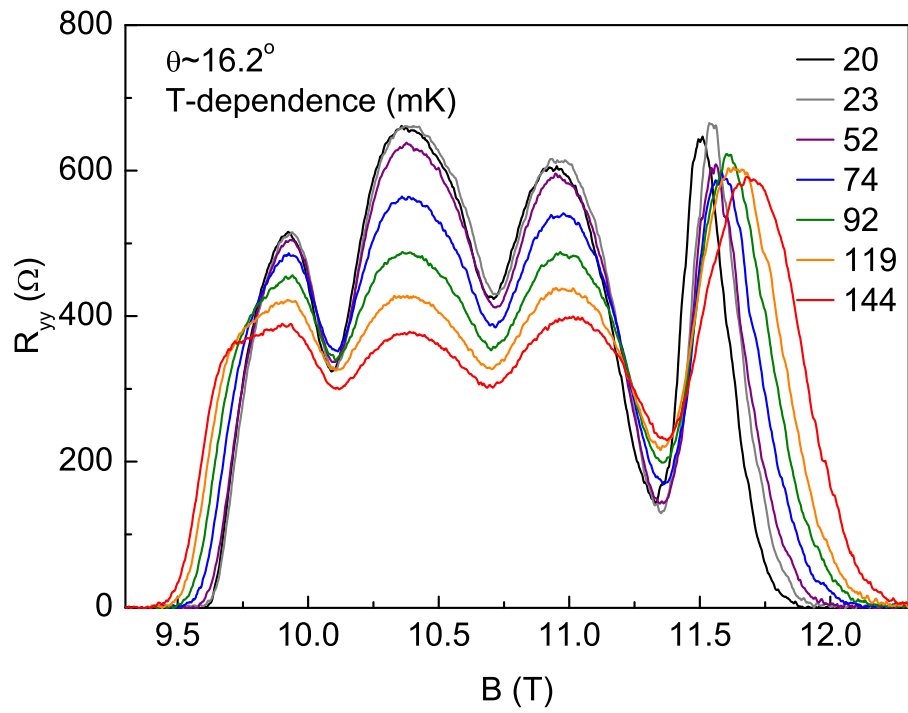


Figure 3.12 : Longitudinal resistance R_{yy} as a function of temperature (between 20 mK and 300 mK) for a tilted angle ($\theta \sim 16.2^\circ$).

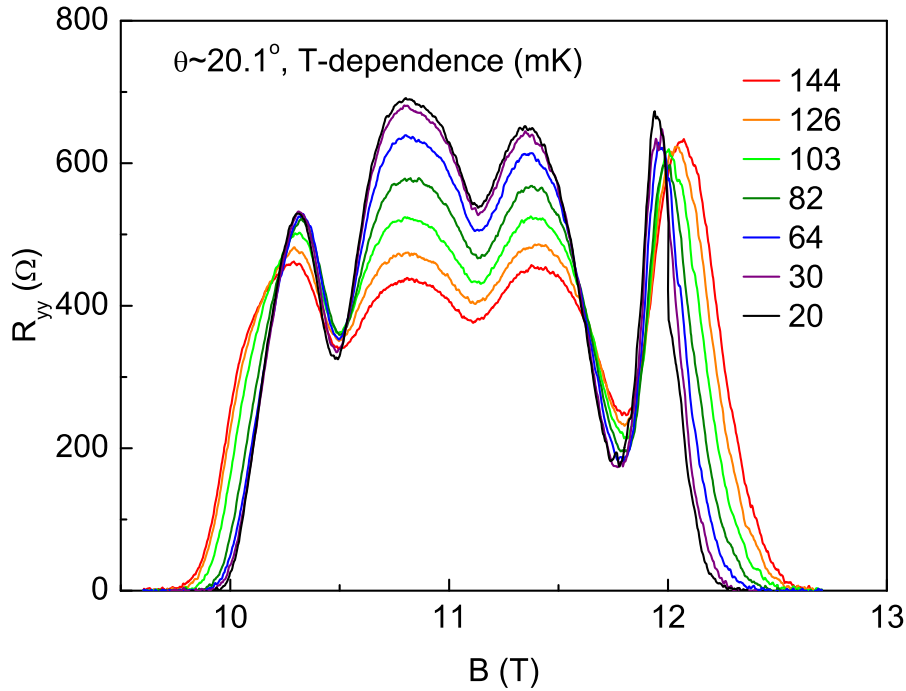


Figure 3.13 : Longitudinal resistance R_{yy} as a function of temperature (between 20 mK and 120 mK) for a tilted angle ($\theta \sim 20.1^\circ$).

g-factor $g \sim -0.44$, we found that $\delta E_Z \sim 0.32$ K for $\theta = 25^\circ$, and ~ 0.48 K for 30° . Such energy cost is a factor of (2 – 3) of the measured $\Delta_{5/2} \sim 0.125$ K at zero tilt. We interpret that this result strongly suggests a spin-polarized or partially-polarized FQHE at $5/2$ in $B \sim 10$ T.

To quantitatively access the energy gaps as a function of tilt θ , we have measured temperature dependence of magnetoresistance in tilted magnetic field. In order to minimize the complications caused by anisotropic resistance background, we choose here to apply the $B_{//}$ along [110]. Figure 3.16 shows the data set for R_{yy} ; similar data were observed for R_{xx} . Systematic evolution of R_{yy} at $5/2$, $7/3$ and $8/3$ indicate a general trend for this QW: all three states tend to diminish with increasing θ . In the meantime, the resistance peaks around $5/2$, as well as those around

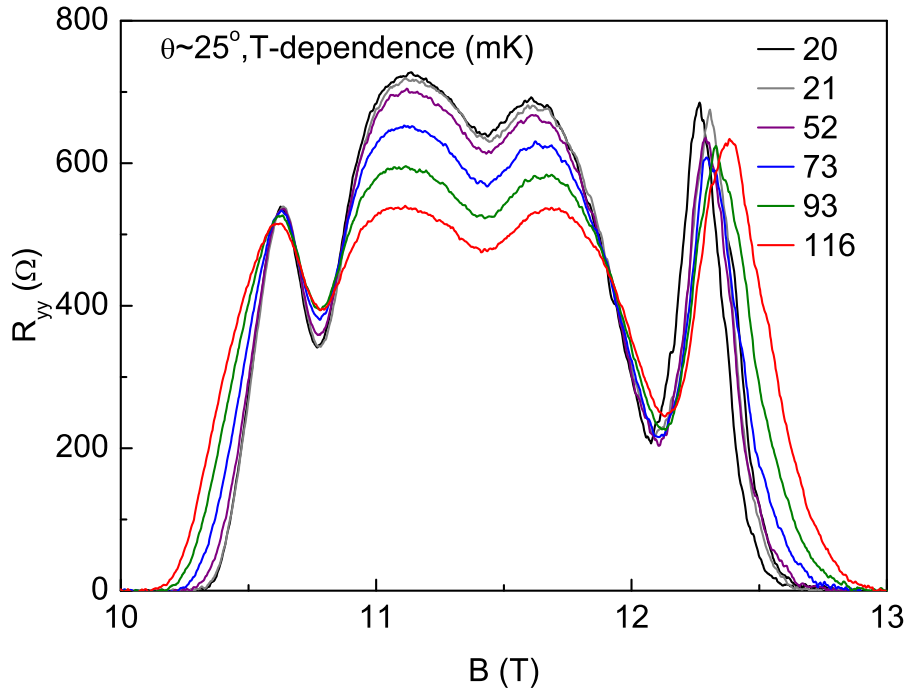


Figure 3.14 : Longitudinal resistance R_{yy} as a function of temperature (between 20 mK and 120 mK) for a tilted angle ($\theta \sim 25^\circ$).

$7/3$ and $8/3$, tends to strengthen. This can be seen clearly for small tilt angles (Figure 3.16, 3.17), where at 7.3° , the $R_{yy}(5/2)$ and $R_{yy}(8/3)$ become essentially temperature-independent, whereas the peaks around $5/2$ are strongly temperature-dependent. This indicates that a tilted field favors the insulating phases [29] and to a certain degree, the diminishing of $5/2$, $7/3$, and $8/3$ FQHE states has to include the influence of nearby insulating phases. For small θ ($\theta = 0^\circ, 4.4^\circ, 7.3^\circ$), we determined the activation gap as shown in Figure 3.17, (the right panel). For $\theta > 10^\circ$ we determined the quasi-gap from the amplitude, S , of the resistance peak-valley structure as a function of temperature [30]. In the Figure 3.17, the T -dependent R_{yy} under tilted angles: $4.4^\circ, 7.3^\circ$ are illustrated in the left panels. We determined the quasi-gap as the function of the resistances peak-valley amplitudes S . Here $S = R_{min}/[(P_1 + P_2)/2]$,

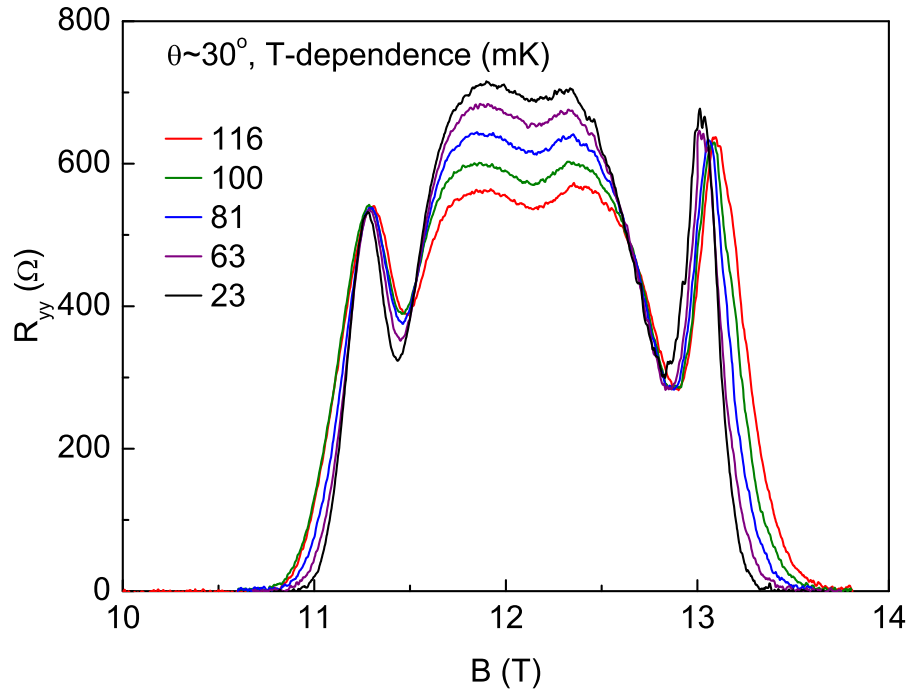


Figure 3.15 : Longitudinal resistance R_{yy} as a function of temperature (between 20 mK and 120 mK) for a tilted angle ($\theta \sim 30^\circ$).

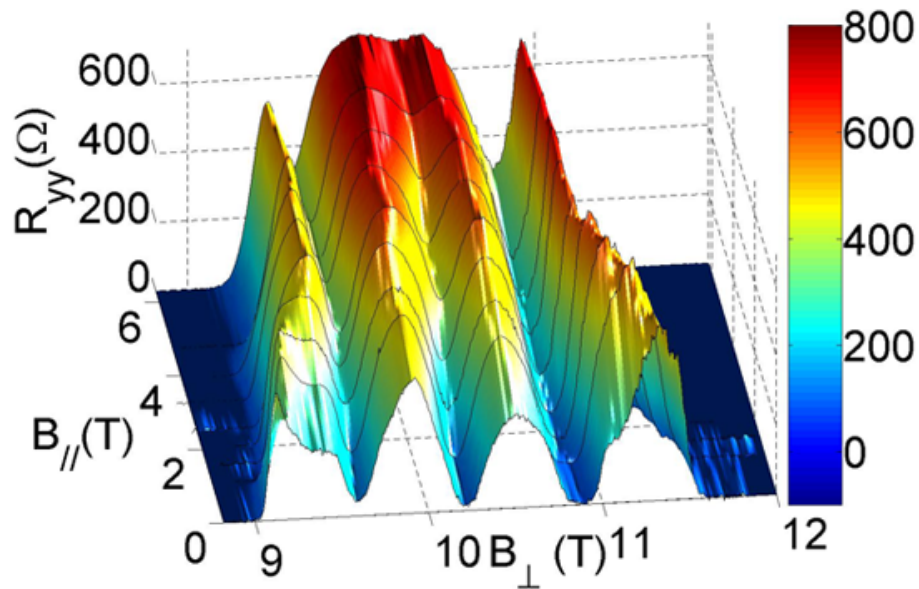


Figure 3.16 : The 3-dimensional figure of longitudinal resistances (R_{yy}) under various in-plane magnetic fields.

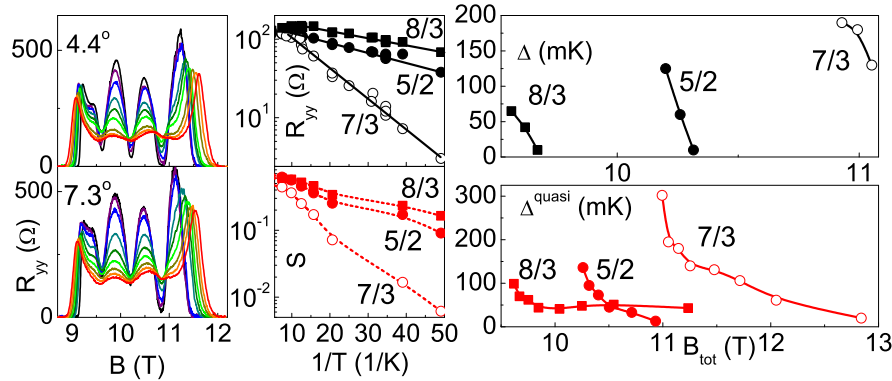


Figure 3.17 : energy gaps Δ (and quasi gaps Δ^{quasi}) of $8/3$, $5/2$, $7/3$ under various tilted-magnetic fields.

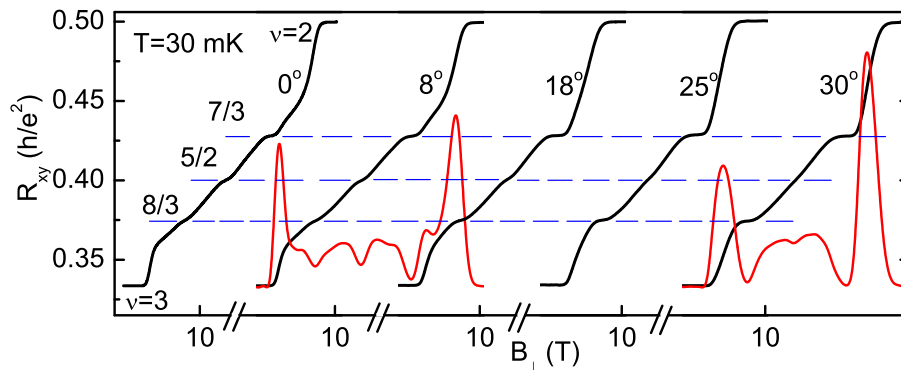


Figure 3.18 : The Hall resistivity (of e-QW-A-3) under various tilted angles: 0° , 8° , 18° , 25° , 30° ; and two red traces are derivatives $B \times dR_{xy}/dB$ for 8° and 30° , respectively.

P_1 and P_2 are the resistances of the two nearest peaks, and R_{min} is the resistance of the minimum. Following these procedures we found that all three FQHE states, $5/2$, $7/3$, and $8/3$ tend to weaken in the tilted magnetic field. This conclusion is in contrast to that from a low-density QW [50], where $5/2$ and $7/3$ show contrasting response to a tilted magnetic field.

3.5 Anisotropic and Isotropic Magnetoresistances under Perpendicular and Tilted Magnetic Fields

The specimen are mounted on the sockets (on sample holders) in two different orientations: (1) the parallel magnetic field along the hard direction (which has higher resistances) is named as “configuration A” in our experiments. (2) the sample is then rotated by 90° , with the in-plane magnetic field along the easy direction (lower resistance), which is called “configuration B”. The configurations will be discussed again in the following data analysis sections.

For a perpendicular magnetic field, we measured the resistance around $5/2$ and $7/2$ FHQE states with two current orientations (Figure 3.19): current is along crystalline axis $[110]$ and $[1\bar{1}0]$, respectively. The $\nu = 5/2$ and $7/2$ exhibit isotropy for a perpendicular, which is consistent with previous results [23, 24]. At a low temperature around 30 mK, we also measured the magnetoresistance R_{xx} and R_{yy} at various tilted angles, respectively (Figure 3.20 and 3.21). In the anisotropic experiments, we load the Van der Pauw sample with one configuration ($B_{//}$ along $[110]$) for tilted fields measurements. After unloading the sample, it was re-oriented in the socket, and re-soldered. The sample was now in the other configuration: $B_{//}$ along $[1\bar{1}0]$.

We now turn to the anisotropic and isotropic magnetoresistances of $9/2$ and $11/2$ state in the GaAs/AlGaAs QWs, which are rather puzzling [12, 23–25, 38]. At low temperatures and for a perpendicular magnetic field, we measured the 20 nm and 25 nm wide quantum wells, respectively, which exhibit different anisotropic behaviors at $9/2$ and $11/2$ states (Figure 3.19). We have checked different pairs of contacts in several specimens and found that they consistently lack definite anisotropy at $9/2$ and $11/2$ states in this high density sample ($n_e \sim 6 \times 10^{11} \text{ cm}^{-2}$). For comparison, we

have measured magnetoresistances in 25 nm wide QW-B, which has a lower electron density $n_e \sim 3.5 \times 10^{11} \text{cm}^{-2}$. In the standard density sample (25 nm wide QW-B), we observed characteristic shapes of peaks and valleys at $9/2$ and $11/2$ with an anisotropic ratio $r \sim 240$ ($\nu = 9/2$) and $r \sim 110$ ($\nu = 11/2$). The data are shown in Figure 3.19 for a magnetic field range from 2.5 T to 4 T. We noticed that from previous reports [23, 24] in heterojunction samples of a lower density $n_e \sim 2 \times 10^{11} \text{cm}^{-2}$ (mobility $\mu \sim 8 \times 10^6 \text{cm}^2/\text{Vs}$) such a ratio is > 1000 . We found a dramatic reduction of the low-temperature anisotropy at $9/2$ (and at $11/2$) as a function of electron density.

We interpret the observed reduction of the magnetotransport anisotropy at $9/2$ state (and $11/2$ state) as a signature of quantum melting of striped phases in the presences of increasing quantum fluctuations [28]. The quantum Hall stripes are thought to be intrinsically unstable against the modulation of widths along the length, therefore a quantum melting process can occur even at very low T , accompanied by low energy excitations. The inverse LL index ($1/N$) is a primary parameter for characterizing quantum fluctuation [28].

The traces around $\nu = 9/2$ and $\nu = 11/2$ under various tilted magnetic field (Figure 3.24 and 3.25, respectively) were measured for another sample (e-QW-A-3), from the same wafer. For the $B_{//}$ from 0 to ~ 16 T, the anisotropic ratio of $\nu = 9/2$ state has a range from 1.5 – 3 (configuration A), and a range from 0.8 – 1.5 (configuration B). Similarly, the anisotropy of $\nu = 11/2$ state (under tilted angle) is rather weak, the anisotropic ratio has a range from 2 – 4 (configuration A), and a range from 1.8 – 1.3 (configuration B). Generally speaking, for the high perpendicular $B \sim 5.5$ T (4.5 T), the $\nu = 9/2$ (and $\nu = 11/2$) states is isotropic under both perpendicular and in-plane magnetic field.

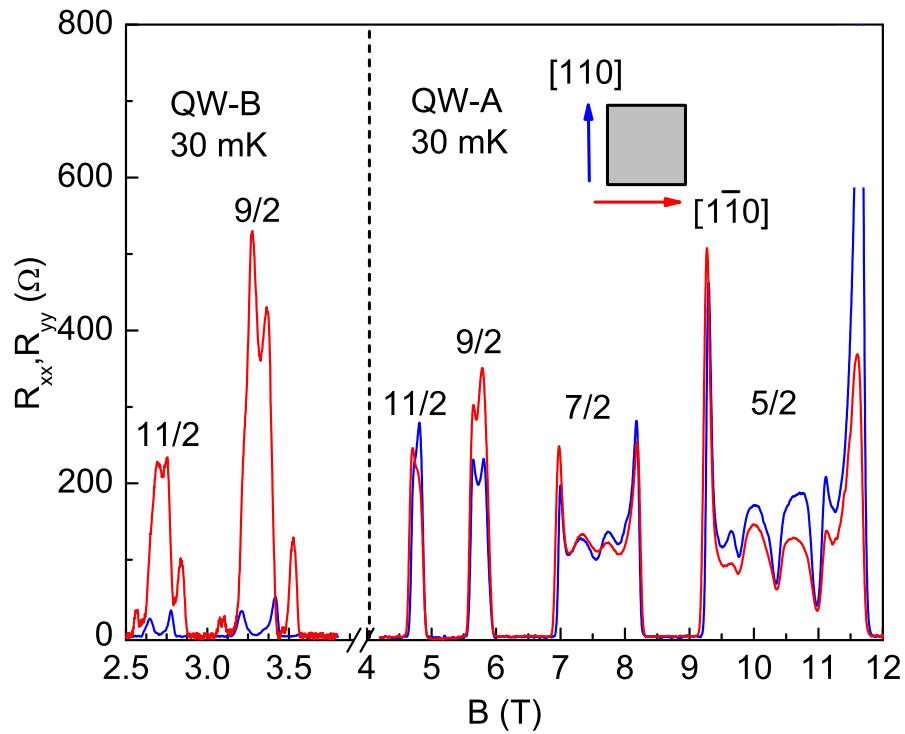


Figure 3.19 : The magnetic resistance R_{xx} (solid, red) and R_{yy} (dotted, blue) in sample 20nm QW (sample e-QW-A-2) measured in a perpendicular magnetic field, respectively along orthogonal crystalline axis $[1\bar{1}0]$ and $[110]$, are shown. The inset depicts schematically the measurement axis. For comparison, the data for sample e-QW-B is shown for the magnetic field range cover $9/2$ and $11/2$.

Figures 3.20 and 3.21 exhibit anisotropic resistances under tilted magnetic fields, with the tilted angle ranging from 0° to around 50° . For the transport under perpendicular B , the transport anisotropy is discernable for the $5/2$ and $7/2$ states. We can conveniently define the longitudinal resistances as R_{xx} and R_{yy} . From our results, we conclude that the anisotropic transport is not induced by the in-plane B orientation (under zero tilted angle).

Now let us discuss the cases with the in-plane field along the x (or y) direction which is named as configuration A (or B). We can start with discussion of $9/2$ and $11/2$ states. In configuration A, R_{xx} corresponds to $I //$ parallel B (current is perpendicular to tilted axis). For both $\nu = 9/2$ and $11/2$, the maximum of R_{xx} is developing with increasing in-plane B . Similarly, for R_{xx} measured in configuration B, the resistance has the same situation under various tilted angles. For R_{yy} of a nearby side for the configuration A, applied current is perpendicular to the parallel component of B . The features split into peaks with a dip in the center. The intensity of shoulders and split peaks diminish gradually with increasing in-plane B , with the tiny peaks left in the end.

For R_{yy} around the $\nu = 7/2$ state of configuration A, as in-plane B increases, the FQHE features diminish gradually, which is replaced by a developing minimum. Simultaneously, the Hall resistance exhibits no plateaus around a filling factor of $7/2$. To the contrary, as in-plane B increases R_{xx} is replaced by a strong peak. The anisotropy shown in the $7/2$ state for configuration A is believed to originate from the in-plane B . In the other configuration, R_{xx} near the $7/2$ state develops a shoulder and a tiny peak grows smoothly on R_{yy} with increasing tilt angle. However, there is no anisotropy as was observed in configuration B.

In the vicinity of the $\nu = 5/2$ state, R_{xx} (in both configuration A and B) and R_{yy}

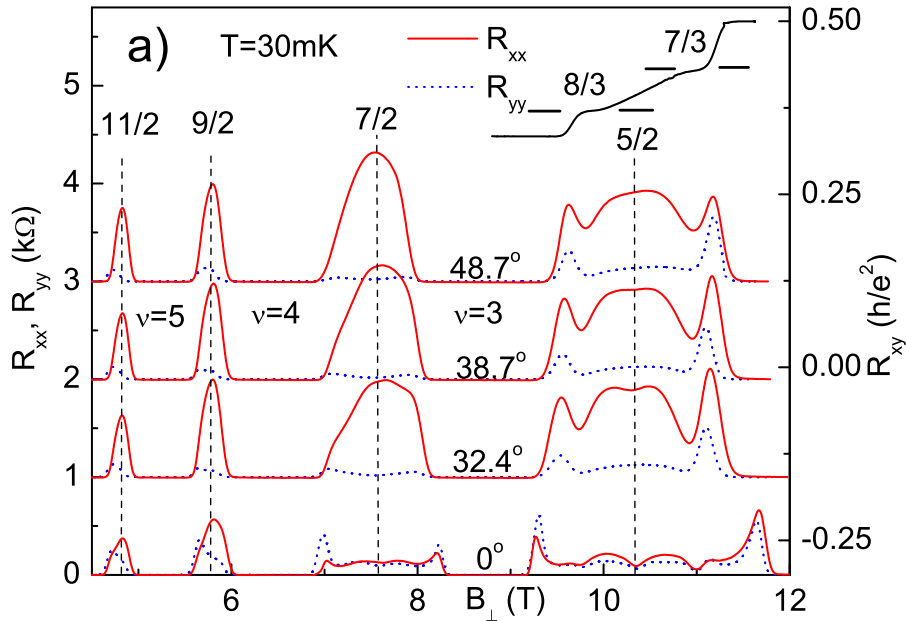


Figure 3.20 : R_{xx} (solid line) and R_{yy} (dashed line) (of Sample e-QW-A-3) under various tilted angles (configuration A). The top trace is Hall resistance under tilted B , and the plateaus at filling factors of $7/3$ and $8/3$ are very clear.

(in configuration B) exhibit maxima in the center as the in-plane B goes up. R_{yy} in configuration A exhibits a low plateau in the center. The FQHE minimum at $\nu = 5/2$ disappears with increasing in-plane B , and turns into a maximum at the end. During the whole tilting procedure, the Hall resistance plateaus prove that FQH states exist in the $\nu = 7/3$ and $8/3$ states.

We also notice that (in Figures 3.20 and 3.21) the width $\delta\nu/\nu$, of the $\nu = 3$ plateau increases linearly with the in-plane magnetic field: $\delta\nu/\nu$ varies from 0.09 to 0.16 as $B_{//}$ increase from 0 to ~ 10 T. On the contrary, $\delta\nu/\nu$ for $\nu = 5$ remains almost constant (~ 0.12) as $B_{//}$ increases from 0 to ~ 6 T.

Figures 3.22 and 3.23 show the anisotropic properties at $\nu = 5/2$ and $7/2$, respectively: R_{xx} and R_{yy} for the two specific filling factors versus the in-plane magnetic

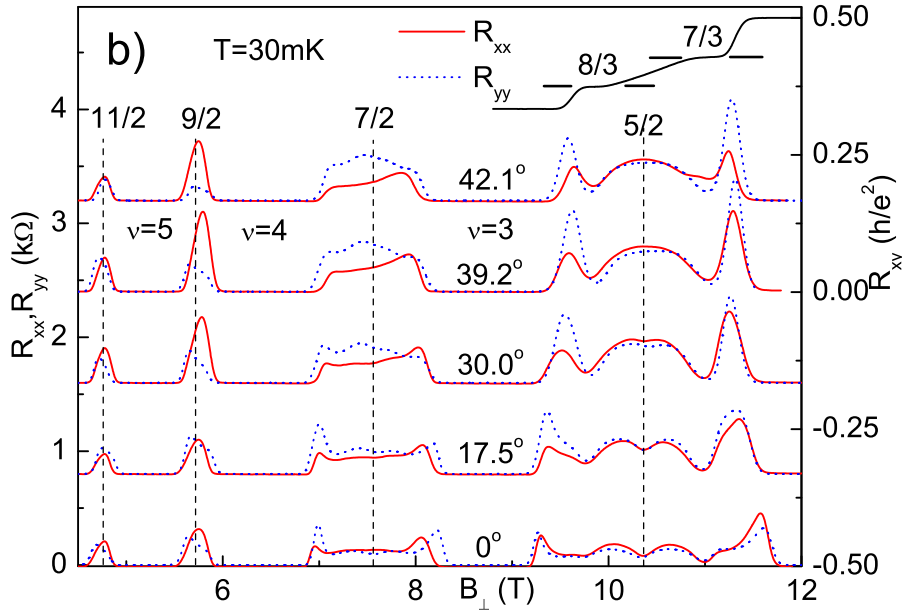


Figure 3.21 : R_{xx} (solid line) and R_{yy} (dashed line) (of sample e-QW-A-3) under various tilted angles (configuration B). The top inset is Hall resistance under tilted B , and the plateaus at filling factors of $7/3$ and $8/3$ are very distinct.

field. For $\nu = 5/2$, before the specimen rotates within the sample surface, the amplitudes of R_{xx} and R_{yy} are rather close to each other at $B = 0$, and then separate as the parallel B increases. The ratio between R_{xx} and R_{yy} can be up to 100 for the $7/2$ state, which corresponds to the previous accumulated results. After the specimen is rotated by 90° within the specimen surface, the R_{xx} and R_{yy} are always kept close to each other. They cross at the position of $1 < B_{//} < 2$ T. From the anisotropic measurement, the ratios of R_{xx} at $\nu = 5/2$ between the anisotropic maximum and minimum values are between $10 \sim 20$.

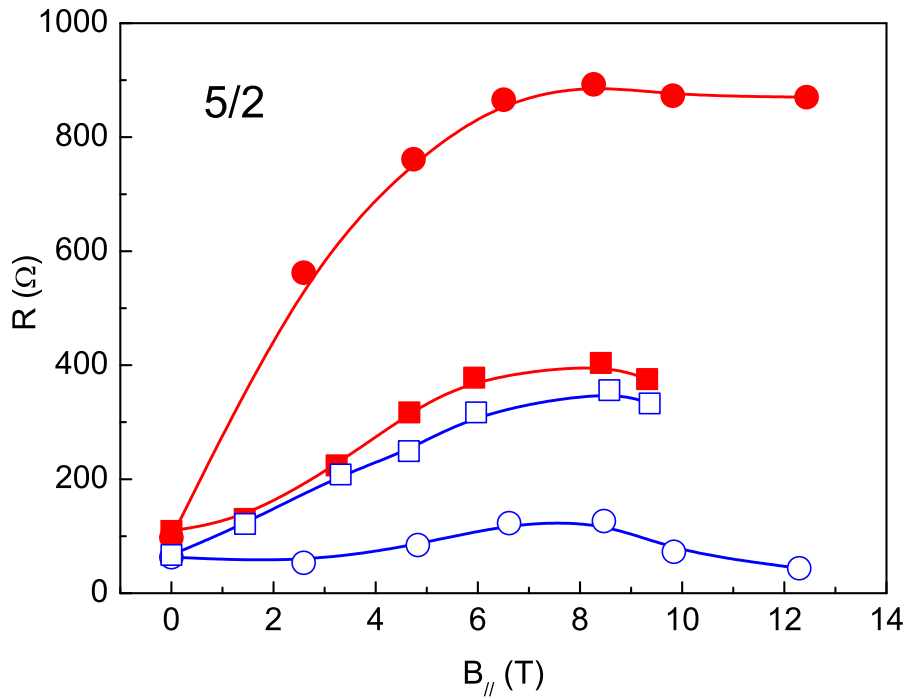


Figure 3.22 : The resistances of states with a fractional filling factor of $5/2$ (of sample e-QW-A-3) under various in-plane magnetic field. R of configuration A (circled trace) exhibits large anisotropy, the anisotropy ratio is around 10; on the other hand, R of configuration B (rectangled trace) exhibits isotropic behavior. In the plot, the symbols are presented as: R_{xx} in configuration A (red-circled curve), R_{yy} in configuration A (blue-circled curve); R_{xx} in configuration B (red-squared curve), R_{yy} in configuration B (blue-squared curve).

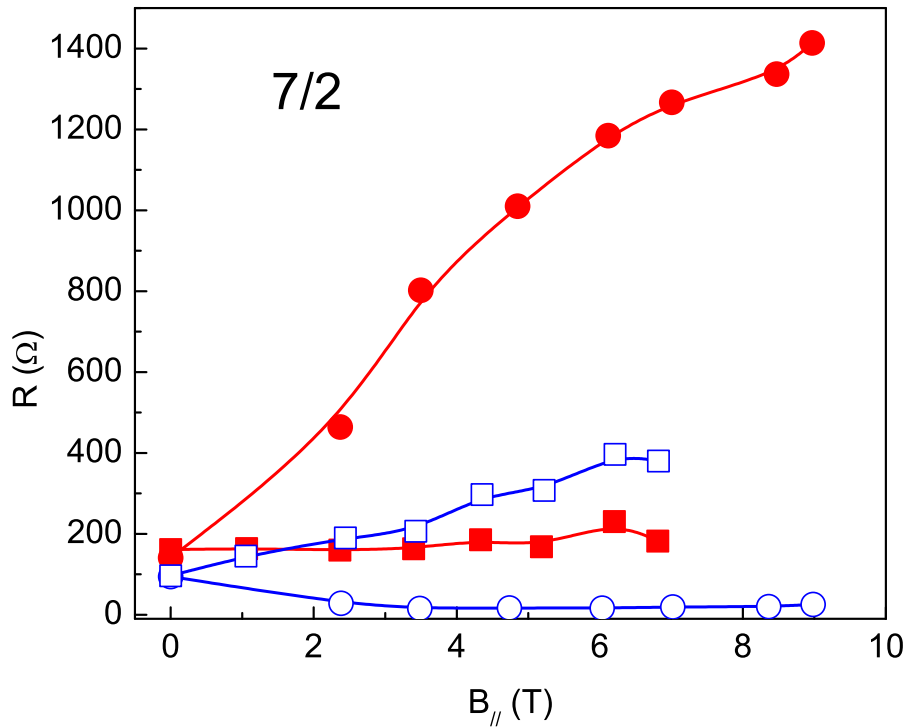


Figure 3.23 : Longitudinal resistances of $7/2$ (of sample e-QW-A-3) under various in-plane magnetic field. R of configuration A (circled trace) exhibits large anisotropy, the anisotropy ratio is larger than 10; on the other hand, R of configuration B (rectangled trace) exhibits isotropic behavior. In the plot, the symbols are presented as: R_{xx} in configuration A (red-circled curve), R_{yy} in configuration A (blue-circled curve); R_{xx} in configuration B (red-squared curve), R_{yy} in configuration B (blue-squared curve).

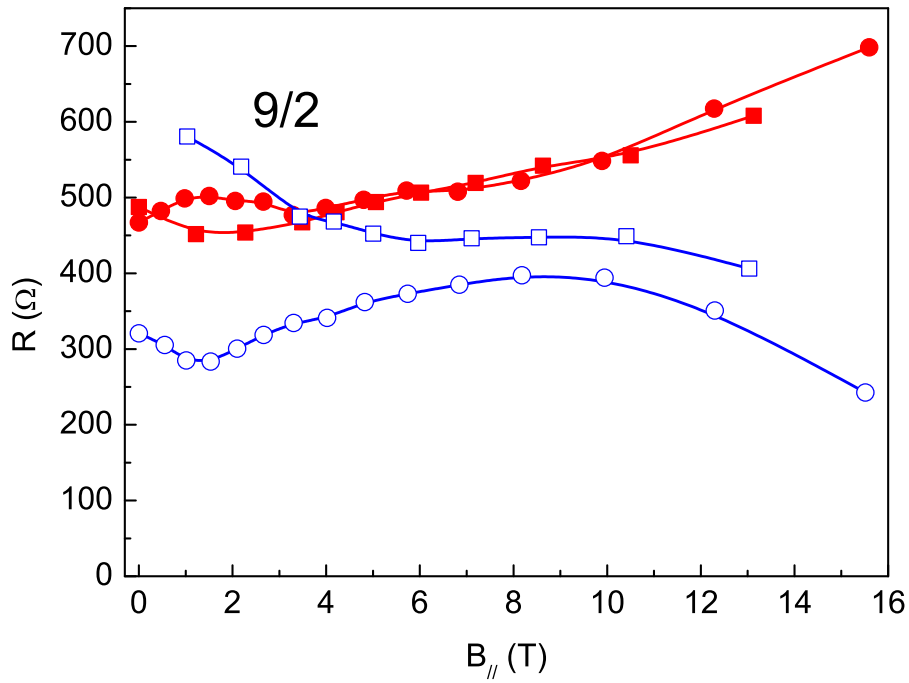


Figure 3.24 : The magnetoresistance R_{xx} (solid symbols) and R_{yy} (open symbols) (of sample e-QW-A-2) are shown for sample c at filling factor $9/2$, as a function of the in-plane magnetic field $B_{//}$; the circle represent the data for $B_{//}$ applied along the $[\bar{1}\bar{1}0]$ axis; the square represent the data for $B_{//}$ applied along the $[110]$ axis.

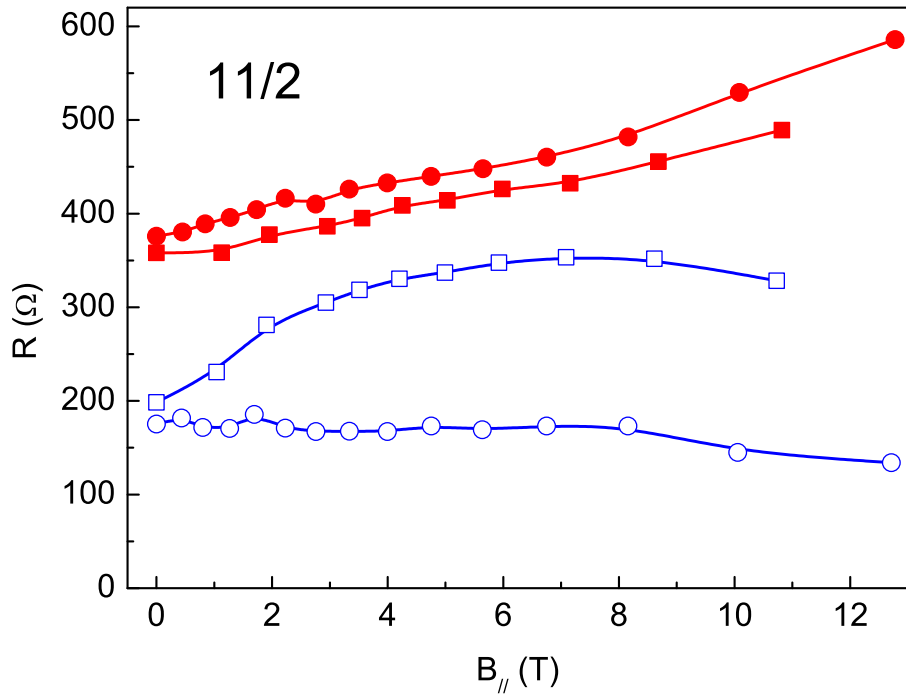


Figure 3.25 : The magnetoresistance R_{xx} (solid symbols) and R_{yy} (open symbols) (of sample e-QW-A-2) are shown for sample c at filling factor $11/2$, as a function of the in-plane magnetic field $B_{//}$; the circle represent the data for $B_{//}$ applied along the $[1\bar{1}0]$ axis; the square represent the data for $B_{//}$ applied along the $[110]$ axis.

3.6 Discussion

At present, the observed magnetotransport properties at $5/2$ and other higher LL half-fillings are not fully understood. However, these data hint at several important influences that have not been explored in previous experiments. We present a brief discussion in the following paragraphs.

1) The $5/2$ FQHE state remains robust for substantially higher B , indicating that the ground state is unlikely to be spin-unpolarized. The role of Zeeman energy can only be quantitatively evaluated by energy gap measurements, which should be performed systematically at low temperatures.

2) The relevance of striped phases at $9/2$ and $11/2$ seems to be weakened for increasing electron density. It is reasonable to think that the striped phases are not the lowest energy states under our experimental conditions, but can become relevant with some modification of interactions by tilting.

3) Although the exact nature of it is not clear, it seems that a symmetry breaking mechanism, originating from the GaAs crystal, is operational not only for the $N = 2$ LL, but also for $N = 1$ LL. This has not been realized prior to our experiment.

Cooper et al [38] did systematic experimental work on orientational symmetry-breaking mechanisms in high Landau levels, *i.e.* $\nu = 9/2, 11/2$. Neither the micron-scale surface roughness nor the precise symmetry of the quantum well structure are important factors leading to symmetry-breaking. The “hard” transport direction is parallel to $[1\bar{1}0]$, while “easy” direction is parallel to $[110]$. Tong et al [57], obtained the crystalline orientations by various wet and dry selective etching process for GaAs/AlGaAs/InGaAs pseudomorphic modulation-doped field effect transistor (MODFET). The etching technique is a good method of illustrating the morphology and crystalline orientations of certain layers of the specimen. From the morphology

obtained by scanning electron microscopy, we make sure the $[1\bar{1}0]$ crystalline direction of the sample is still parallel to the “hard” direction, while the $[110]$ axis is parallel to the “easy” transport direction. Nevertheless, the rather small anisotropic ratio indicates that the anisotropy is very weak.

From the data for a 20 nm wide QW specimen with a high electron density in Figures 3.20, 3.21, 3.22, 3.23, 3.24, and 3.25, we compared our results with the previous work of Pan et al [12]. Without any tilted B , (1) the R_{xx} around $\nu = 9/2$ and $11/2$ are isotropic, and (2) features around $\nu = 5/2$ and $7/2$ are isotropic, which confirmed the results of [12]. (3) Under increasingly tilted B , the features around $\nu = 9/2$, $11/2$ induced anisotropic electronic transport; the peaks always appear when the applied current is along the “hard” crystalline orientation. (4) Under in-plane magnetic field, the states around $\nu = 7/2$ induced anisotropic transport. (5) However, under increasing parallel B , the features of the state $\nu = 5/2$ disappear gradually, and the anisotropy exists in one configuration, while isotropy exists in the other. It is very natural to connect the “hard” orientation in (3) to 2D crystalline orientations, thus it is necessary for us to clarify. Simultaneously, from our measurements, (3) and (5) contradict Pan et al [12]. Actually, in Pan’s work, the states of $9/2$ and $11/2$ reorient the anisotropic axis, with the peaks developing when the current is along the in-plane B . With in-plane B , the anisotropy exists in both configurations.

In our measurements, the $5/2$ diagonal resistances in a high in-plane B either remain isotropic or become strongly anisotropic. Together with the $\nu = 5/2$ plateau observed at 10 T, our data suggests a new regime for electron transport in higher LLs.

Chapter 4

Conclusions of 5/2 State Experiments

We observed a quantized 5/2 Hall plateau at a high $B \sim 10$ T for the first time, and determined the transport activation energy (or energy gap) from temperature activated transport. In a perpendicular magnetic field, the energy gap of $\nu = 5/2$ is ~ 125 mK, with accompanied results: $\Delta_{8/3} \sim 65$ mK, $\Delta_{7/3} \sim 200$ mK. For a small tilted angle from 0° to $\sim 30^\circ$, the energy gap decreases with increasing in-plane magnetic field. The plateau behavior in a small tilt-angle range is inconsistent with spin-unpolarized ground state at 5/2 if a Zeeman mechanism with a bulk g -factor of GaAs is assumed. In tilted magnetic field ($\sim 25^\circ - 30^\circ$), the increment of Zeeman energy δE_Z is much larger than activation energy. We believe that the high- B version $\nu = 5/2$ ground states is not spin-unpolarized, which lead to the implication for the Moore-Read Pfaffian wave function [36].

We studied the transport at the filling factor $\nu = 5/2, 7/2, 9/2, 11/2$ in a high electron density GaAs/AlGaAs quantum well, where these states are observed in a high magnetic field of about twice the previous reported values. The morphology of the sample surface obtained by using SEM, and the orientations of the sample are consistent with the conclusions of Cooper et al [38]. The $\nu = 5/2$ and $7/2$ states exhibit anisotropy for the in-plane magnetic field $B_{//}$ along $[1\bar{1}0]$, isotropy for $B_{//}$ parallel to $[110]$. Based on experimental results, we compared the anisotropic transport R_{xx} and R_{yy} in both 20 nm and 25 nm wide QWs. In perpendicular magnetic fields, the anisotropy ratios of $\nu = 9/2$ and $11/2$ are the function of electron

density: for the low electron density ($n_e \sim 3.5 \times 10^{11} \text{ cm}^{-2}$), the anisotropy ratio is $r \sim 240$ ($\nu = 9/2$) and ~ 110 ($\nu = 11/2$), for the high electron density ($n_e \sim 6.3 \times 10^{11} \text{ cm}^{-2}$), the transport is isotropic.

Chapter 5

Background of Wigner Crystal

5.1 Wigner Crystal

The concept of Wigner Crystal was originally proposed by Wigner in 1934 [40]: in a disorder free system, the electron liquid can be turned into a lattice of electrons, in which the Coulomb energy dominates the kinetic energy. In dilute 2D electron or hole systems, existence of Wigner crystal can be observed [43, 58–60]. In the two dimensional carrier systems, the Coulomb energy is proportional to the square root of carrier density: $E_C \sim n^{1/2}$; on the other hand, kinetic energy is proportional to the density. Conventionally, we introduce a dimensionless density r_s ($r_s = E_C/E_k$), which is an important parameter in the observation of the insulating phase in dilute systems. Coulomb energy is expressed as: $E_C = 4\pi\epsilon\epsilon_0(\pi n)^{-1/2}$, and the kinetic energy (E_k) is equal to the Fermi energy (E_F): $E_F = \pi n \hbar^2 / m^*$. In the absence of magnetic fields, the parameter r_s can also be expressed as the average distance between particles measured in units of effective Bohr radius: $r_s = (\pi n)^{-1/2} / a_B^*$, where a_B^* is the effective Bohr radius, and $a_B^* \sim 10.2$ nm in electron system, $a_B^* \sim 1.7$ nm in hole system (by assuming $m^* \sim 0.5m_e$). The effective mass of 2DHS ($\sim (0.4 - 0.5)m_e$) is significantly larger than that of 2DES ($0.067m_e$). As a result, WC solid phase, which has been observed in Ref. [41–44] occurs for rather small ratio of r_s ($1 < r_s < 3$) for 2DES as compared to that of 2DHS ($7 < r_s < 15$).

In the cases of weak pinning, the sliding motion of the Wigner Solid can be driven

by external force. This type of Wigner solid phase can be analog to the sliding CDW systems in superconductor [61]. The threshold, pinning frequency and coherent length are the most important parameters in describing the system [61, 64, 65]. Zhu et al [66, 67] reported some theoretical results on the domain size and threshold of sliding WC under a high magnetic field. In 2004, Chen et al [45] reported the WC oscillations with radio frequency under a low magnetic field. In our measurements, we observed the sliding Wigner solid under a high magnetic field around $1/5$ FQHE state, displaying a large threshold in solid phases.

5.2 Magnetotransport Measurements on Wigner Solids

We shall first focus on the reported experiments on Wigner solid phases in 2D electron systems and hole systems. A Wigner Crystal in a 2D electron system was studied at the Helium surface [62, 63]. In the transport measurements [41, 44], the longitudinal resistivity of WC solid phase (in 2DES and 2DHS sample) was as large as $\sim 1\text{M}\Omega$. Goldman et al [44] observed evidence of the Wigner crystal in the two-dimensional electron system, with a density of $n = (5.0 - 6.0) \times 10^{10} \text{ cm}^{-2}$. In this experiment, longitudinal magnetoresistance, an Arrhenius plot of resistance vs. T and four-terminal differential resistance dV/dI were obtained. Li et al [41, 58], reported the magnetoresistance and derivative resistance (dV/dI) (or differential conductance) in the low density GaAs/AlGaAs 2DES ($n = 6.6 \times 10^{10} \text{ cm}^{-2}$). In the experiment, the magnetoresistance exhibits a reentrant insulating phase around $\nu = 1/5$, with a diminishing resistance R_{xx} at a low $T \sim 22 \text{ mK}$. In derivative resistance (dV/dI) measurements (including 2-terminal and 4-terminal measurements), the trace exhibits linear behavior (at the $\nu = 1/5$ state); for the LL filling factors deviating from $\nu = 0.2$, (i.e. $\nu = 0.187, 0.194, \text{ and } 0.214$), the derivative dV/dI display strong nonlin-

ear features. Simultaneously, the relevant current noise power density (ΔS_i) is also discussed: at $\nu = 0.194, 0.214$, data classify a threshold voltage for the noise signals; at $\nu = 0.2$, the threshold is rather weak. Figure 5.1 (Sajoto et al [43]) exhibits the magnetoresistances R_{xx}, R_{xy} in a dilute 2DES at a base $T \sim 22\text{mK}$. The magnetotransport displays FQHE liquid at $\nu = 1/5$ state, with a quantized Hall plateau and a diminishing longitudinal resistance for low temperature. However, in the vicinity of $\nu = 1/5$ FQHE state, the observed resistance $R_{xx} \sim (1-10) \text{ k}\Omega$, or even larger, while, the accompanied Hall resistivity R_{xy} deviates from the quantized Hall resistance $(h/e^2)/(1/5)$. In 1996, Du et al [68] reported the transition from the $\nu = 2/9$ fractional quantum Hall effect to the reentrant insulating phase around $\nu = 1/5$. Previous reports indicated that the ground state at $\nu = 1/5$ in the GaAs/AlGaAs samples with electron density: $0.4 \times 10^{11} < n < 1.1 \times 10^{11} \text{ cm}^{-2}$ is the FQH liquid. The ρ_{xx} of $\nu = 1/5$ exhibits the activated behavior, which is a signature of FQHE liquid [58]. For the cases of $\nu < 1/5$ and $\nu > 1/5$, ρ_{xx} increases with decreasing T , with an insulating phase emerging at base T .

Generally speaking, in the 2DHS samples, a reentrant insulating phase locates around $\nu = 1/3$. In 1991, Santos et al [42] reported the observation of Wigner solid phase in a low density ($p \sim 4 \times 10^{10} \text{ cm}^{-2}$) two-dimensional hole system. Compared to the results of 2DES, the reentrant insulating phases locate around $\nu = 1/3$ FQHE state. Figure 5.2 displays the resistance of 2DHS: the insulating phases are located on both sides of the $1/3$ FQHE liquid. As temperature decreases, the resistance (R_{xx}) of the insulating phases in the vicinity of $\nu = 1/3$ drops dramatically. This report interpreted that the larger LL filling factor $\nu = 1/3$ around the insulating phase comes from the larger Landau level mixing (LLM) in the heavier hole system in GaAs specimens: in the p-type GaAs/AlGaAs samples, the ground state of FQHE

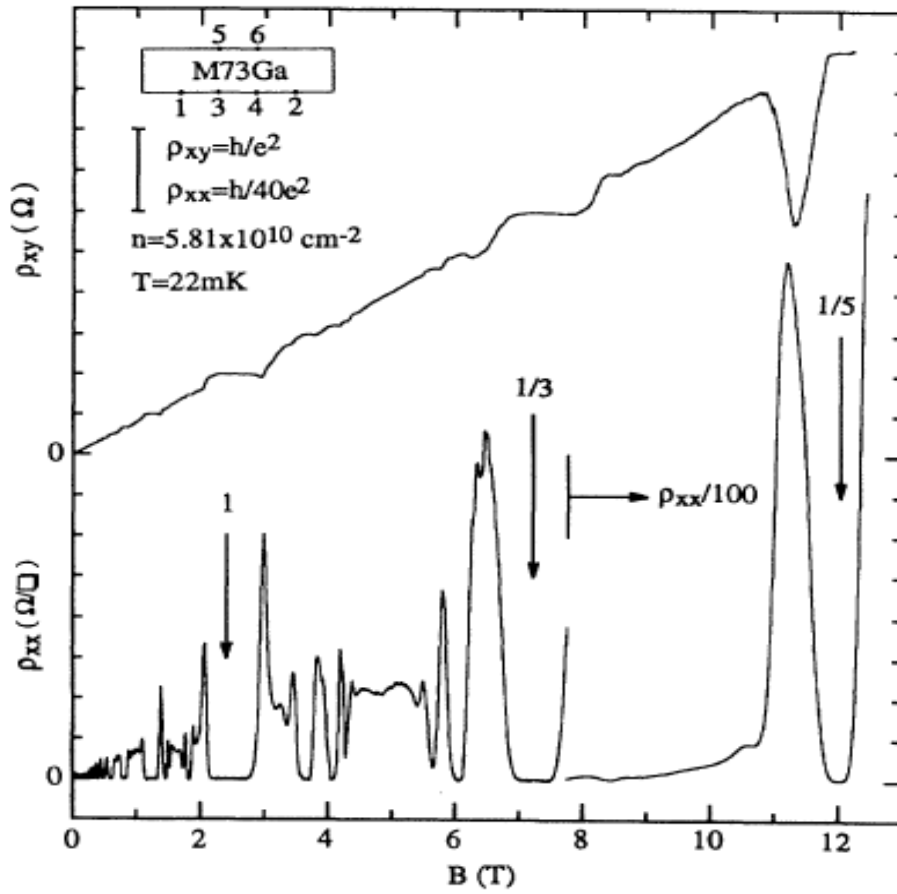


Figure 5.1 : The magnetotransport data of a low electron density sample, there exists a reentrant insulating phase around $\nu = 1/5$ FQHE state (Sajoto et al [43]).

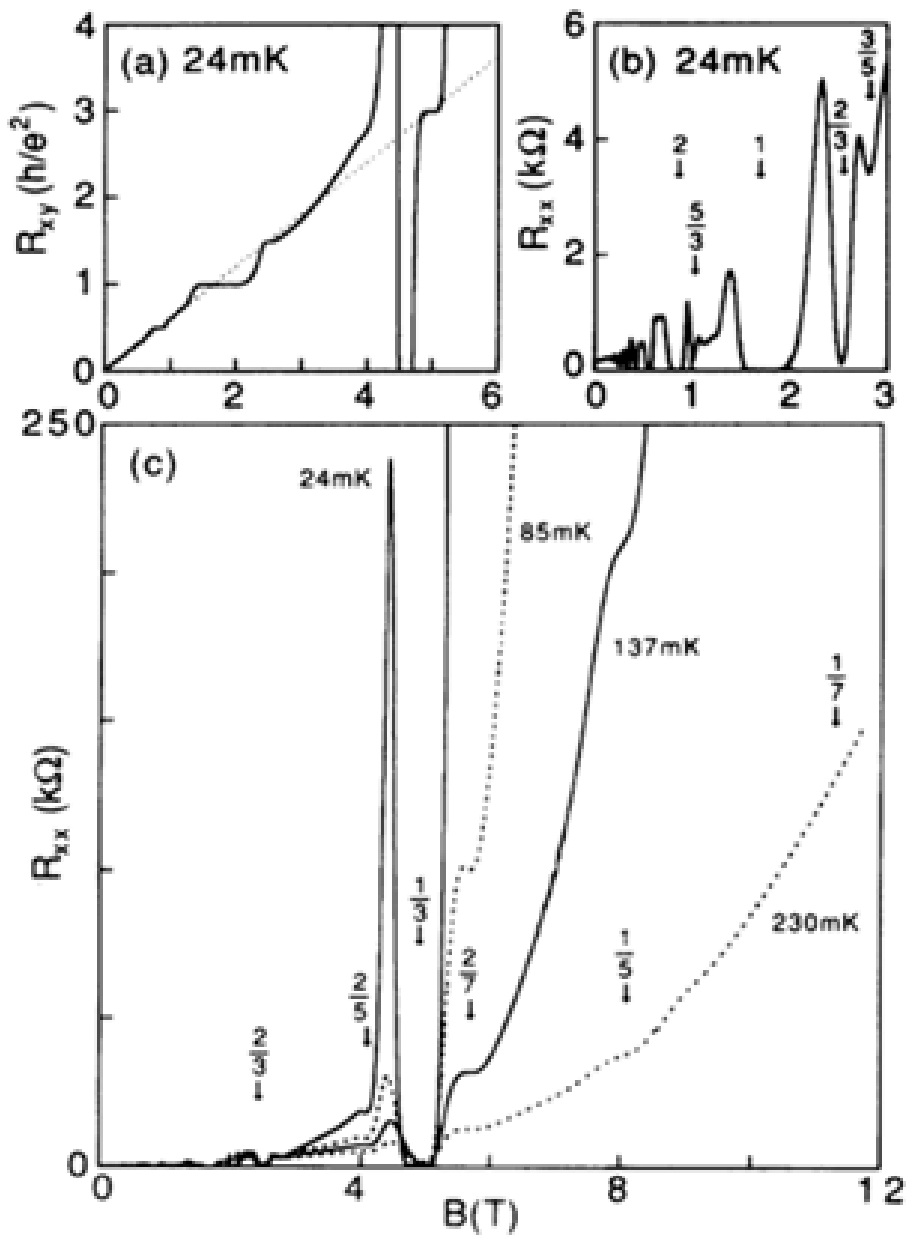


Figure 5.2 : The magnetotransport data of a dilute 2DHS, with a reentrant insulating phase along $\nu = 1/3$ FHQE state (Santos et al [42]).

and Wigner Crystal states are influenced by LLM. In 2DHS, the vanishing position on B -axis of insulating phase (IP) in the vicinity of $\nu = 1/3$ shift to lower filling factor ν for a smaller LLM parameter κ , which corresponds to a higher hole density p in GaAs [42, 69, 70]. Therefore, it is rather surprising that our observation in a high density ($p \sim 2.0 \times 10^{11} \text{ cm}^{-2}$) 2DHS displays a reentrant insulating phase around $\nu = 1/5$ FQHE liquid.

5.3 Fractional Quantum Hall Liquid and Wigner Solid

In this section, we would like to discuss the competition between the ground states of Fractional quantum Hall liquid and Wigner solid, which can be influenced by various factors. As I mentioned in Chapter 2, the magnetic length can be expressed as: $l_B \sim B^{-1/2} \sim \nu^{1/2}$; at a low magnetic field, the electron can not be localized, and has an electron state of liquid phase. At a high magnetic field B , the existence of the solid phase is possible when the average distance between electrons is smaller than magnetic length [71–73]. Wigner Solids locate at very high magnetic fields, meaning that the ground state energy of insulating phase decreases with increasing B . Normally, for a non-extremely-high B , the FQHE liquid phase has a lower ground state than other phases. Therefore, a competition exists between the ground states of Winger Crystal solid phase and FQHE liquid phase for the high B . In the real systems, FQH liquid was observed at $\nu = 1/3$ in 2DHS, and at $\nu = 1/5$ in 2DES, around which the Wigner solid has a lower ground state energy.

Actually, other factors can also influence the ground states, i.e. Landau level mixing, etc. Yoshioka theoretically discussed and demonstrated the Landau level mixing (LLM) effect on the ground state [74] and energy gap [75] in 2DES. In the experiments, Santos et al [42] (Figure 5.2) observed the reentrant insulating phase

around $\nu = 1/3$ FQHE state in 2DHS. The LLM parameter at $\nu = 1/3$ state (with a $B \sim 5$ T) is $\kappa \sim 5$. On the other hand, Yoshioka estimated a critical value of LLM parameter at $\kappa \sim 6.2$ [74]. In simple terms, the Landau level mixing favors the Wigner solid phase and weakens the FQH liquid.

Based on previous experiments, it is necessary to summarize the performances of FQH liquids and Wigner solids. In the measurements of conductances and resistances, quantum phases exhibited distinct behaviors. (1) As we introduced in Chapter 2, the longitudinal resistance approaches to zero as T decreases, while the Hall resistivity is quantized at LL filling factor ν . (2) The Wigner solids exhibit an insulating phase in R_{xx} , with a Hall resistivity irregular. (3) Either FQHE liquid or Wigner solid state has a conductance of ~ 0 , as T goes to zero. At a low T , the competition between the phases causes the increase of conductance.

5.4 Two-Dimensional Hole System in GaAs

The valence band structure in GaAs is more complicated than conduction band. The top of valence band (Γ -point) in GaAs is four-branched. The wave functions of the top branch are of p-orbital symmetry. The high anisotropy of wave functions in the top valence band induces a strong overlap in the z -direction and a much weaker overlap in the x - y plane. In the x - y plane of the sample, electrons travel less freely, accompanied by a larger effective mass. All three p -orbitals form a band with a double degenerated heavy band and a single light band. The relation of energy vs. k -vector (wave number) (Figure 5.3) exhibits that, heavy holes and light hole co-exists for a small k -vector. In the GaAs/AlGaAs QW (or heterostructure) samples, the ground state energies of light and heavy holes are different, due to different effective mass which leads to the separation between valence bands (Figure 5.3 panel b)). The

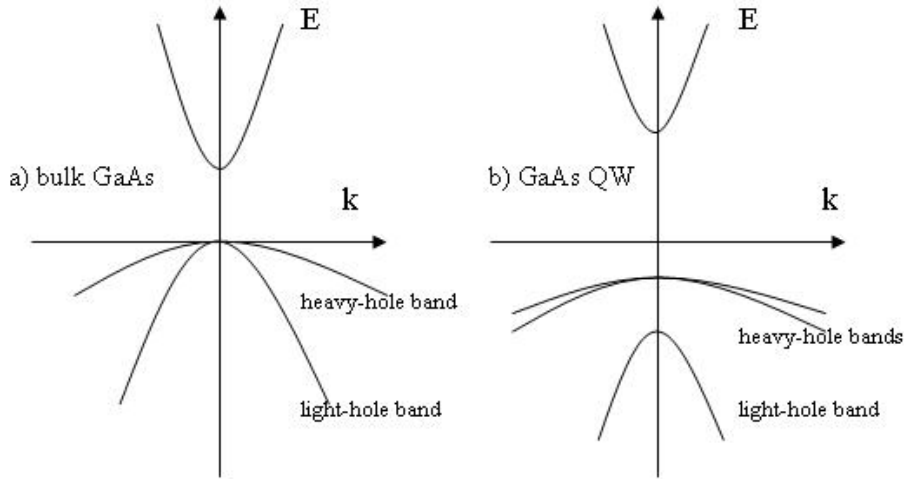


Figure 5.3 : The band structure diagram in bulk GaAs, (panel a)), and in GaAs quantum well (panel b)).

Rashba effect (from inversion asymmetry of quantum well) causes a spin-splitting in heavy bands ($k > 0$) at zero magnetic fields (Figure 5.3 panel b)).

As discussed above, comparing to 2DES, a two dimensional hole system has a distinct valence band structure. The typical type of the GaAs band structure is exhibited in Figure 5.3. The effective masses of holes in bulk GaAs are more complicated than that of electron: $m_H^* = 0.5m_e$, and $m_L^* = 0.08m_e$, where m_H and m_L are heavy hole and light hole effective mass, respectively. Effective mass of the 2D hole system can be measured with microwave (MW) cyclotron resonance (CR). Microwave cyclotron resonance exists when $\omega_{MW} = \omega_C$, $\omega_C \sim 1/m_H^*$. Pan et al [76] developed a method for measuring band edge effective mass (m_b) at various density (p) in 2DHS. More recently, Yuan et al [77] described the experimental setup for effective mass measurements: the $1\text{ mm} \times 1\text{ mm}$ square GaAs wafer without any contacts is glued on one end of a long sapphire substrate bar, and a chip Cernox thermometer is located on the other end of the substrate. Yuan et al [77,78] reported that our p-type GaAs

sample has a heavy effective mass $m^* \sim 0.4m_e$.

Chapter 6

Experiments on Wigner Crystal in a Two-Dimensional Hole System

6.1 Experimental Setup

The magnetoresistance (or magnetoconductance) experiments were performed in a dilution refrigerator, with a base temperature $T \sim 20$ mK. The samples were studied in a $B \sim 45$ Tesla hybrid magnet, which consists of the superconducting magnet ($B \sim 11.5$ T) and a resistive magnet (~ 33.5 T). The magnet is rather water consuming (~ 4000 gallons/min) and power consuming (33 MW). The bore radius is merely 32 mm (~ 1.25 ") for the sample holder: two samples (face to face) can be tested simultaneously in each loading, with one sample facing up and the other facing down.

Next we introduce the general procedure for lithography. The sample preparation includes three steps: exposure, developing, and metal deposition with E-beam evaporator. First, we would like to expose the sample (with a layer of photoresist on the top) by means of the mask which we produced. The mask can be patterned by running laser in Heidelberg DWL 66 mask maker, which is widely used in nanoscale lithography. Our mask maker is equipped with a 405 nm (wavelength) laser and two exchangeable writeheads. Our mask was written with a 4 mm writehead, which has a focal depth of ~ 1.8 μ m and a minimum resolution size ~ 800 nm. We designed the Corbino sample patterns with various sizes: OD/ID = 2.5 mm/1.25 mm, 3 mm/2.5 mm, 3.5 mm/ 2 mm, and 4 mm / 2 mm by AutoCAD. Then the files were converted

into “.lic” files that are output into the DWL 66 system. The conversion software works in Linux computer system; and the laser writing procedure runs on OS-9 system. It is advantageous to use the low reflective Cr-plate, which has nanofilm coated with 530 nm thick AZ 1518 photoresist. After the writing procedure, the mask needs to be developed in the MF-351 developer for ~ 30 -60 seconds, and rinsed in DI water. If the pattern is fully developed, the mask would be etched in CEP-200 etchant for $\sim 1 - 2$ minutes, and then rinsed in DI water. Finally, the photoresist on the mask is removed by placing it in stripper-100 for 4 - 5 minutes, followed by cleaning in DI water again.

We measured the magnetoconductance with the divider circuits (Figure 6.1 panel a)). The applied ac voltage is generated from an SR 830 lock-in amplifier with a frequency of 7 Hz (also 13 Hz or 17 Hz). The measured current (I_x) of the sample can be obtained from the voltage signals (channel: A-B) passed through a standard resistor of $1\text{k}\ \Omega$ (or $10\ \text{k}\Omega$). The minimum value of the ac voltage from the lock-in amplifier is 4 mV, which is large enough to drive the solid to slide. We obtained a much lower ac voltage from the divider circuit (by a ratio between resistors of $\sim 1\ \text{k}\Omega/100\ \text{k}\Omega$), which is necessary for observing the transition from static solid into sliding solid. The non-linear behavior of the conductance requires ac signals by means of dc components (Figure 6.1 panel b)). We perform the non-linear conductance measurements by establishing a dc electric field (E_{dc}) which is generated by a Keithley-6221A dc current source (with a range of $0 \sim 30\ \mu\text{A}$). The dc signals go through a resistor of $1\ \text{M}\Omega$, which is part of another divider circuit in the ac+dc measurements. The $1\text{k}\ \Omega$ resistor is used for dividing both ac and dc components. We obtained the threshold of the field either by sweeping the dc current for a fixed magnetic field or by sweeping B at fixed dc signals. The T -dependent conductance measurements play an important

role in our experiments. Temperature of the coolant is controlled by a Lakeshore temperature controller 370. The applied power is roughly proportional to the square root of the steady coolant temperature when the temperature is stabilized after some minutes.

6.2 Sample Characterization

Previous experiments measured the p-type (001) oriented GaAs/AlGaAs samples, in which beryllium (Be) is utilized as the acceptor [79]. In this wafer, the hole mobility is around $\mu \sim 10^5$ cm²/Vs. Higher mobility ($\mu \sim 1 \times 10^6$ cm²/Vs) 2DHS in (311)A orientation wafer has been developed shortly afterwards. Si dopants incorporate the arsenic atoms (As) [80], having the function of acceptors. On the other hand, the (311)A orientation induces more complicated band structures than those of (001) orientation. Recently, Manfra et al [81] developed and reported a new growing technique of C-doped (001) GaAs/AlGaAs wafers, which has a typical mobility $\sim 1 \times 10^6$ cm²/Vs.

Experimentally, we have explored two (001) C-doped 20 nm wide GaAs QW wafers by making measurements in high magnetic fields: one is GaAs/Al_{0.24}Ga_{0.76}As QW (wafer A), with a hole density of 1.9×10^{11} cm⁻² and mobility $\sim \mu = 1 \times 10^6$ cm²/Vs; the other is GaAs/Al_{0.325}Ga_{0.675}As QW (wafer B) with a hole density of $\sim (2.2 - 2.35) \times 10^{11}$ cm⁻², and a mobility $\mu = (1.3 - 1.5) \times 10^6$ cm²/Vs.

The samples were measured in both Van der Pauw and Corbino configurations. Van der Pauw configuration (as we mentioned in Chapter 3) is used for magnetoresistance measurements, and a Corbino sample can be used for direct measurement of magnetoconductance. In the conductance measurements, the Corbino current is proportional to the longitudinal conductance in the presence of an applied excitation

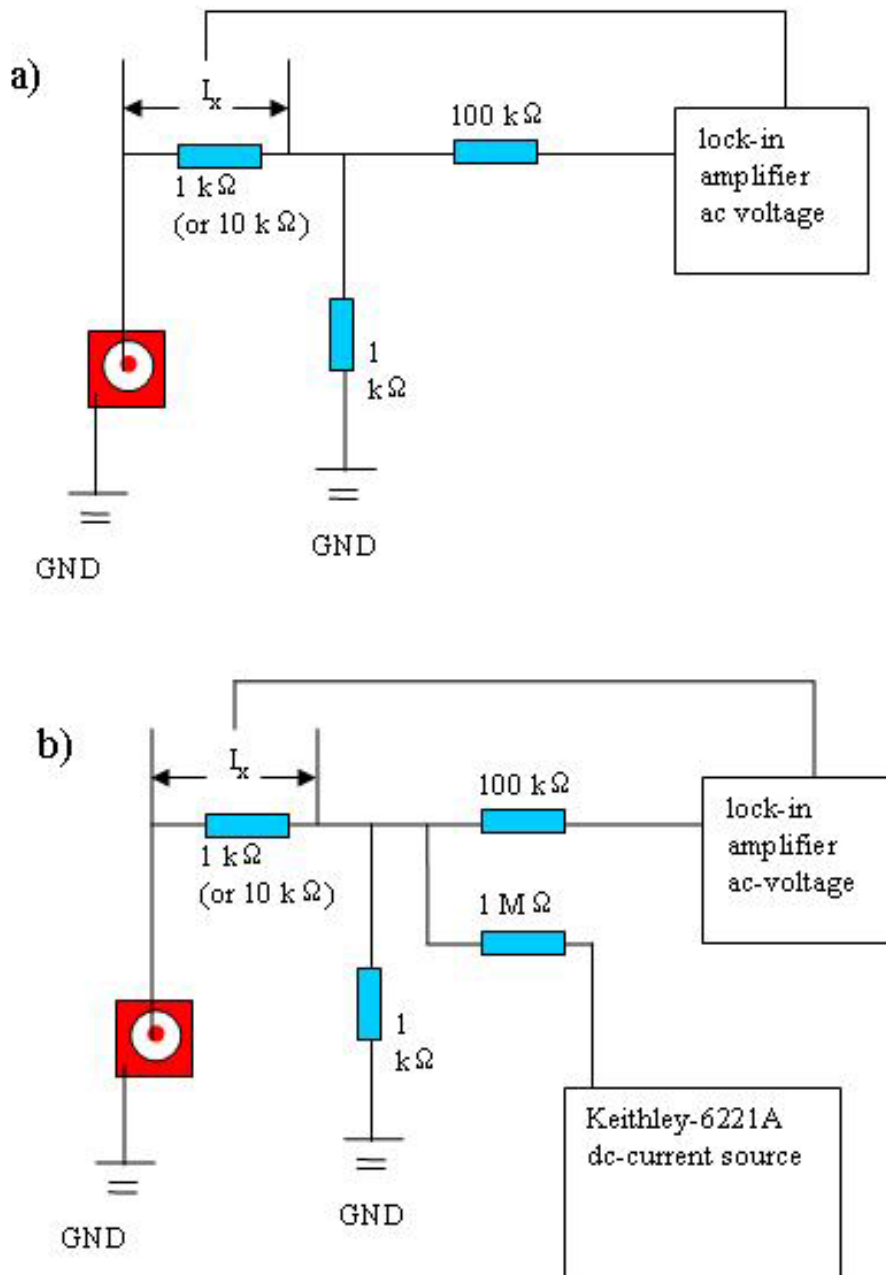


Figure 6.1 : Schematic for setup of conductance (panel a)) and nonlinear (ac + dc) conductance (panel b)) measurements on Corbino samples.

voltage. The Figure 6.3 shows the Corbino configuration, which consists of concentric circle contacts. At the base temperature, the resistance between the ohmic contacts is smaller than 50 Ohms.

The Ohmic metal contacts for the 2DHS in GaAs can be created by employing several types of alloys using the E-beam evaporator. In our experiments, 500 Å Au/Be ($\sim 2\%$ Be) alloy was evaporated with a depositing rate around (0.5 - 1) Å/s, and followed by 2000 Å Au with a deposition rate around (1 - 2) Å/s. In the liftoff procedure, the sample is put into a plastic dish, and sonicated in Acetone for 1 \sim 3 minutes until the whole pattern is revealed. Then the sample is rinsed in the Methanol for 2 minutes, and cleaned again in DI-water. Finally, we annealed our samples at the temperature ~ 420 °C for ~ 3 minutes which is required to develop good ohmic contacts. In addition, we also produced In/Zn (1:1) contacts with JBC AD-2950 soldering station at ~ 350 °C. After soldering, the contacts also need to be annealed at a temperature around ~ 450 °C for $\sim 15 - 20$ minutes, within the protection of forming gas ambient (15% H₂, 85% N₂).

It is well known that Corbino samples are widely used in conductance measurements. Previous experiments have reported the Wigner solid phase in magnetoresistance, in which the obtained electric fields are mixture of longitudinal and Hall components. We would like to directly measure the conductance of the 2DHS sample. The conductance measurement experiments can be conducted by applying the dc electric field (E_{dc}), which eliminate the E_{xy} component. For the simplest model, the voltage is along the radial direction.

Under a magnetic field, the resistance can be measured in a Hall bar or a Van der Pauw sample, while the conductance can be measured in a Corbino sample. Here, we should mention the relation between the conductivity and resistivity. The

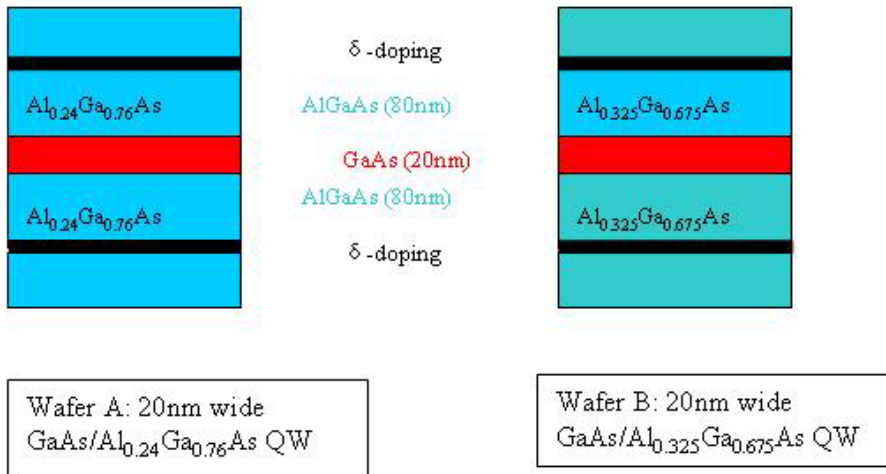


Figure 6.2 : The schematic of the main structure of the 20 nm wide GaAs/AlGaAs wafers: A and B, other details of layers are not present in this figure.

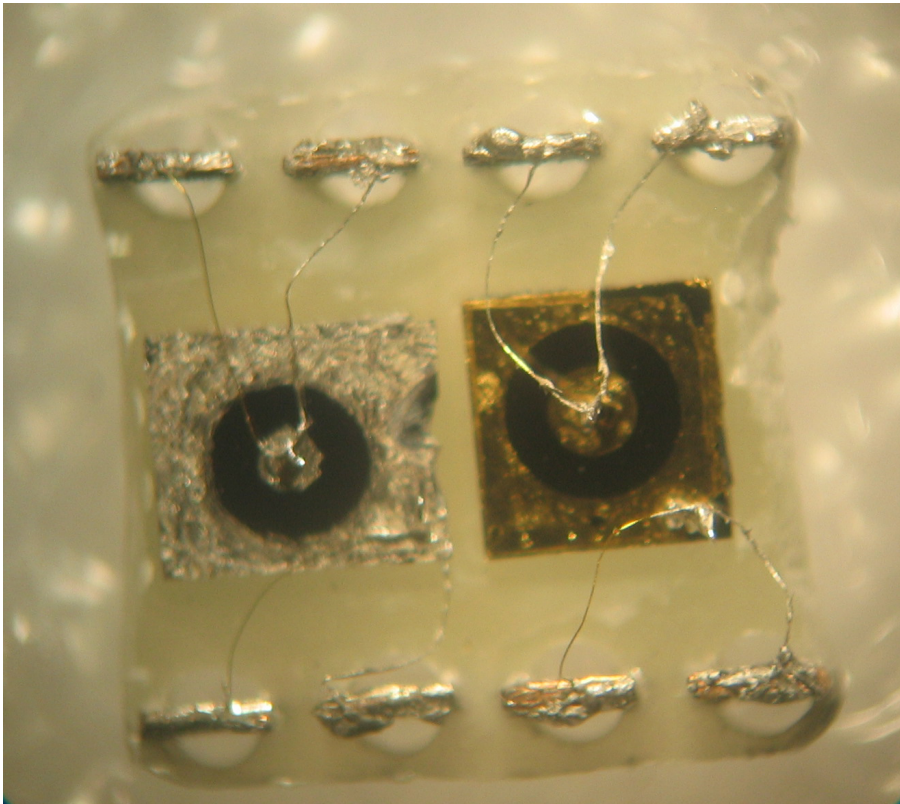


Figure 6.3 : Optical picture of typical Corbino samples, the sample B3 (h-QW-B-3) (left) has In/Zn contacts and the sample A2 (h-QW-A-2) (right) has Au/Be contacts.

conductivity tensor for 2 dimensional system can be expressed as:

$$\vec{\sigma} = \begin{pmatrix} \sigma_{rr} & \sigma_{r\phi} \\ -\sigma_{r\phi} & \sigma_{\phi\phi} \end{pmatrix} \quad (6.1)$$

The resistance tensor is the reciprocal tensor of the conductivity:

$$\rho = \frac{1}{\sigma_{rr}^2 + \sigma_{r\phi}^2} \begin{pmatrix} \sigma_{rr} & \sigma_{r\phi} \\ -\sigma_{r\phi} & \sigma_{\phi\phi} \end{pmatrix} \quad (6.2)$$

For the case of absence of magnetic field, $\rho_{rr} = 1/\sigma_{rr}$. However, under a magnetic field, with a condition $|\sigma_{rr}| \ll |\sigma_{r\phi}|$; in this limit, we obtained:

$$\rho \approx \begin{pmatrix} \sigma_{rr}/\sigma_{r\phi}^2 & -1/\sigma_{r\phi} \\ 1/\sigma_{r\phi} & \sigma_{rr}/\sigma_{r\phi}^2 \end{pmatrix} \quad (6.3)$$

where, the longitudinal resistivity is proportional to the longitudinal conductivity:

$$\rho_{rr} \approx \sigma_{rr}/\sigma_{r\phi}^2 \quad (6.4)$$

From scalar form of Maxwell equations, the current density and electric field are related by the relation:

$$J = \sigma E \quad (6.5)$$

which is for the case of absence of a magnetic field. Under a magnetic field, this relation can be expressed as: $\vec{J} = \vec{\sigma} \vec{E}$, in which the conductivity is in tensor form.

$$\begin{pmatrix} J_r \\ J_\phi \end{pmatrix} = \begin{pmatrix} \sigma_{rr} & \sigma_{r\phi} \\ -\sigma_{r\phi} & \sigma_{\phi\phi} \end{pmatrix} \begin{pmatrix} E_r \\ E_\phi \end{pmatrix} \quad (6.6)$$

In the measurement of magnetoconductance, $J_\phi = 0$, the tensor equations can be expressed as:

$$\begin{pmatrix} J_r \\ 0 \end{pmatrix} = \begin{pmatrix} \sigma_{rr} & \sigma_{r\phi} \\ -\sigma_{r\phi} & \sigma_{\phi\phi} \end{pmatrix} \begin{pmatrix} E_r \\ E_\phi \end{pmatrix} \quad \text{which lead to}$$

$$J_r = \sigma_{rr}E_r + \sigma_{r\phi}E_\phi \quad (6.7)$$

$$-\sigma_{r\phi}E_r + \sigma_{\phi\phi}E_\phi = 0 \quad (6.8)$$

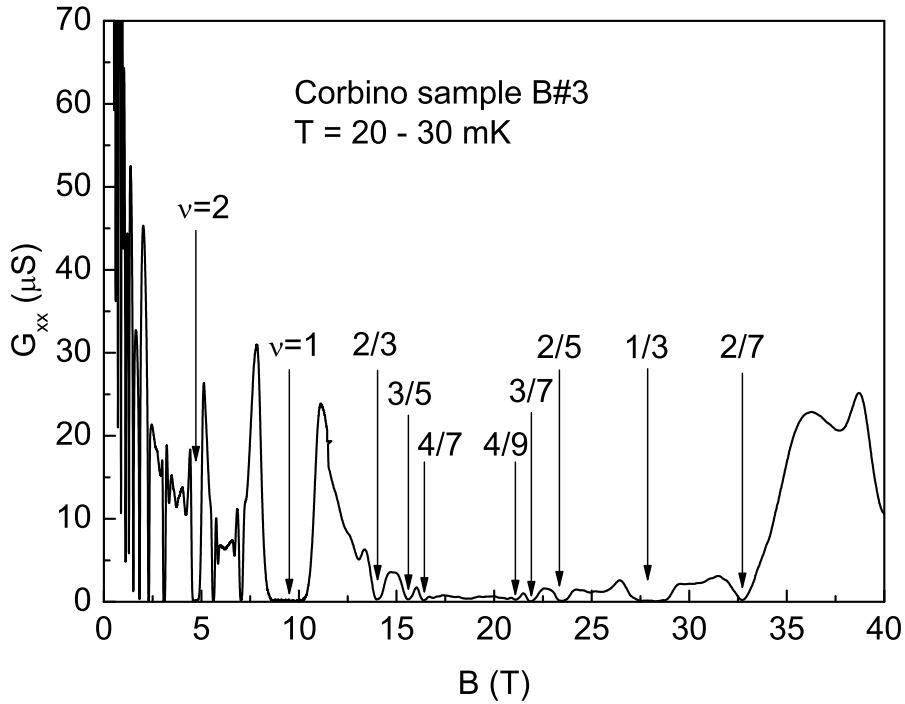


Figure 6.4 : Conductance data of 20nm QW B3 (Corbino sample h-QW-B-3) in the magnetic field from 0 to 40 T.

For the simplest case, we assume: $E_\phi = 0$, which leads to $J_r = \sigma_{rr}E_r$. In this method, we can obtain only the longitudinal component of the conductance.

Now we would like to analyze the relation between the conductance and conductivity. Considering the simplest model of electric field distribution in a 2D Corbino sample, the electric field (E) and current density (J) is along the radial direction. From Maxwell equations, we have:

$$J_x = \sigma_{xx}E_x \quad (6.9)$$

Here current density is:

$$J = I/2\pi r \quad (6.10)$$

and σ_{xx} is the magnetoconductivity. The voltage can be obtain by the integral form

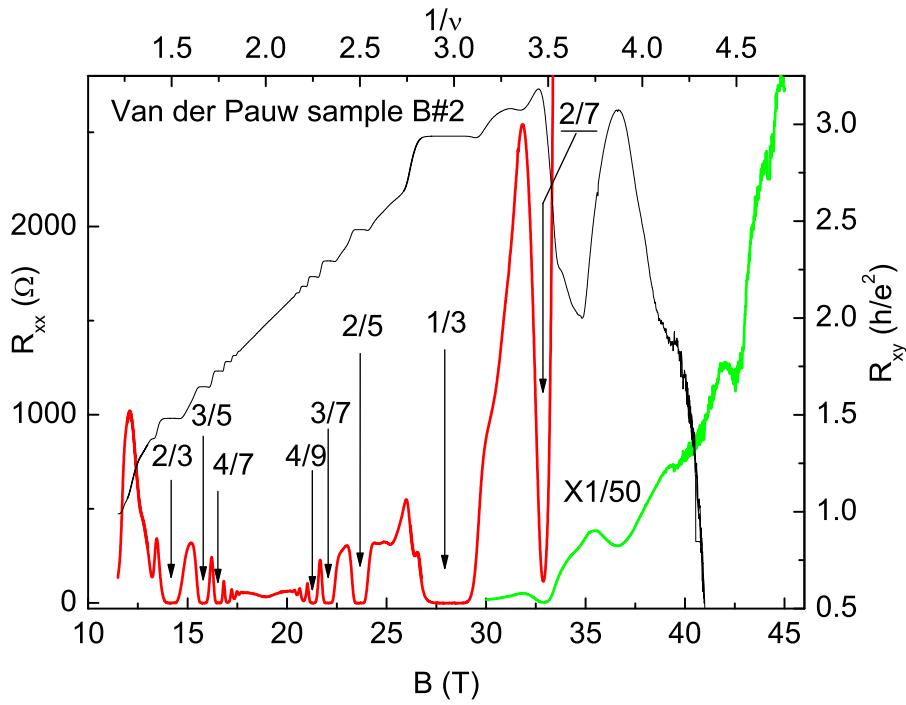


Figure 6.5 : Magnetoresistance R_{xx} (red and green) and R_{xy} of 20 nm wide QW B2 (Van der Pauw sample h-QW-B-2) at a base $T \sim 20$ mK.

of the Maxwell equations:

$$V_x = \int -E_x dr = I_x \ln(r_1/r_2)/2\pi\sigma_{xx} \quad (6.11)$$

where, r_1 and r_2 are inner and outer radius, respectively. On the other hand, from the differential form:

$$E_x = -dV/dI = I_x/2\pi\sigma_{xx} \sim 1/r \quad (6.12)$$

The ratio between E_x and V_x :

$$E_x/V_x = (1/r)\ln(r_2/r_1) \quad (6.13)$$

The longitudinal conductance G_{xx} :

$$G_{xx} = I_x/V_x = \sigma_{xx}2\pi/\ln(r_2/r_1) \quad (6.14)$$

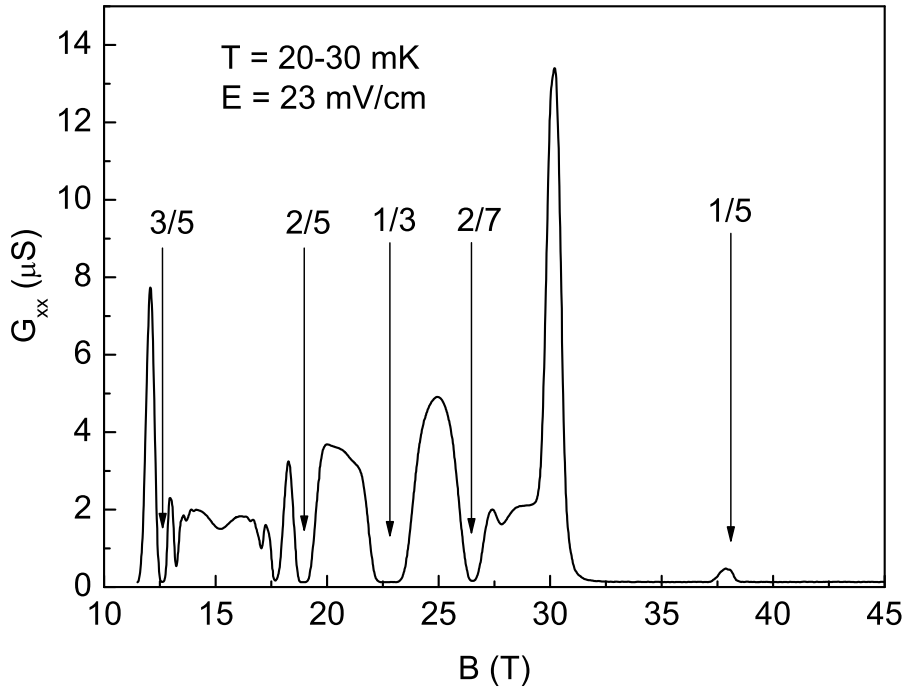


Figure 6.6 : Conductance data of 20nm QW A2 (Corbino sample h-QW-A-2) in the magnetic field from 19 to 45 T.

For our measured Corbino sample A: $r_2/r_1 = 2$, geometrical factor (between conductance and conductivity) $G_{xx}/\sigma_{xx} = 2\pi/\ln(r_2/r_1) = 9$, and $V_x = E_x/r\ln 2$.

The magnetoconductance of the Corbino sample B3 (h-QW-B-3) is measured at low temperature around 20 - 30 mK. From the measured data, we can discern that the conductance for zero magnetic field is much higher than that in the magnetic field ($B > 0$). At the LL filling factors $\nu = 1/3, 2/7$, etc, the data exhibits zero conductance for the magnetic field ($B \sim 28 \text{ T}, 33 \text{ T}$,). For the magnetic field $B \sim 37-38 \text{ T}$, $\nu \sim 1/4$, the conductance exhibits a dip for the temperature $T \sim 30 \text{ mK}$.

Figure 6.5 exhibits the magnetoresistance of Van der Pauw sample (h-QW-B-2) at a base T of 20 mK with a range of B from: 12 T \sim 45 T. In the range of 12 T \sim 29 T, we observed FQHE states at various LL filling factors: i.e. $2/3, 2/5, 1/3$,

etc. For higher magnetic fields ($B > 29$ T), the resistance increase sharply from several thousands Ohms to more than 100,000 Ohms, which is an insulating phase. In contrast to the increasing resistance as magnetic fields, the data at the vicinity of filling factor $\nu = 2/7$ exhibit a sharp decreasing behavior, which is the reentrant insulating phase around $2/7$ FQHE state. The accompanied Hall resistivity exhibits a distinct decrease for B from ~ 33 T ($\sim \nu = 2/7$) to 35 T. Generally speaking, for the filling factor $\nu < 2/7$, the Hall resistivity is off from the quantized conductivity. At $T \sim 20$ mK, the state $\nu \sim 1/4$ exhibits a dip in an insulating phase, with a large $R_{xx} \sim 20$ k Ω . The accompanied R_{xy} is irregular for insulating phase, but it dramatically approaches quantized Hall resistivity value in the vicinity of $1/4$ state. Comparing with Figure 6.4 at $T \sim 20$ mK, the longitudinal and Hall resistivity near the $1/4$ state at $T \sim 30$ mK exhibit a competition between Wigner solid phase and FQH liquid phase (Figure 6.5).

The magnetoconductance measurements of Corbino sample A2 (h-QW-A-2) is performed by applying a electric field of ~ 23 mV/cm. Figure 6.6 shows the data for high magnetic fields 19 T $< B < 45$ T. The conductance exhibits a hump at $\nu \sim 1/5$, where the Wigner lattice order is weaker. The possible interpretation is that the FQH liquid mixed with lattice order; and the details will be described afterwards.

6.3 Conductance and Resistance Measurements

We measured the magnetoconductance of Corbino sample A2 in various ac electric fields, with the range from $\sim (4.6 - 690)$ mV/cm. The electric field is applied with a SR830 lock-in amplifier, which outputs an ac-voltage in the circuit. The data (in Figure 6.7, 6.8, 6.9, and 6.10) indicate the weakened solid phase and the sliding motion around the state of $\nu = 1/5$ ($B \sim 38$ T). In the next section, differential conductivity

provides the evidence of sliding WS. For a weak applied field ($E_{ac} \sim 4.6$ mV/cm), the conductance is \sim zero, which is interpreted as the localization of electrons at the sites of Wigner lattice. As the ac-field increases, the Wigner lattice starts sliding, with the measured conductance increasing sharply. Under a dc-field of around 276 mV/cm, the maximum of conductance at $\nu = 1/5$ is $\sim 12.5 \mu\text{S}$. Increasing dc-field continuously, the conductance start to decrease distinctly (Figure 6.10), this is thought to result from the heating of current. For the conductance measurements of Corbino sample A2 (h-QW-A-2) under higher electric fields (Figure 6.9, and 6.10), we observed the phase transition from the $\nu = 2/9$ FQHE liquid state into the reentrant insulating phase around $\nu = 1/5$, which is consistent with the result from Du et al [68]. For an electric field range from 276 mV/cm to 690 mV/cm, an inflexion exist around $B \sim 33.5$ T ($\nu = 2/9$): (1) under a high electric field (~ 276 mV/cm), the conductance ~ 36 T reaches a maximum, with the $\nu = 2/9$ state being most obvious. (2) As electric field increases (> 440 mV/cm), the features of the $2/9$ state become a little weaker.

Experimental results in Figure 6.12 exhibit the T -dependent conductance by changing the heater power in the Lakeshore temperature controller 370 system, with a temperature range from 20 mK to ~ 364 mK. We observed FQHE states around the composite fermions, i.e. $\nu = 4/9, 2/5, 1/3,$ and $2/7,$ etc. At the lowest $T \sim 20$ mK, the conductance in the vicinity of $\nu = 1/5$ is close to zero. As temperature increases, the conductance keeps increasing for a temperature range: 20 mK \sim 170 mK. In the T -range from base T to 100 mK, the traces around the $1/5$ state exhibit peaks of various heights. However, the trace at $T \sim 170$ mK shows a deep minimum, around which two strong nearby peaks exist. The trace of $\nu = 1/5$ state at 170 mK indicates a FQHE liquid phase. Combining the traces at $T < 170$ mK, a competition between the Wigner solid phase and FQHE liquid exists in the conductance of this

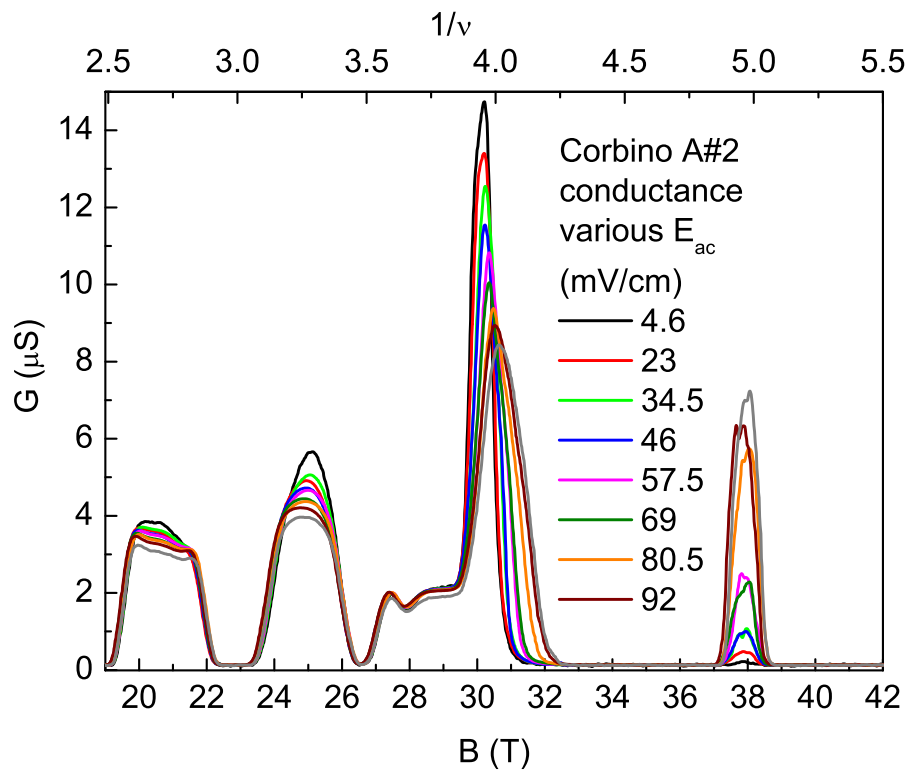


Figure 6.7 : Conductance of sample A2 under ac electric fields, which ranges from 4.6 mV/cm to 92 mV/cm.

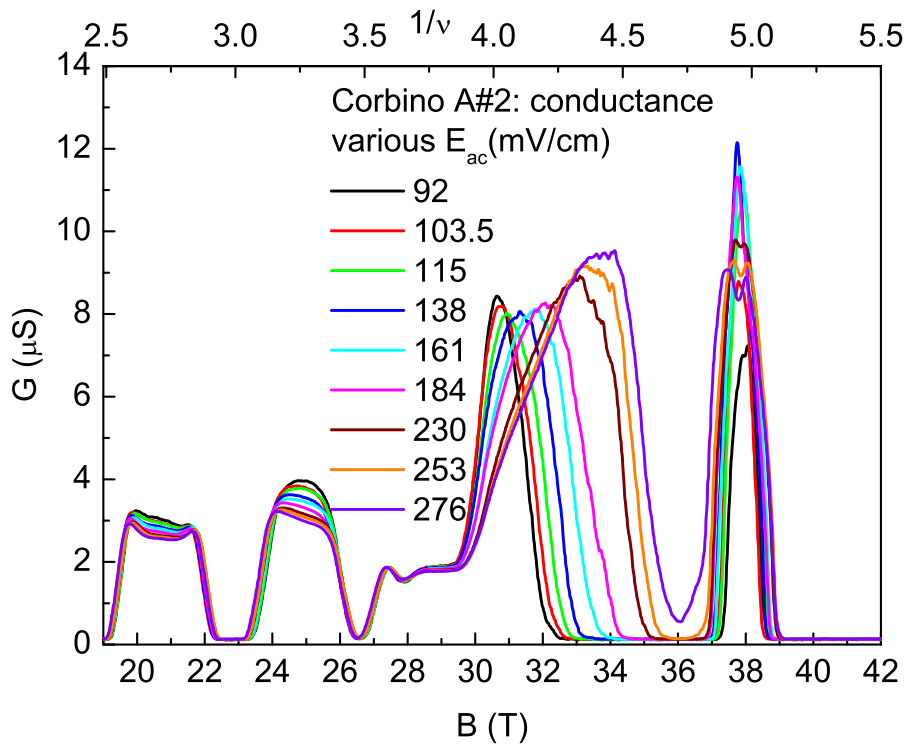


Figure 6.8 : Conductance of sample A2 under ac electric fields, which ranges from 92 mV/cm to 276 mV/cm.

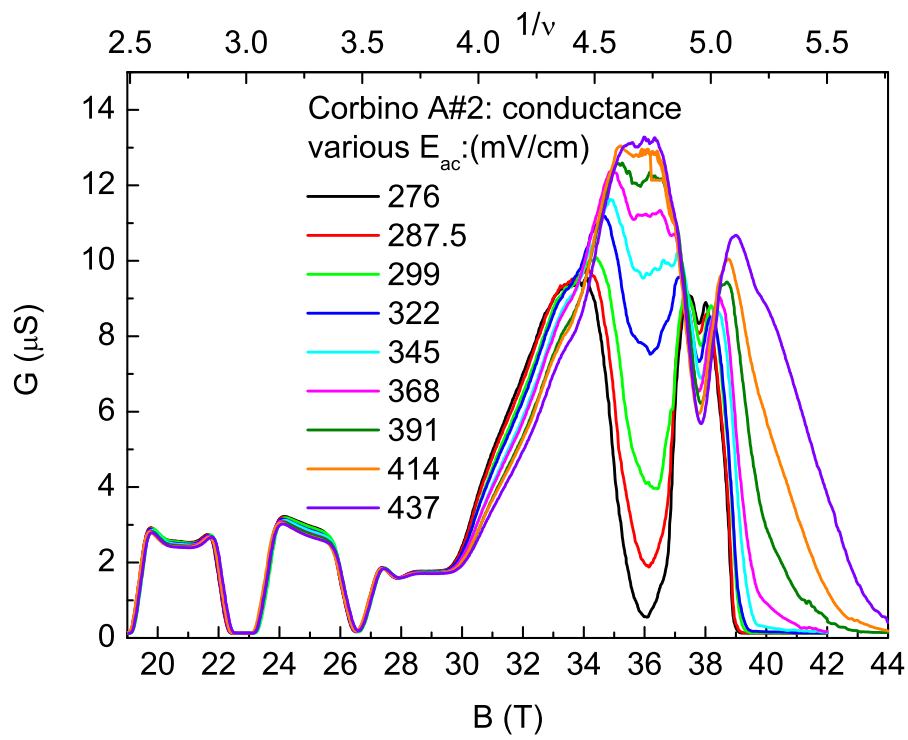


Figure 6.9 : Conductance of sample A2 under ac electric fields, which ranges from 276 mV/cm to 437 mV/cm.

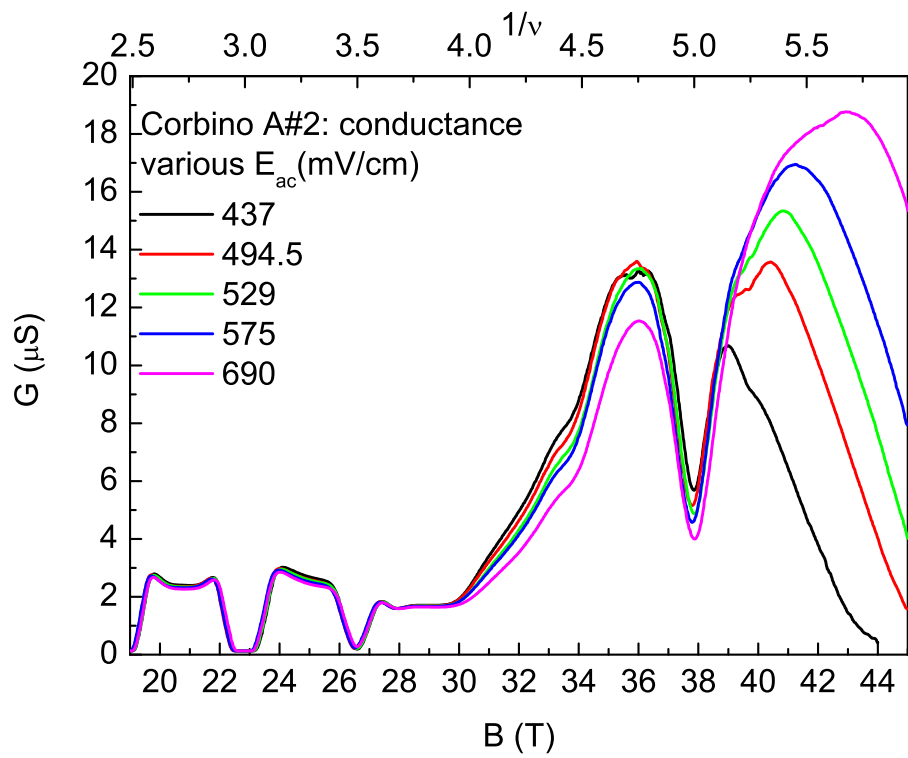


Figure 6.10 : Conductance of sample A2 under ac electric fields, which ranges from 437 mV/cm to 690 mV/cm.

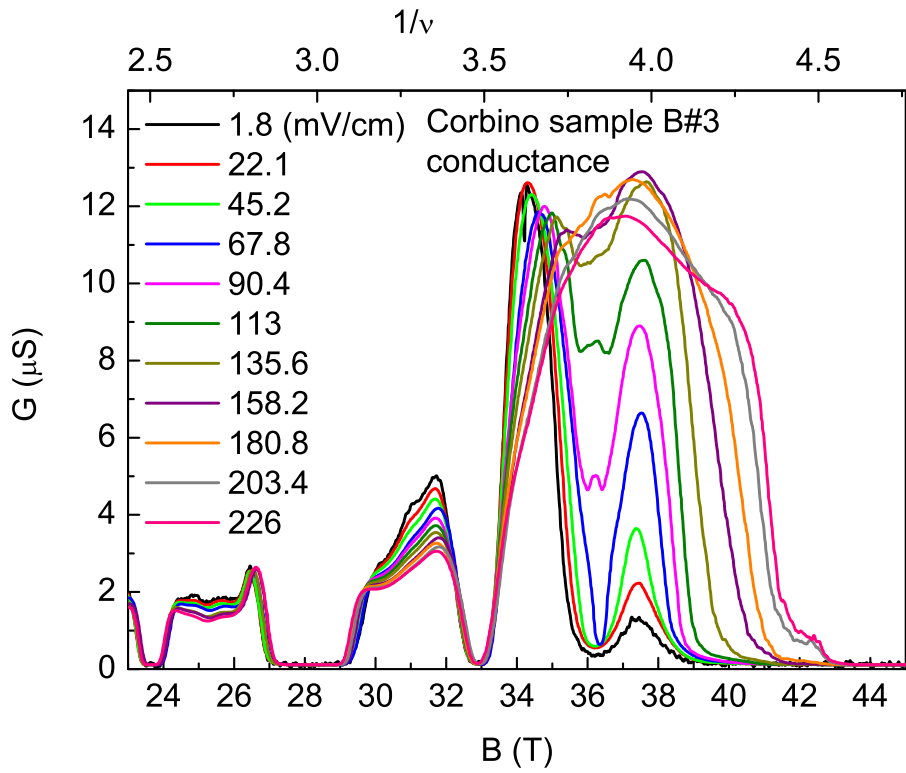


Figure 6.11 : Conductance sample B3 (h-QW-B-3) under ac electric fields, which ranges from 1.8 mV/cm to 226 mV/cm.

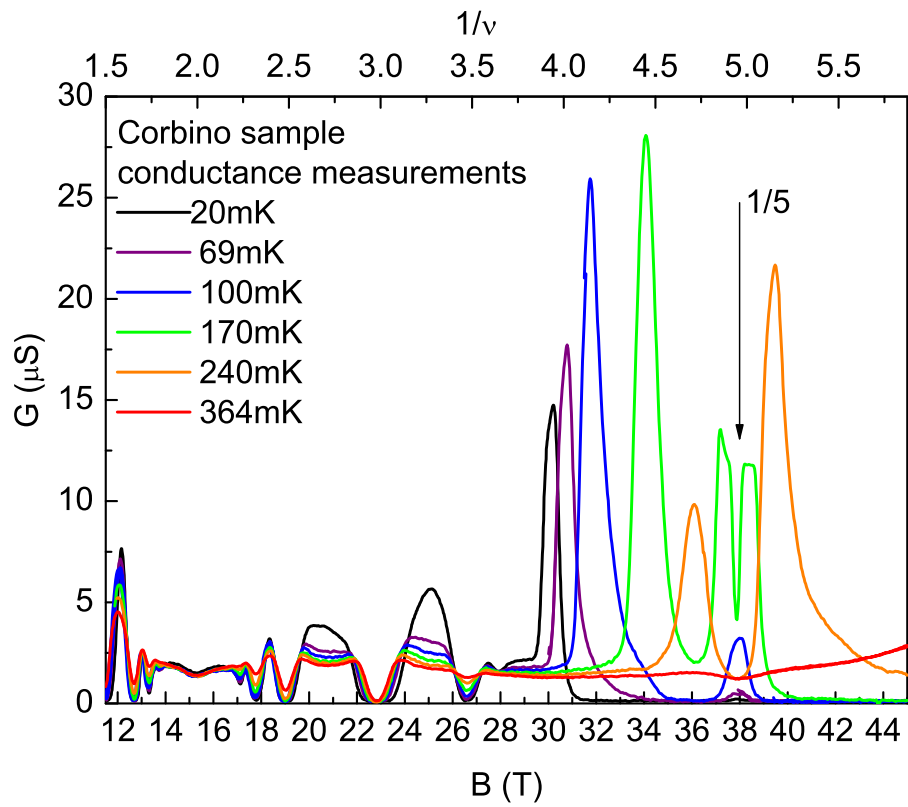


Figure 6.12 : T -dependent conductance of Corbino sample A2 (h-QW-A-2) . The applied field $E_{ac} = 46$ mV/cm.

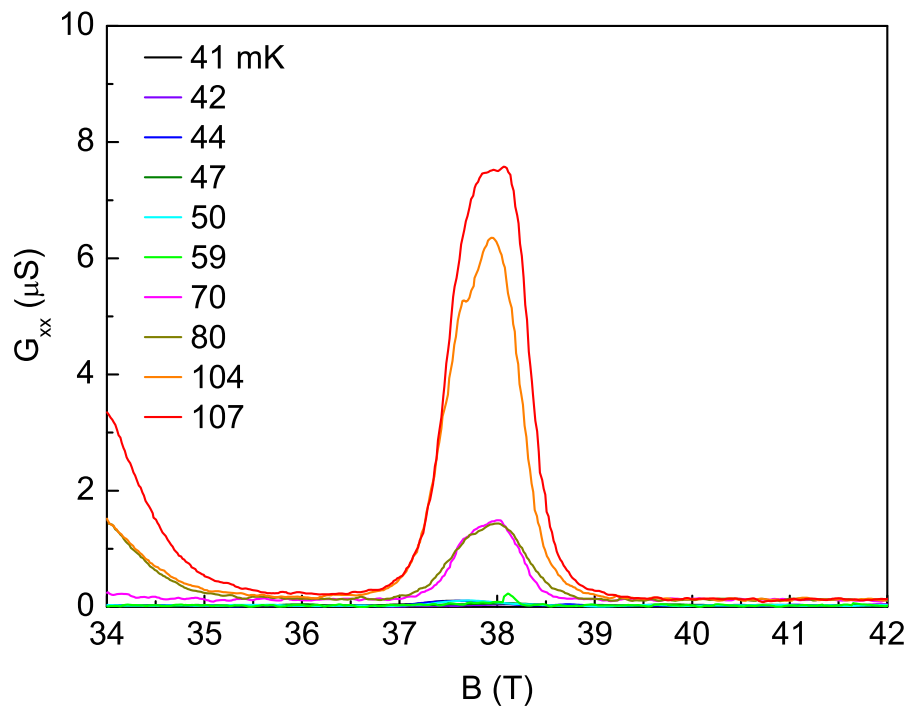


Figure 6.13 : T -dependent conductance of sample A2 (h-QW-A-2) (for $T = 41 - 107$ mK) is measured in a magnetic range: $B \sim 34 - 42$ T.

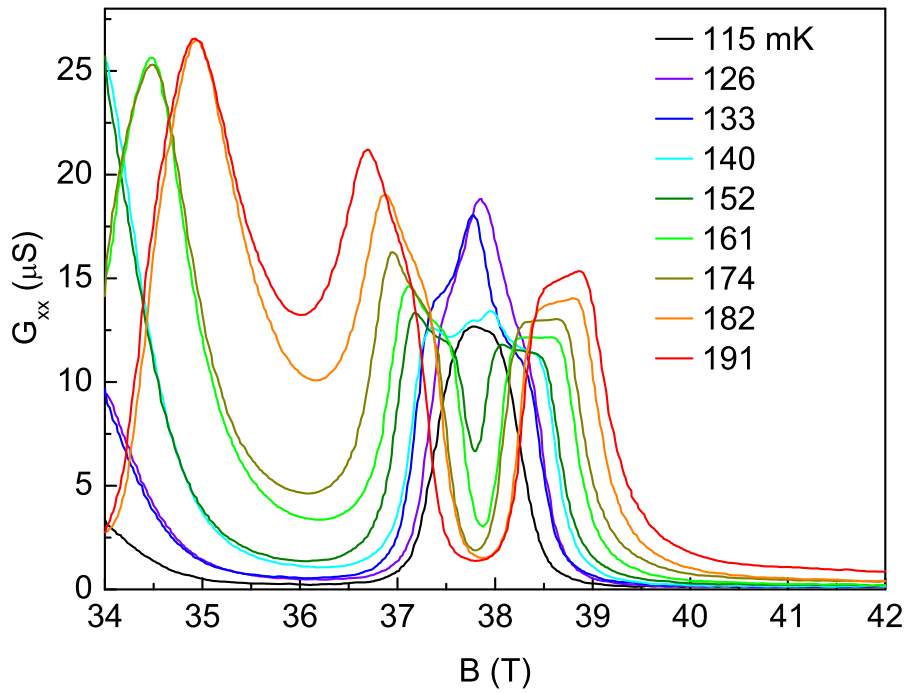


Figure 6.14 : T -dependent conductance of sample A2 (h-QW-A-2) (for $T = 115 - 191$ mK) is measured in a magnetic range: $B \sim 34 - 42$ T.

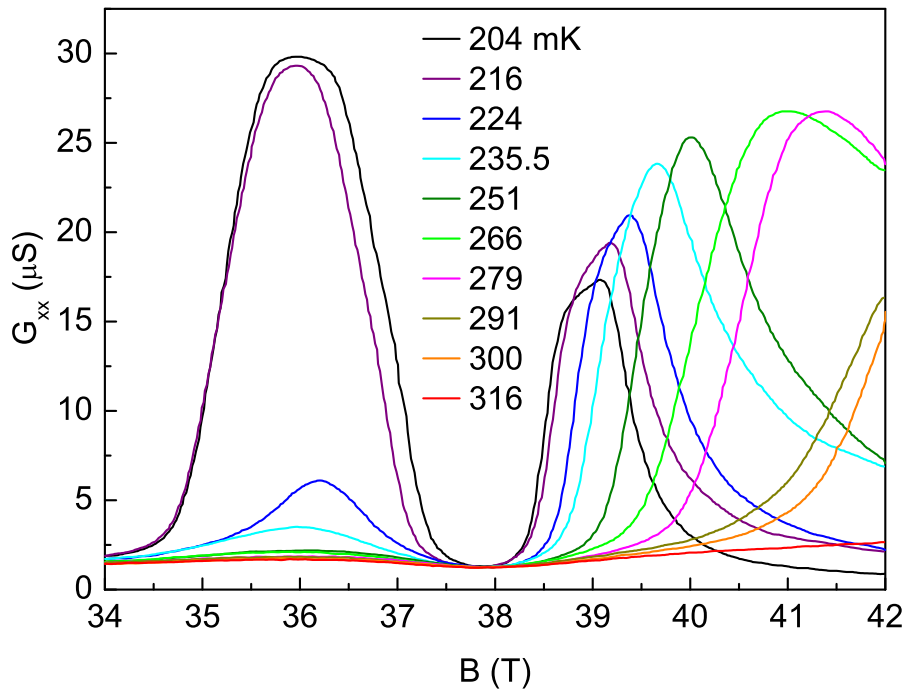


Figure 6.15 : T -dependent conductance of sample A2 (h-QW-A-2) (for $T = 204 - 316$ mK) is measured in a magnetic range: $B \sim 34 - 42$ T.

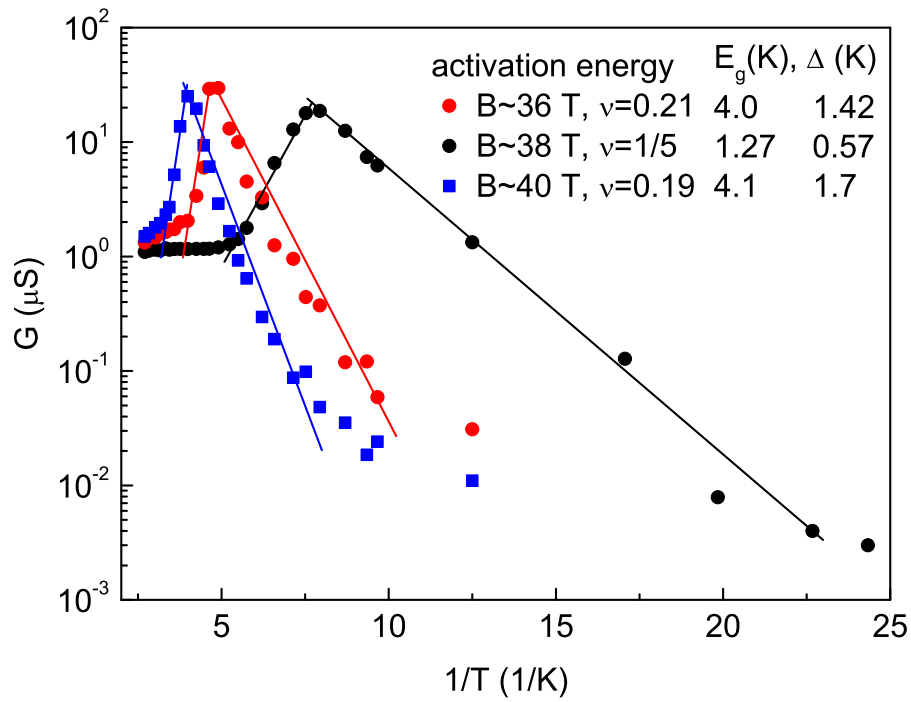


Figure 6.16 : T -dependent conductance data (sample h-QW-A-2) under various magnetic fields (at various magnetic fields: $B \sim 36$ T (red, solid circle), 38 T (black, solid circle), 40 T (blue, solid square)). The Arrhenius plot exhibits two energy scales: Energy gap (E_g) $G_{xx} \sim \exp(E_g/k_B T)$ and activation energy (Δ): $G_{xx} \sim \exp(-\Delta/k_B T)$.

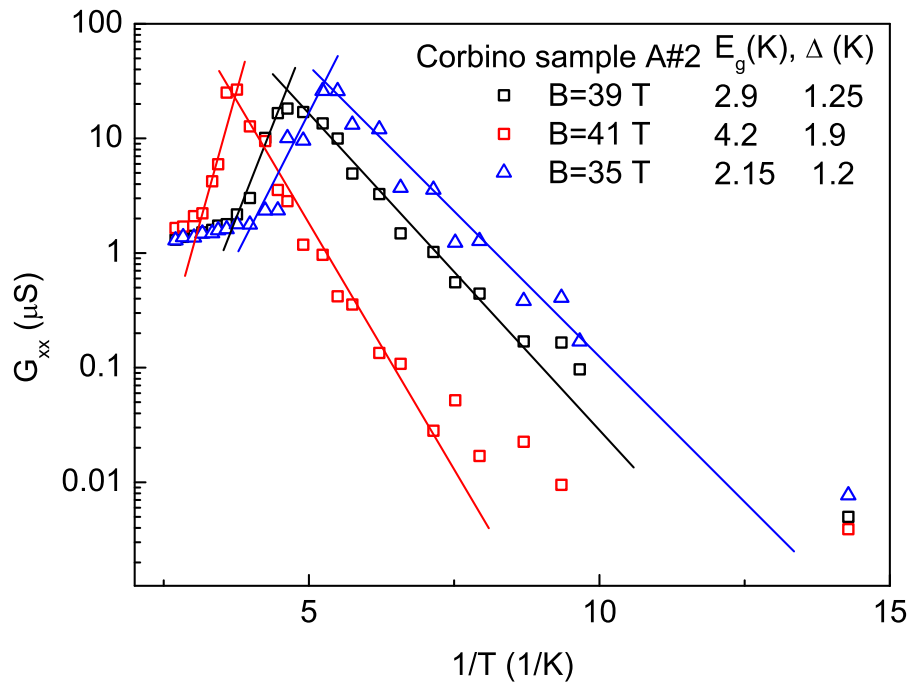


Figure 6.17 : T -dependent conductance data (sample h-QW-A-2) under various magnetic fields (at various magnetic fields: $B \sim 35$ T (blue open triangular), 39 T (black, open square), 41 T (red, open square)). The Arrhenius plot exhibits two energy scales: Energy gap (E_g) $G_{xx} \sim \exp(E_g/k_B T)$ and activation energy (Δ): $G_{xx} \sim \exp(-\Delta/k_B T)$.

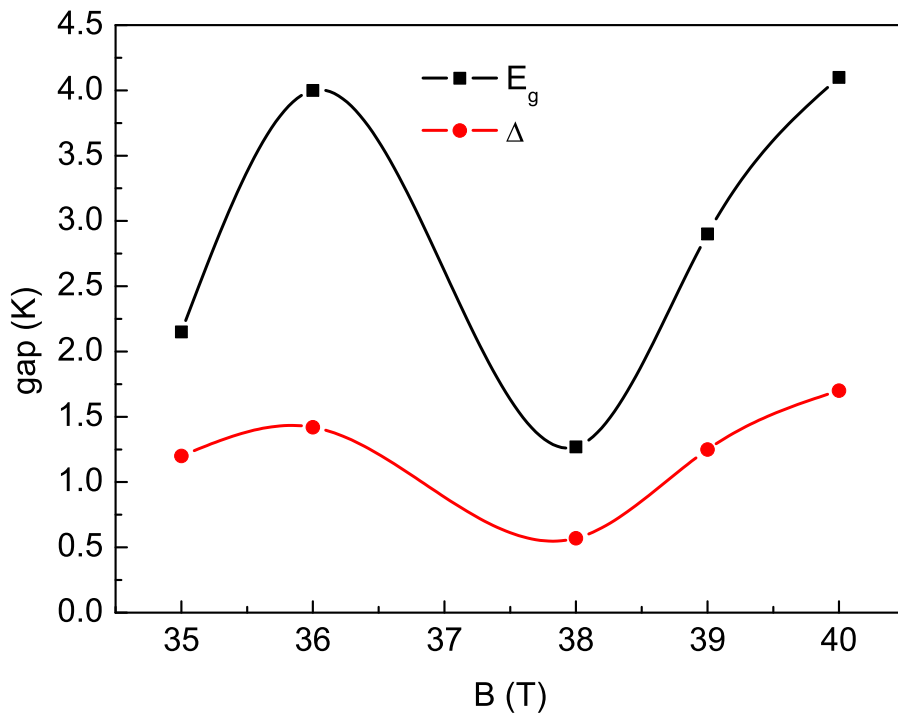


Figure 6.18 : Energy gaps E_g and Δ (of sample h-QW-A-2) under various magnetic fields: 35 T, 36 T, 38 T, 39 T, 40 T, 41 T.

high density hole system. At higher temperatures ($T > 170$ mK), the conductance starts to decrease, and the measured values at 240 mK and 364 mK are almost the same. The saturation of the conductance indicates the composite fermions at $\nu = 1/5$ for the high temperatures. Let us come back to the peaks of conductance of various heights at lower T (20 mK \sim 170 mK). As T goes up, both the B -position and the intensity of peak increase. One possible explanation of this phenomenon is related to the mass and size of the solid phase at lower temperatures. Actually, it is rather surprising that as temperature increases, the conductance at $\nu = 1/5$ increases to a maximum ($\sim 5 \mu\text{S}$) and then decreases again. Qualitatively, based on the T -dependent conductance data, we can plot a dramatic phase diagram between solid and liquid vs. B and T .

Moreover, quantitative analysis gives us more information on the varying- T procedure. We obtained Figure 6.16 and Figure 6.17 by extracting the conductance values of various magnetic fields ($B = 36$ T, 38 T, 39 T, 40 T, 41 T) for different temperatures. It is rather amazing that the conductance increases dramatically, reaches a maximum value, and then drops sharply with increasing temperature. This type of λ -shape traces are universal for the range of $B \sim 35 - 42$ T. The figures are plotted as the logarithm form versus the inverse of temperature, which is known as ‘‘Arrhenius plot’’. The Arrhenius plots exhibit a behavior: $G_{xx} \propto \exp(\Delta/k_B T)$; here, the Δ indicate an certain energy scale, which is independent of temperature. This energy scale can be viewed as the energy required by the transition from ground state to excited state. Figure 6.18 exhibits the energy gaps E_g and Δ under various magnetic fields. Generally speaking, the conductance values keep rising for an increasing T in the low- T range, and keep lowering for an increasing in the high- T range. Here, we note the energy scale of low- T range as E_g , and the energy of high- T range as Δ .

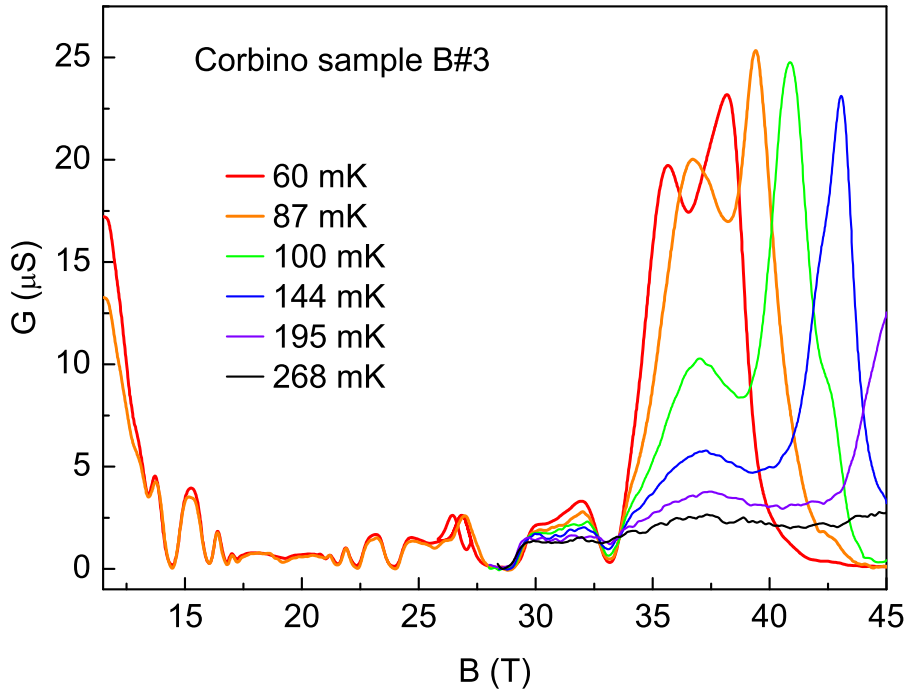


Figure 6.19 : T -dependent conductance of Corbino sample B3 (h-QW-B-3) with T : 60 mK to 270 mK.

Comparing with the neighboring magnetic fields (36 T and 40 T), both E_g (~ 1.27 K) and Δ (~ 0.57 K) of the $\nu = 1/5$ state ($B \sim 38$ T) are much lower. The energy values of various magnetic fields are: $E_g \sim (2 - 4)$ K and $\Delta \sim (1 - 2)$ K.

In addition, we present the results of E -dependent conductances (Figure 6.11) T -dependent conductances (Figure 6.19). Under various electric fields, the peaks are located around the LL filling factor $\nu \sim 1/4$, which is a consistent behavior with Figure 6.4 and 6.5 at the base temperature. The maximum of conductance increases with the applied electric field.

6.4 Non-linear Conductivity Measurements

In the last section, we observed Wigner solid sliding under larger electric fields. In this section we will show evidence of the sliding Wigner crystal. We measured the non-linear conductivity by applying dc and ac electric field simultaneously. The circuit (Figure 6.1) for the measurements was discussed in the Section 6.2. In the experiments, we applied the dc fields by a Keithley 6221A current source and the ac field by a lock-in amplifier. In the measurements, we constantly applied the ac voltage of 30 mV output (from lock-in amplifier), which corresponds to an ac-electric field of 6.9 mV/cm. For a fixed magnetic field, we swept the current from 0 to $\sim 30 \mu\text{A}$, which produced a dc-field from 0 to 0.69 (V/cm). For the simplest model, we discussed the relation between the voltage of the electric field, $V \sim 1/r$. A majority of applied field is distributed on the inner radius of the Corbino sample.

The results of non-linear I - V vs. E_{dc} are presented in Figure 6.20. For $B \sim 37.8 \text{ T}$ and 38.1 T , (the corresponding LL filling factor $\sim 1/5$), the dI/dV displays almost a linear curve under a sweeping dc-field from 0 to $\sim 0.15 \text{ (V/cm)}$. The linear behavior of conductivity indicates the liquid phase for the filling factor $1/5$. Actually, the existence of rather small thresholds indicate the FQH liquid mixing with Wigner lattice order. For $B \sim 37.7 \text{ T}$, the dI/dV trace deviates from the linear behavior, which can be interpreted as a mixture of liquid phase and solid phase. For magnetic fields lower than 37 T ($B \sim 34 \text{ T}$, 36 T), the dI/dV shows intriguing nonlinear behaviors: below a threshold field, the derivative conductivity is $\sim \text{zero}$; on the other hand, for the dc-field above the threshold, the dI/dV increase rapidly. The threshold field for $B \sim 34 \text{ T}$ and 36 T are ~ 0.22 and 0.35 mV/cm , respectively. The trace for 39 T shows a negative differential conductivity with an unknown mechanism. Intuitively, E_{th} can be used for describing domain size and the mass of the Wigner

Solid. Some groups reported the measured threshold fields [41, 44, 83]; however, it is rather puzzling that the results vary over several orders of magnitudes. A key factor is that the measurements include both longitudinal and transversal components.

Combining the information we just analyzed (in Figure 6.20), we obtained the Figure 6.21, which displays the threshold fields (E_{th}) under various magnetic fields (B). The figure of E_{th} vs. B , can be viewed as one kind of rough phase diagram: the very low threshold represents the linear transport, which is a liquid phase; the high threshold represents the non-linear transport, which exhibits the Wigner solid phase.

For convenience, we also plotted the slope (dj/dE) under high magnetic fields, shown in Figure 6.22. For slightly lower and higher filling factors ($\nu > 1/5$ and $\nu < 1/5$), the sliding Wigner solid exhibits rather large slopes. We note that, in Figure 6.18, the traces exhibit intriguing slopes of various LL filling factors, some complicated behaviors exist for some traces (i.e. 34 T, 39 T). At $B \sim 34$ T, two slopes exist; for $B \sim 39$ T, the behavior is even more complex, a knee-point locates around $E \sim 0.46$ V/cm. One possible interpretation for the case of $B \sim 34$ T ($\nu \sim 2/9$), which shows two slopes comes from the two Wigner solids on both sides. Furthermore, the mechanism for the details at $B \sim 39$ T, is still unknown.

In general, a schematic phase diagram can be described as follows: the $\nu = 1/5$ exhibits a competing phase between FQHE liquid and Wigner solid phase. For the base $T \sim 20$ mK, at $\nu = 1/5$ filling factor, a competing phase exists between the Wigner solid phase and FQHE liquid phase. For higher $T \sim 100 - 250$ mK, the Wigner solid melts, with a $\nu = 1/5$ FQHE liquid phase dominant. As $T \sim 250 - 350$ mK, the FQHE liquid transforms into a composite fermions (CF) sea. At low $T \sim 20 - 100$ mK, two Wigner crystal phases are located on both sides of FQHE liquid phase. The Wigner solid phases diminish gradually as T increases. We should note that

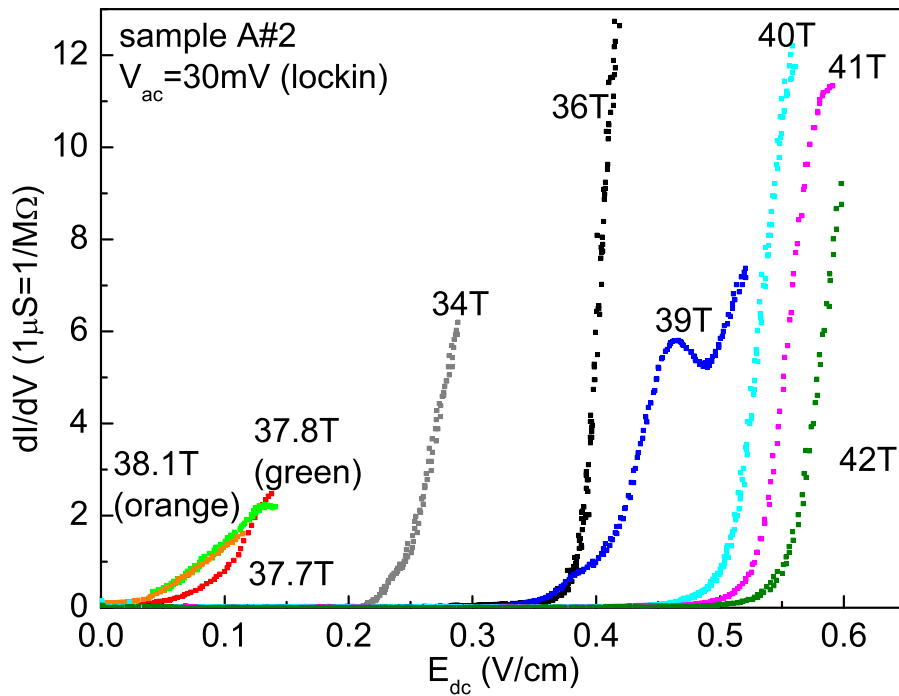


Figure 6.20 : The nonlinear conductivity measurements (h-QW-A-2) exhibit large threshold electric field in solid phase, the linear behavior at $B \sim 37.8, 38.1$ T indicate the liquid phase at these magnetic fields. From Lockin-amplifier, we applied ac voltage $V_{ac}=30$ mV, which corresponds to the ac-field $E_{ac} = 6.9$ mV/cm at the inner radius of the Corbino sample.

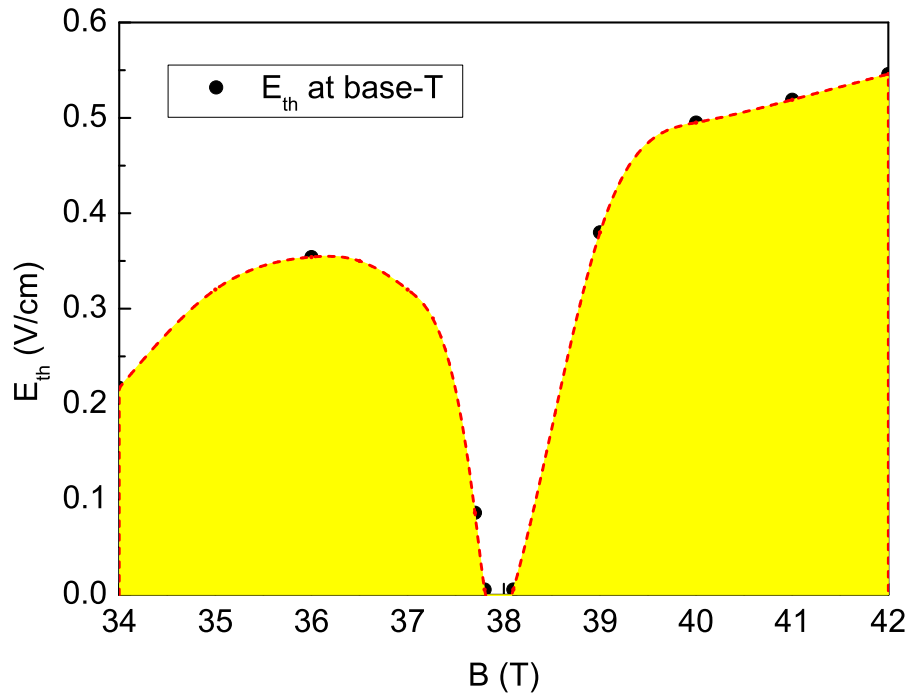


Figure 6.21 : The threshold field under various magnetic fields simply indicate the parameters of the phases of various filling factors.

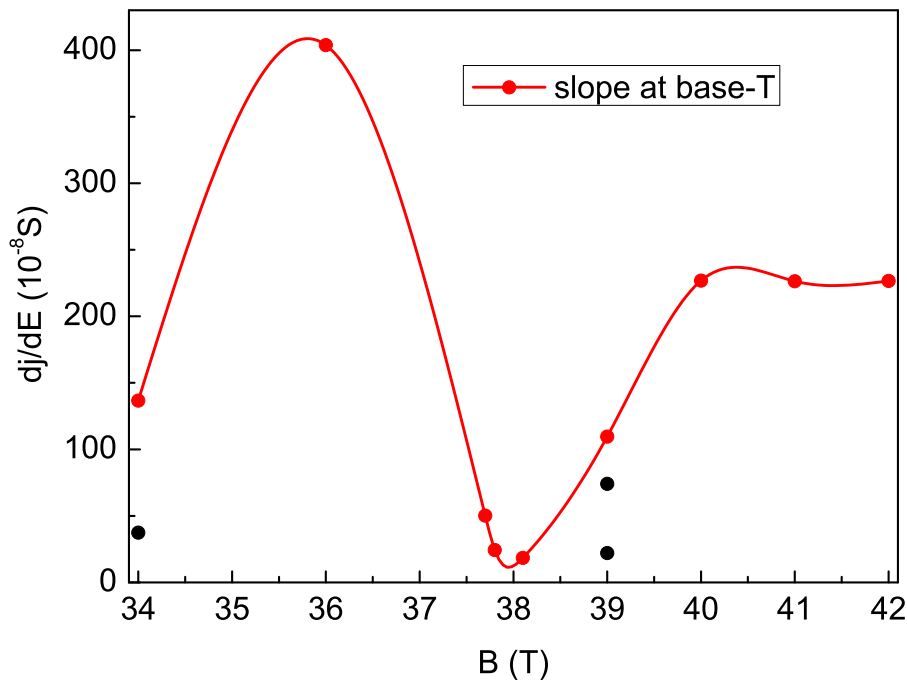


Figure 6.22 : The slope of the j vs. E ($E > E_{th}$) in the nonlinear conductance measurements.

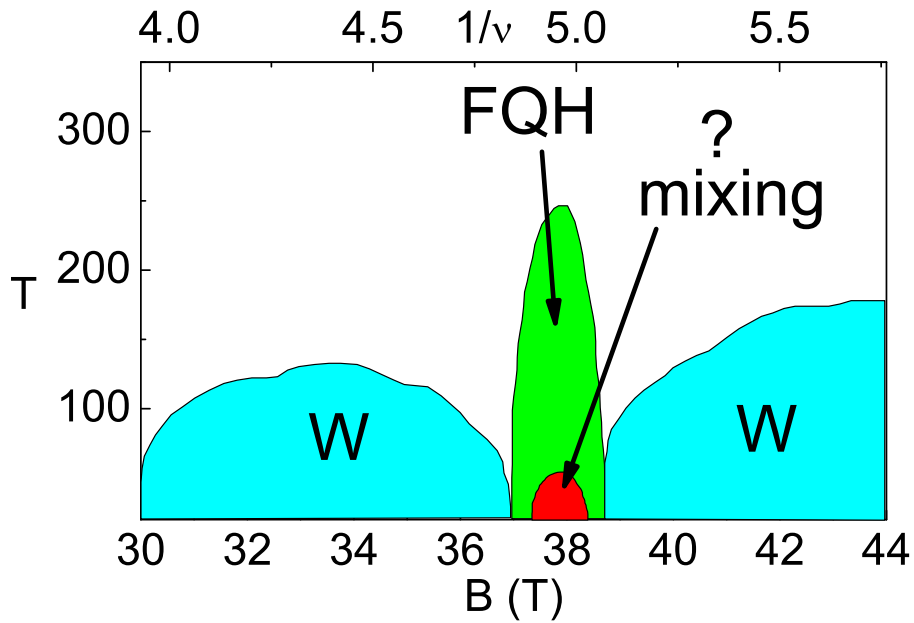


Figure 6.23 : The schematic of phase diagram of the 20 nm wide GaAs/AlGaAs QW sample A2 (h-QW-A-2) with a high hole density ($p \sim 2 \times 10^{11} \text{ cm}^{-2}$). The phase diagram exhibit the phases under various temperature (T) and magnetic field (B).

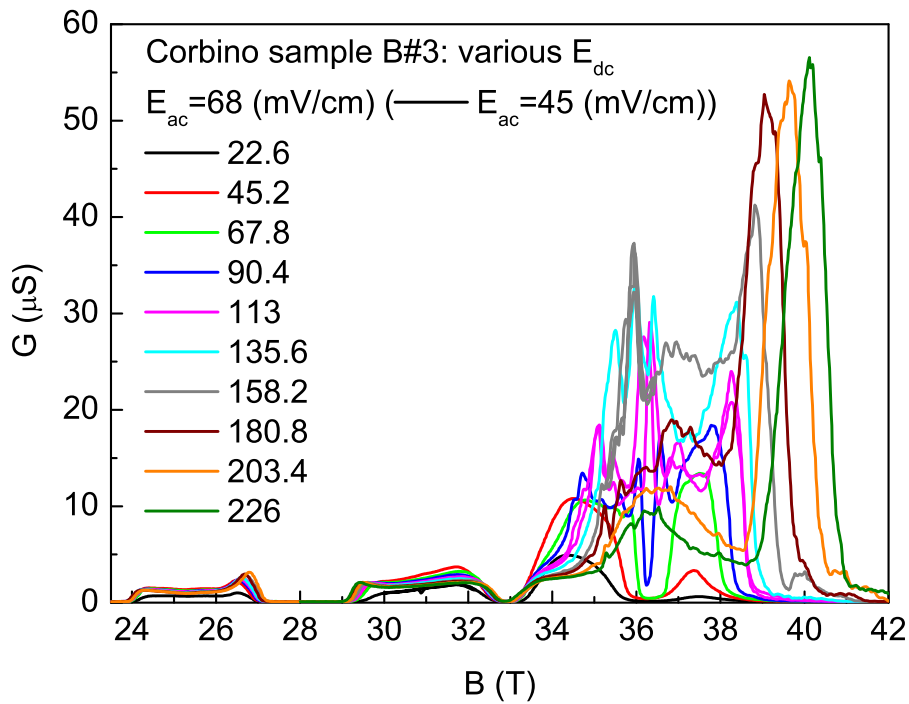


Figure 6.24 : The differential conductance of Corbino sample B (h-QW-B-3) is performed by applying ac+dc electric fields, with dc field $\sim 22.6 \text{ mV/cm} - 226 \text{ mV/cm}$.

the carriers are warmed up due to the heating effect which comes from the sweeping electric field in the measurements. Considering the results of a small applied voltage (in Figure 6.7), the hole system displays a zero conductance for small fields (E) and base T . Therefore, Wigner solid phase should be dominant at the lowest $T \sim 20$ mK. For higher carrier temperature, the solid starts melting, with the mixture phase of the FQH liquid and Wigner solid located around $\nu = 1/5$. The λ -shape traces in the T -dependent conductance is different from previous experiments, which possibly comes from the competition between the pinning of WC and forming of superfluid.

Chapter 7

Conclusions of Wigner Crystal in 2DHS

We tested the new type of 2DHS sample: carbon (C) modulation doped (001) oriented GaAs/Al_xGa_{1-x}As 20 nm wide quantum wells: wafer A ($x=0.24$) and B ($x=0.325$). In the high magnetic field ($B \sim 45$ T) experiments, we measured the magnetoconductance (T -dependent conductance) and nonlinear conductivity. The high-density hole system (in the wafer A) exhibits a reentrant insulating phase located around $\nu = 1/5$ FQHE liquid, which is a typical electron-like behavior [41,43,44]. A schematic of phase diagram can be obtained from our T -dependent experimental results: at base temperature ~ 20 mK, the Wigner solid phase has a lower ground state energy than that of FQH liquid. The hole Wigner solid starts melting as T increases. During the melting process, λ -shape traces are very distinct with previous results. In varying T , longitudinal conductance exhibited a thermally activated behavior, by which rather large energy gaps of various LL filling factors can be obtained.

We observed the sliding Wigner crystal by applying external ac and dc electric fields. Generally speaking, the results of conductance measurements and nonlinear conductance experiments are rather consistent with each other. Under a high external electric field, the Wigner solid starts sliding, with the $1/5$ and $2/9$ FQHE liquid states becoming distinct. On the other hand, the derivative I - V curvatures reveal the sliding Wigner solids around $\nu = 1/5$. Large threshold electric fields are obtained for nearby Wigner solids, displaying sharp slopes of dj/dE .

From the discussions above, we described schematically a phase diagram: for a

low temperature around $\nu = 1/5$ state, the competition between Wigner solid and FQHE liquid exists. Wigner solids on both sides persist up to $T \sim 100 - 200$ mK.

Appendix A

Sample Information

A.1 2D Electron Samples

Sample e-QW-A-1: (high electron density, 20 nm wide $\text{Al}_{0.24}\text{Ga}_{0.76}\text{As}/\text{GaAs}$ QW) Van der Pauw sample with Indium contacts. (The Figure 3.4 displays the measurements on this sample.)

Sample e-QW-A-2: (high electron density, 20 nm wide $\text{Al}_{0.24}\text{Ga}_{0.76}\text{As}/\text{GaAs}$ QW) Van der Pauw sample with Ge/Pd/Au alloy contacts. (The Figures 3.6, 3.7, 3.8, 3.9, 3.10, 3.11, 3.12, 3.13, 3.14, 3.15, 3.16, 3.17, 3.24, 3.25 display the measurements on this sample.)

Sample e-QW-A-3: (high electron density, 20 nm wide $\text{Al}_{0.24}\text{Ga}_{0.76}\text{As}/\text{GaAs}$ QW) Van der Pauw sample with Indium contacts. (The Figures 3.5, 3.18, 3.19, 3.20, 3.21, 3.22, 3.23 display the measurements on this sample.)

Sample e-QW-B: ($n \sim 4 \times 10^{11} \text{ cm}^{-2}$, 25 nm wide $\text{AlGaAs}/\text{GaAs}$ QW), Van der Pauw sample with Indium contacts. (The Figure 3.19 displays the measurements on this sample.)

A.2 2D Hole Samples

Sample h-QW-A-1: (high density ($n \sim 1.9\text{--}2.0 \times 10^{11} \text{ cm}^{-2}$) 20 nm wide $\text{Al}_{0.24}\text{Ga}_{0.76}\text{As}/\text{GaAs}$ QW) Van der Pauw sample with In/Zn Ohmic contacts.

Sample h-QW-A-2: (high density ($n \sim 1.9\text{--}2.0 \times 10^{11} \text{ cm}^{-2}$) 20 nm wide $\text{Al}_{0.24}\text{Ga}_{0.76}\text{As}/\text{GaAs}$

QW) Corbino sample with Au (98%)/Be(2%) Ohmic contacts. (The Figures 6.6, 6.7, 6.8, 6.9, 6.10, 6.11, 6.12, 6.13, 6.14, 6.15, 6.16, 6.17, 6.18, 6.19, 6.20, 6.21 display the measurements on this sample.)

Sample h-QW-B-2:(high density ($n \sim 2.3 \times 10^{11} \text{ cm}^{-2}$) 20 nm wide $\text{Al}_{0.325}\text{Ga}_{0.675}\text{As}/\text{GaAs}$ QW) Van der Pauw sample with In/Zn Ohmic contacts. (The Figure 6.5 displays the measurements on this sample.)

Sample h-QW-B-3:(high density ($n \sim 2.3 \times 10^{11} \text{ cm}^{-2}$) 20 nm wide $\text{Al}_{0.325}\text{Ga}_{0.675}\text{As}/\text{GaAs}$ QW) Corbino sample with In/Zn Ohmic contacts. (The Figures 6.4, 6.11, 6.19 and 6.24 display the measurements on this sample.)

A.3 Effect of Light on Samples

The electron and hole samples are both sensitive to the light. The electron samples from Loren Pfeiffer display high quality by means of illuminating with an LED. By shining LED, the electrons tunnels through the barrier between the dopant layer and QW, with a larger electron density accumulated in the QW. On the hand, the mobility also increases under the light. However, the new C-doped (001) $\text{AlGaAs}/\text{GaAs}$ wafers (from Micheal J. Manfra) are quite sensitive to the light: even very small leakage of light will change the state of the sample. For example, the $\text{Al}_{0.24}\text{Ga}_{0.76}\text{As}/\text{GaAs}$ 20 nm wide QW has a lower density $p \sim 1.6 \times 10^{11} \text{ cm}^{-2}$ under the light. Actually, with the protection of the Aluminum foil on the top end of the probe, the hole density reached a larger value: $p \sim 1.9 \times 10^{11} \text{ cm}^{-2}$.

Appendix B

Determination of crystalgraphic axis by defect-pit etching technique

From previous results, high resistance is parallel to a certain crystalline orientation in GaAs wafer. There are three methods for checking the [110] direction of GaAs: labelling the wafer when it comes, etching GaAs to see the profile of the cross-section, and bowtie structure always parrallel to the [110] axis in III-V family semiconductors.

B.1 Etching Profile of Cross-Section

In our samples (AlGaAs/GaAs QW), the quantum well is ~ 160 nm under the surface, and the cap layer is around 50 nm. The etching process are as follows.

(1) Use e-beam lithography to create an (a few micron wide) line.

(2) Put GaAs sample in the mixture of C_2H_4O (citric acid) and H_2O_2 (ratio 5:1) for wet-etching for ~ 2 minutes. This solution is supposed to be good for etching GaAs and stopped at AlGaAs, however, it not true for our samples.

This method is not good for our samples, because of the roughness of the sample edges. The roughness of the sample is $\sim 20 \mu m$, and the etched pattern is on the order of nm.

B.2 Pit-Etching by Using KOH for GaAs Sample

In order to identify the crystal axis of the sample, we used the defect pit-etching procedure, as briefly described here (thanks due to Yuanhua Dai who did the etching experiment [57]).

(1) Cleave a piece of $2 \text{ mm} \times 2 \text{ mm}$ square sample from the same wafer we measured.

(2) Then put the KOH crystals in the Cr crucible, and put crucible on the hot plate. Heat KOH solids up to around 350°C , until all the crystals melt.

(3) Etch the sample inside the melting KOH for $\sim 15 - 20$ minutes. In this section, GaAs will be etched. The etching rate varies based on the samples. In the real procedure, the wafers are etched with different time.

(4) The sample is taken out with a small Cr basket, and then is rinsed in DI water.

(5) Check the crystalline orientations under a microscope ($\times 30$ magnification), or SEM. In the SEM observation, the bowtie structures that we expected were not observed. Actually, we observed rectangle structures, which comes from the overetching of the sample. In Figure B.2, numerous rectangle structures in the GaAs layer are shown, with the long-side along $[110]$ axis, and the short-side along the $[\bar{1}\bar{1}0]$ direction orientation. Compare with the magnetoresistances, the hard direction of $9/2$, $11/2$ state is along $[\bar{1}\bar{1}0]$ direction, easy transport direction is along $[110]$ orientation [38]. SEM Figures B.2 and B.3 display the rectangle structures close to the heterojunction, with the typical rectangle length scale around $100 - 200 \text{ nm}$. From the back of the sample, we also find some rectangle etching pit on the substrate with a length scale $\sim 2 - 3 \text{ mm}$.



Figure B.1 : Cr crucible and basket are used for pit-etching with KOH.

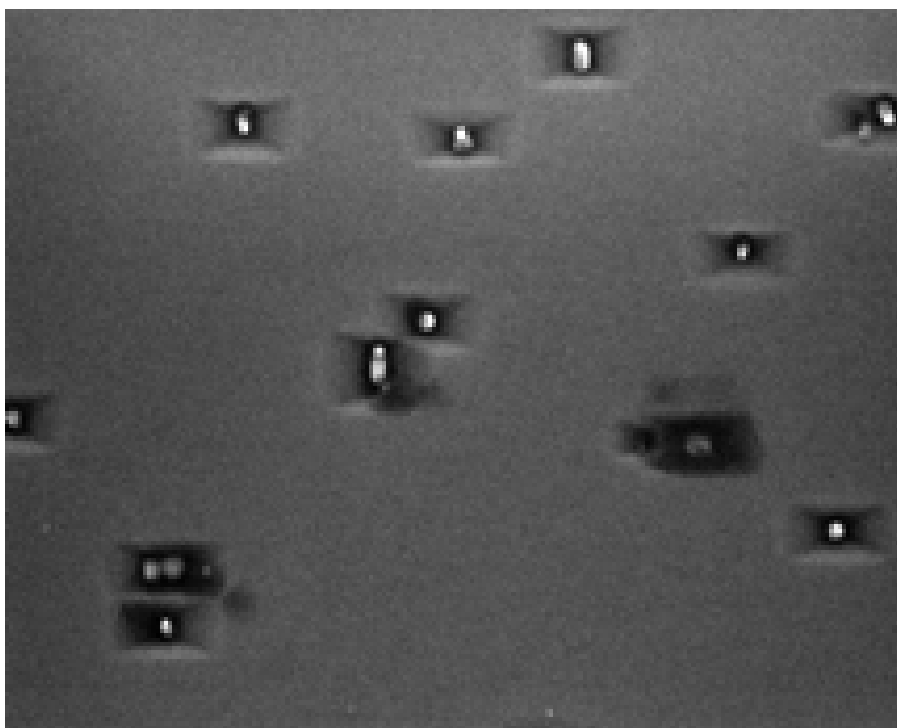


Figure B.2 : SEM picture, with the scale of rectangle structure $\sim 100 - 200$ nm.

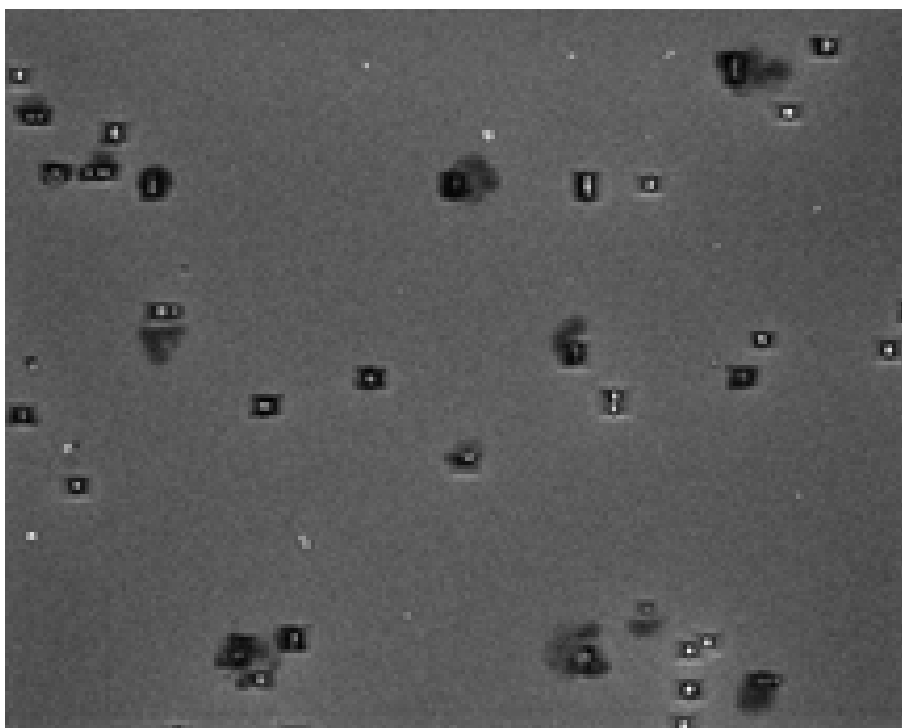


Figure B.3 : SEM picture with a larger scale, and the typical scale of rectangle structure $\sim 100 - 200$ nm.

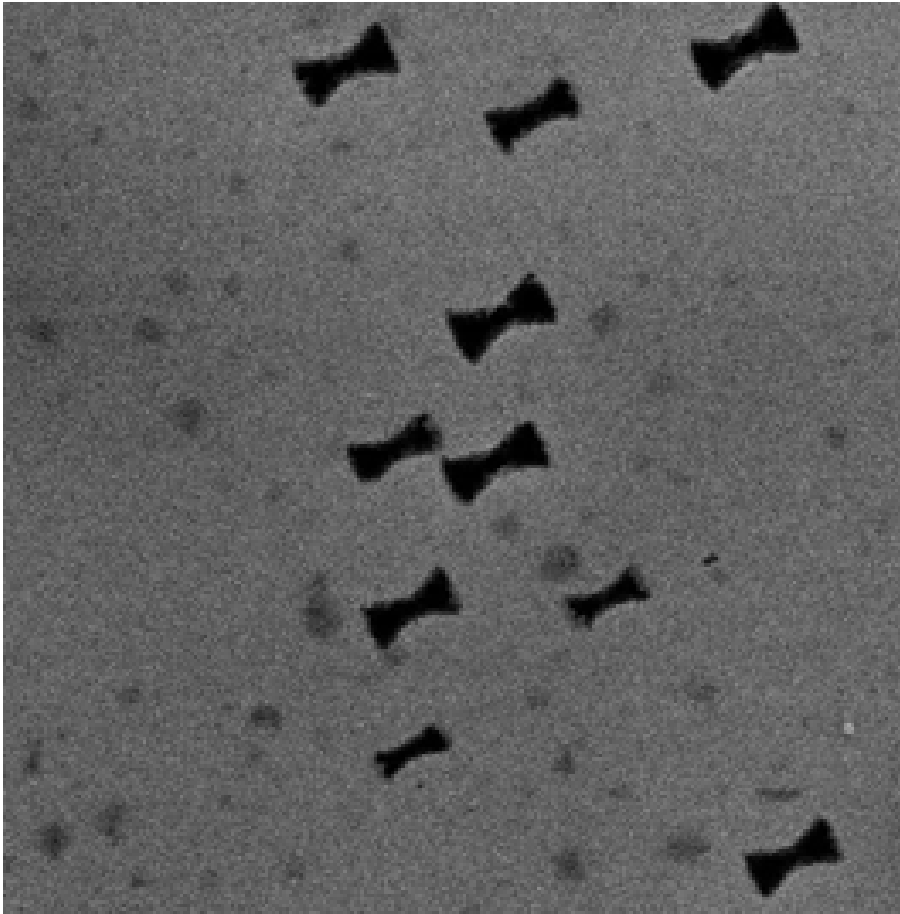


Figure B.4 : Bowtie structures in the GaAs sample are obtained by pit-etching with $\text{H}_3\text{PO}_4:\text{H}_2\text{O}_2:\text{H}_2\text{O}$ (1:1:38).

B.3 Pit-Etching by Using $\text{H}_3\text{PO}_4:\text{H}_2\text{O}_2:\text{H}_2\text{O}$ (1:1:38) for GaAs Sample

For the GaAs samples, we also use $\text{H}_3\text{PO}_4:\text{H}_2\text{O}_2:\text{H}_2\text{O}$ (1:1:38) for pit-etching. In this method, the bowtie structure display in the sample (Figure B.4).

Bibliography

- [1] *Perspective in Quantum Hall Effects: Novel Quantum Liquids in Low-Dimensional Semiconductor Structures*, Edited by Sankar Das Sarma and Aron Pinczuk (Wiley and Sons, New York, 1998).
- [2] K. Von Klitzing, G. Dorda, and M. Pepper, Phys. Rev. Lett. **45**, 494 (1980).
- [3] D. C. Tsui, H. L. Stormer, and A. C. Gossard, Phys. Rev. Lett. **48**, 1559 (1982).
- [4] R. B. Laughlin, Phys. Rev. Lett. **50**, 1395 (1983).
- [5] J. K. Jain, Phys. Rev. Lett. **63**, 199 (1989), Phys. Rev. B. **40**, 8079 (1989), Phys. Rev. B. **41**, 7653 (1989).
- [6] *Composite Fermions: A Unified View of the Quantum Hall Regime*, Edited by O. Heinonen (World Scientific, Singapore, 1998)
- [7] H. -W. Jiang, H. L. Stormer, D. C. Tsui, L. N. Pfeiffer, and K. W. West, Phys. Rev. B. **40**, 12013 (1989).
- [8] B. I. Halprein, P. A. Lee, and N. Read, Phys. Rev. B. **47**, 7312 (1993).
- [9] V. Kalmeyer, and S. C. Zhang, Phys. Rev. B. **46**, 9889 (1992).
- [10] R. L. Willett, J. P. Eisenstein, H. L. Stormer, D. C. Tsui, A. C. Gossard, and J. H. English, Phys. Rev. Lett. **59**, 1776 (1987).

- [11] J. S. Xia, W. Pan, C. L. Vicente, E. D. Adams, N. S. Sullivan, H. L. Stömer, D. C. Tsui, L. N. Pfeiffer, K. W. Baldwin, and K. W. West, Phys. Rev. Lett. **93**, 176809 (2004).
- [12] W. Pan, R. R. Du, H. L. Stormer, D. C. Tsui, L. N. Pfeiffer, K. W. Baldwin, and K. W. West, Phys. Rev. Lett. **83**, 820 (1999).
- [13] G. Moore and N. Read, Nucl. Phys. B. **360**, 362 (1992).
- [14] S. Das Sarma, M. Freedman, and C. Nayak, Phys. Rev. Lett. **94**, 166802 (2005).
- [15] R. H. Morf, Phys. Rev. Lett. **80**, 1505 (1998).
- [16] M. Greiter, X. G. Wen, and F. Wilczek, Phys. Rev. Lett. **66**, 3205 (1991); Nucl. Phys. B. **374**, 567 (1992).
- [17] E. H. Rezayi, and F. D. M. Haldane, Phys. Rev. Lett. **84**, 4685 (2000).
- [18] M. R. Peterson, K. Park, and S. Das Sarma, Phys. Rev. Lett. **101**, 155308 (2008).
- [19] M. Levin, B. I. Halperin, and B. Rosenow, Phys. Rev. Lett. **99**, 236806 (2007).
- [20] S. -S. Lee, S. Ryu, C. Nayak, and M. P. A. Fisher, Phys. Rev. Lett. **99**, 236807 (2007).
- [21] A. Yu Kitaev, Ann. Phys. (N.Y.), **303**, 2, (2003).
- [22] H. L. Stormer, R. R. Du, D. C. Tsui, L. N. Pfeiffer, and K. W. West, Bull. Am. Phys. Soc. **38**, 235 (1993).
- [23] M. P. Lilly, K. B. Cooper, J. P. Eisenstein, L. N. Pfeiffer, and K. W. West, Phys. Rev. Lett. **82**, 394 (1999).

- [24] R. R. Du, D. C. Tsui, H. L. Stormer, L. N. Pfeiffer, K. W. Baldwin, and K. W. West, *Solid State Commun.* **109**, 389 (1999).
- [25] M. P. Lilly, K. B. Cooper, J. P. Eisenstein, L. N. Pfeiffer, and K. W. West, *Phys. Rev. Lett.* **83**, 824 (1999).
- [26] M. M. Fogler, A. A. Kukalov, and B. I. Shklovskii, *Phys. Rev. B.* **54**, 1853 (1996).
- [27] R. Moessener and J. T. Chalker, *Phys. Rev. B.* **54**, 5006 (1996).
- [28] E. Fradkin and S. A. Kivelson, *Phys. Rev. B.* **59**, 8065 (1999).
- [29] J. P. Eisenstein, R. Willett, H. L. Stormer, D. C. Tsui, and A. C. Gossard, and J. H. English, *Phys. Rev. Lett.* **61**, 997 (1988).
- [30] W. Pan, H. L. Stormer, D. C. Tsui, L. N. Pfeiffer, K. W. Baldwin, and K. W. West, *Solid State Commun.* **119**, 641 (2001) (HIGFET, heterojunction insulated gated field- effect transistor).
- [31] R. H. Morf, and N. d'Ambrumenil *Phys. Rev. Lett.* **68**, 113309 (2003).
- [32] S. Das Sarma, M. Freedman, and C. Nayak, *Phys. Rev. Lett.* **94**, 166802 (2005).
- [33] M. R. Peterson, K. Park, and S. Das Sarma, *Phys. Rev. Lett.* **78**, 156803 (2008).
- [34] H. Wang, D. S. Sheng, and F. D. M. Haldane, *Arxiv*: 0905. 3589.
- [35] W. Bishara, and C. Nayak, *Phys. Rev. B.* **80**, 241302 (2009).
- [36] E. H. Rezayi, S. H. Simons, *Arxiv*: 0912.0109.
- [37] A. E. Feiguin, E. Rezayi, Kun Yang, C. Nayak, S. Das Sarma, *Phys. Rev. Lett.* **79**,115322 (2009).

- [38] K. B. Cooper, M. P. Lilly, J. P. Eisenstein, L. N. Pfeiffer, and K. W. West, *Solid State Commun.* **119**, 89 (2001).
- [39] F. D. M. Haldane, *Phys. Rev. Lett.* **51**, 625 (1983).
- [40] E. Wigner, *Phys. Rev.* **46**, 1002 (1934).
- [41] Yuan. P. Li, T. Sajoto, L. W. Engle, D. C. Tsui, and M. Shayegan, *Phys. Rev. Lett.* **67**, 1630 (1991).
- [42] M. B. Santos, Y. W. Suen, M. Shayegan, Y. P. Li, L. W. Engel, and D. C. Tsui, *Phys. Rev. Lett.* **68**, 1188 (1992).
- [43] T. Sajoto, Y. P. Li, L. W. Engel, D. C. Tsui, and M. Shayegan, *Phys. Rev. Lett.* **70**, 2321 (1993).
- [44] V. J. Goldman, M. Santos, M. Shayegan, and J. E. Cunningham, *Phys. Rev. Lett.* **65**, 2189 (1990).
- [45] Yong. P. Chen, R. M. Lewis, L. W. Engel, D. C. Tsui, P. D. Ye, Z. H. Wang, L. N. Pfeiffer, and K. W. West, *Phys. Rev. Lett.* **93**, 206805 (2004).
- [46] I. Dimov, B. I. Halperin, and B. Rosenow, *Phys. Rev. Lett.* **100**, 126804 (2008).
- [47] B. I. Halperin, *Helv. Phys. Acta* **56**, 75 (1983).
- [48] K. Park, V. Melik-Alaverdian, N. E. Bonesteel, and J. K. Jain, *Phys. Rev. B.* **58**, R10167 (1998).
- [49] H. C. Choi, et al, *Phys. Rev. B* **77**, 081301 (2008).
- [50] C. R. Dean, et al, *Phys. Rev. Lett.* **100** 146803 (2008). *Phys. Rev. Lett.* **101**, 186806 (2008).

- [51] Arkadiusz Wójs, Gunnar Müller, Steven H. Simon, and Nigel R. Cooper, Phys. Rev. Lett. **104**, 086801 (2010).
- [52] G. Sambandamurthy, R. M. Lewis, Han Zhu, Y. P. Chen, L. W. Engel, D. C. Tsui, L. N. Pfeiffer, and K. W. West, Phys. Rev. Lett. **100** 256801 (2008).
- [53] F. F. Fang and P. J. Stiles, Phys. Rev. **174**, 823 (1968).
- [54] John H. Davies, The Physics of Low-Dimensional Semiconductors (Cambridge University Press, Cambridge, 1998).
- [55] I would like to thank Yanhua Dai very much for her work in etching and observing with SEM.
- [56] Thanks to Dr. Tauno Knuuttila for his excellent data at extremely low temperatures.
- [57] M. Tong, D. G. Ballegeer, A. Ketterson, E. J. Roan, K. Y. Cheng, and I. Adesda, (wet etching of GaAs), J. of Electro. Matter. **21**, 9 (1992).
- [58] Yuan. P. Li, Ph.D. thesis, Princeton University (1994).
- [59] M. B. Santos, J. Jo, Y. W. Suen, L. W. Engel, and M. Shayegan, Phys. Rev. B **46**, 639 (1992).
- [60] T. Sajoto, Ph.D. thesis, Princeton University (1993).
- [61] Grüner, Rev. Mod. Phys. **40**, 1129 (1988).
- [62] C. C. Grimes, and G. Adams, Phys. Rev. Lett. **42**, 795 (1979).
- [63] T. Ando, A. B. Fowler, and F. Stern, Rev. Mod. Phys. **54**, 437 (1982).

- [64] H. Fukuyama, and P. A. Lee, Phys. Rev. B **17**, 535 (1978).
- [65] P. A. Lee and T. M. Rice, Phys. Rev. B **19**, 3970 (1979).
- [66] Xuejun Zhu, P. B. Littlewood, and A. J. Millis, Phys. Rev. Lett. **72**, 2255 (1994).
- [67] Xuejun Zhu, P. B. Littlewood, and A. J. Millis, Phys. Rev. B **50**, 4600(1994).
- [68] R. R. Du, D. C. Tsui, H. L. Stormer, L. N. Pfeiffer, and K. W. West, Solid State Commun. **99**, 755 (1996).
- [69] P. J. Rodgers, C. J. G. M. Langerak, B. L. Gallagher, R. J. Barraclough, M. Henini, T. J. Foster, G. Hill, S. A. J. Wiegers, J. A. A. J. Perenboom. Physica B **184**, 95 (1993).
- [70] H. C. Manoharan, M. Shayegan, S. J. Keppeler, Phys. Rev. Lett. **73**, 3270 (1994).
- [71] Y. E. Lozovik and V. I. Yudson, JETP Lett. **22**, 11 (1975).
- [72] P. K. Lam and S. M. Girvin, Phys. Rev. B **19**, 3970 (1984).
- [73] D. Levesque, J. J. weis, and A. H. MacDonald, Phys. Rev. B **30**, 1056 (1984).
- [74] D. Yoshioka, J. Phys. Soc. Jpn. **53**, 3740 (1984).
- [75] D. Yoshioka, J. Phys. Soc. Jpn. **55**, 885 (1986).
- [76] W. Pan, K. Lai, S. P. Bayrakci, N. P. Ong, D. C. Tsui, L. N. Pfeiffer, and K. W. West, Appl. Phys. Lett. **83**, 3519 (2003).
- [77] Z. Q. Yuan, Ph.D. Thesis, Rice University (2009).
- [78] Z. Q. Yuan, R. R. Du, M. J. Manfra, L. N. Pfeiffer, and K. W. West, Appl. Phys. Lett. **94**, 052102 (2009).

- [79] H. L. Stormer, Z. Schleisinger, A. Chang, D. C. Tsui, A. C. Gossard, and W. Weigmann, *Phys. Rev. Lett.* **51**, 126 (1983).
- [80] W. I. Wang, E. E. Mendez, Y. Iye, B. Lee, M. H. Kim, and G. E. Stillman, *J. Appl. Phys. Rev. Lett.* **72**, 709 (1994).
- [81] M. J. Manfra, L. N. Pfeiffer, K. W. West, R. de Picciotto, and K. W. Baldwin, *Appl. Phys. Lett.* **86**, 162106 (2005).
- [82] X. Bayot, X. Ying, M. B. Santos, M. Shayegan, *Europhys. Lett.* **25**, 613 (1994).
- [83] R. L. Willet, H. L. Stormer, D. C. Tsui, L. N. Pfeiffer, K. W. West, M. Shayegan, M. B. Santos, and T. Sajoto, *Phys. Rev. Lett.* **40**, 6432 (1989).
- [84] H. W. Jiang, C. E. Johnson, K. L. Wang, and S. T. Hannahs, *Phys. Rev. Lett.* **44**, 8107 (1993).
- [85] Yuan. P. Li, T. Sajoto, L. W. Engle, D. C. Tsui, and M. Shayegan, *Phys. Rev. B* **47**, 9933 (1993).
- [86] Daijiro Fukuyama, *J. Phys. Soc. Jpn.* **53**, 3740(1984).
- [87] Daijiro Fukuyama, *J. Phys. Soc. Jpn.* **55**, 885 (1986).
- [88] B. G. A. Normand, P. B. Littlewood, and A. J. Millis, *Phys. Rev. B* **46**, 3920 (1992).
- [89] H. Kröhlich, *Froc. Roy. Soc.* **223**, 296 (1954).
- [90] M. Kellog, J. P. Eisenstein, L. N. Pfeiffer, K. W. West, *Phys. Rev. Lett.* **93**, 036801 (2000).

- [91] H. C. Manoharan, and M. Shayegan, Phys. Rev. B. **50**, 17662 (1994a).
- [92] F. I. B. Williams, P. A. Wright, R. G. Clark, E. Y. Andrei, G. M Deville, D. C. Glatti, O. Probst, B. Etienne, C. Dorin, C. T. Foxon, and J. J. Harris, Phys. Rev. Lett. **66**, 3285 (1991).
- [93] H. W. Jiang, H. L. Stormer, D. C. Tsui, L. N. Pfeiffer, K. W. West, Phys. Rev. B **44**, 8107 (1991).